Master's thesis

NTNU
Norwegian University of Science and Technology
Faculty of Natural Sciences
Department of Physics

Patrik Isene Sund

Characterization of a proximity-mediated magnon–exciton coupling in a ferromagnet/transition metal dichalcogenide van der Waals heterostructure

Master's thesis in MTFYMA

Supervisor: Jeroen Danon (NTNU) and Koji Usami (University of Tokyo)

August 2020

NTNU
Norwegian University of
Science and Technology

Patrik Isene Sund

Characterization of a proximity-mediated magnon–exciton coupling in a ferromagnet/transition metal dichalcogenide van der Waals heterostructure

Master's thesis in MTFYMA
Supervisor: Jeroen Danon (NTNU) and Koji Usami (University of Tokyo)
August 2020

Norwegian University of Science and Technology
Faculty of Natural Sciences
Department of Physics

Characterization of a proximity-mediated magnon–exciton coupling in a ferromagnet/transition metal dichalcogenide van der Waals heterostructure

Patrik Isene Sund

Norwegian University of Science and Technology
Department of Physics

Supervisors:
Assoc. Prof. Koji Usami & Assoc. Prof. Jeroen Danon

NTNU

14 August 2020

Acknowledgment

I would like to thank Koji Usami and Yasunobu Nakamura for giving me the opportunity to spend my last year as a Master's student at the Nakamura-Usami group. I am especially thankful to Koji for supervising me and working with me in the lab; I learned a lot this past year, thanks in no small part to him.

I would also like to thank my supervisor at NTNU, Jeroen Danon, for giving me a lot of good feedback and encouragement along the way.

I would like to thank all of the members of the Nakamura-Usami group, for welcoming me and including me in a great learning environment. I am especially thankful to Sam Wolski for giving me a lot of much-needed feedback in early stages, and for our great, invariably heated discussions. I would also like to acknowledge the members who have contributed to the experiment in the lab. I am very grateful to Masaru Onga and the Iwasa lab, who provided us with the samples used for the experiment. I am also thankful to Arnaud Gloppe for laying the groundwork of the experiment, and Yusuke 'Ponsuke' Sasaki and Keisuke Kato for working with me on the experiment and making the time spent in the lab that much more enjoyable.

Lastly, I'd like to thank my girlfriend, who came with me to Japan, and supported me throughout the year. It turns out lockdowns aren't so bad when you get to spend every day with your best friend!

Abstract

Strong coupling between heterogeneous quantum systems enable the construction of hybrid quantum systems, which can leverage the unique properties of the constituent systems for novel applications. In this thesis, I describe an experiment aiming to characterize the coupling between magnons in a thin film of yttrium iron garnet (YIG) and excitons in atomically thin layers of a transition metal dichalcogenide (TMD).

Magnons are strong candidates for applications in quantum-information processing, as they can carry information without suffering from Ohmic losses [1], and have been demonstrated to couple strongly to superconducting qubits [2]. TMDs on the other hand, are 2D materials with strong optical properties and potential applications in the creation of artificial materials with novel properties [3]. A strong coupling between magnons and excitons in TMDs would expand the range of applicability of both systems, and in particular could provide magnon-based hybrid quantum systems with a strong optical response, which has been a bottleneck in previous attempts at implementations [4].

The coupling is achieved by piling thin flakes of TMD onto a YIG film to make a van der Waals heterostructure, where the exchange interactions in the interface between the materials lead to a magnetic proximity effect, which couples the resonance energy of the excitonic modes to the out-of-plane magnetization in the YIG film. The YIG film is magnetized with an in-plane magnetic field, after which a magnon population is excited, resulting in an oscillating out-of-plane magnetization which induces a dynamic shift in the exciton resonance energy. By probing the excitons with a laser at a fixed wavelength, the dynamic shift in the resonance manifests itself as an amplitude modulation, which can be measured to determine the magnon–exciton coupling strength.

The thesis details an experimental setup and a set of experiments designed to generate and analyze such an experimental signal, including a robust theoretical framework to describe the YIG–TMD heterostructure and its interaction with the probe laser. The results of the experiments show that the setup is capable of identifying and addressing TMD flakes, as well as exciting magnetostatic modes in the YIG film, however, subsequent experiments could not be performed due to delays resulting from the COVID-19 pandemic.

The thesis concludes by addressing the challenges encountered in the acquisition of the experimental results, and discussing future directions for successive experiments.

Sammendrag

Sterk kobling mellom heterogene kvantesystemer kan brukes til å konstruere hybridkvantesystemer, der de unike egenskapene til de individuelle systemene kan anvendes for innovative muligheter. Denne tesen gjør rede for et eksperiment med mål om å karakterisere koblingen mellom magnoner i en tynnfilm med yttrium-jern-granat (YIG) og eksitoner i atomisk tynne lag av et overgangsmetalldikalkogenid (TMD).

Magnoner er sterke kandidater for anvendelser i kvanteinformasjonsprosessering grunnet evne til å transportere informasjon uten å lide ohmske tap [1], samt at de kan kobles sterkt til superledende qubits [2]. TMDer, på den andre siden, er 2D-materialer med sterke optiske egenskaper og med mulige anvendelser i syntetisering av kunstige materialer med ekstraordinære egenskaper [3]. Om systemene kan kobles sterkt sammen vil det videre forsterke potensialet til begge systemer for nyskapende anvendelser, spesielt for magnon-baserte hybridsystemer da det kan forsterke optiske egenskaper, hvis svakhet tidligere har vært et hinder for enkelte anvendelser [4].

Det koblede systemet er en van der Waals-heterostruktur, konstruert ved å feste tynne flak av et TMD oppå en tynnfilm av YIG, der interaksjoner i overflaten fører til at resonansenergien til eksitonene kobles til den transversale magnetiseringen i YIG-filmen gjennom den magnetiske nærhetseffekten ('magnetic proximity effect'). Ved å magnetisere YIG-filmen parallelt med planaksen og eksitere magnoner, vil den oscillerende transversale magnetiseringen forårsaket av magnonene skifte resonansenergien til eksitonene dynamisk. Dersom man så belyser eksitonene med laserlys med en bestemt bølgelengde vil det dynamiske skiftet forplante seg i form av en amplitudemodulasjon i det reflekterte lyssignalet. Koblingen mellom magnonene og eksitonene kan så bestemmes ved å analysere dette signalet.

Tesen presenterer et eksperimentelt oppsett og et sett med eksperimenter som kan generere og analysere et slikt signal, og forankrer det i et robust teoretisk rammeverk for YIG-TMD heterostrukturen inklusiv interaksjon med signaler fra omgivelsene. De eksperimentelle resultatene viser at oppsettet er i stand til å identifisere, og kan anvendes på TMD-flak, i tillegg til å kunne eksitere magnetostatiske magnoner i YIG-filmen. Ytterligere planlagte eksperimenter kunne dessverre ikke gjennomføres grunnet COVID-19-pandemien.

Tesen konkluderer med en diskusjon om utfordringer som fremkom under eksperimentet, og mulige retninger for fremtidige eksperimenter.

Contents

List of Symbols and Abbreviations

$\boldsymbol{e}_x,\ \boldsymbol{e}_y,\ \boldsymbol{e}_z$	Unit vectors in the positive cartesian $x,\ y,\ z$ directions
$\hbar = 1.055 \times 10^{-34}\,\mathrm{J\,s}$	Reduced Planck's constant
$\mu_0 = 1.257 \times 10^{-6}\,\mathrm{H\,m^{-1}}$	Vacuum permeability
$e = 1.602 \times 10^{-19}\,\mathrm{C}$	Elementary charge
$m_\mathrm{e} = 9.109 \times 10^{-31}\,\mathrm{kg}$	Electron mass
$m_\mathrm{p} = 1.673 \times 10^{-27}\,\mathrm{kg}$	Proton mass

---

$\hat{a}^\dagger$	Hermitian conjugate of $\hat{a}$
a^*	Complex conjugate of a
$\dot{a}$	Time-derivative of a
$[\hat{a}, \hat{b}]$	Commutator between $\hat{a}$ and $\hat{b}$ equivalent to $\hat{a}\hat{b} - \hat{b}\hat{a}$

TMD	Transition metal dichalcogenide
YIG	Yttrium iron garnet
$MoSe_2$	Molybdenum diselenide
RWA	Rotating wave approximation
LWA	Long wavelength approximation
AC	Alternating current
DC	Direct current
AM	Amplitude modulation
PM	Phase modulation
EOM	Electro-optic modulator
AOM	Acousto-optic modulator
Ti:sapphire	Titanium–sapphire laser
FMR	Ferromagnetic resonance
HWP	Half-wave plate
QWP	Quarter-wave plate
PBS	Polarizing beam splitter

1. Introduction

From its humble theoretical beginnings in the early 20th century, quantum mechanics has come to dominate the cutting edge of modern technology. But as quantum systems are pushed to their limits, inherent limitations become obstacles hindering further development. Coupling separate quantum systems to construct hybrid quantum systems presents a way forward, as the unique strengths of the constituent systems can be leveraged to surpass individual shortcomings.

Taking as an example the leading implementation in the burgeoning field of quantum computation, superconducting qubit-based quantum computers, the nature of the inherent microwave communication and control presents substantial challenges to increasing the number of qubits and communication between separate quantum computers. This has led to a significant amount of research focused on constructing hybrid quantum systems that facilitate microwave-to-optical transduction, which would allow for the use of highly stable optical signals for quantum communication [5, 6].

Magnons, the quanta of collective spin excitations in magnetically-ordered systems, hold promise as platforms for information processing as well as hybrid quantum systems [1, 7]. Much like electrons in electronics, magnons can be used as information carriers to carry and store information, but do not suffer from the same drawbacks, such as Ohmic losses [1]. As magnonic modes can be coupled strongly to superconducting qubit-systems [2], they provide a gateway for the advancement of quantum computation and quantum sensing [7–9]. Though magnonic modes have wide applicability due to their intrinsic magnetic properties and microwave-domain radiative transitions, attempts at leveraging magneto-optic effects in magnon-based hybrid quantum systems has been limited by an inherently weak coupling [4], preventing access to the optical domain.

Group 6 transition metal dichalcogenides (TMDs) are two-dimensional semiconductors with direct band gaps. The band gaps support the creation of excitons, bound states of an electron and a hole, which constitute strong optical transitions. Exploiting the novel physical properties of TMDs and its excitonic modes holds great promise for applications in photonics and valleytronics [10,11], as well as hybrid quantum systems [6]. By stacking atomically thin layers of TMD togehter with other 2D materials such as graphene and hexagonal boron nitride(h-BN), or on top of a bulk substrate, one can create *van der Waals heterostructures* to enhance and alter their properties. This further expands the prospects of TMDs as a platform for developing functional and effective hybrid quantum systems [3, 12].

The resonance frequency of excitonic modes in TMDs can be coupled to an out-of-plane magnetization through the *magnetic proximity effect*, which is realized by piling a layer of TMD onto a magnetic substrate. By exciting magnons in the substrate, the oscillating magnetization will lead to a dynamic shift in the excitonic resonance energy, constituting a magnon–exciton coupling. The goal of the experiment detailed in this thesis is to characterize the coupling strength between the excitonic and magnonic modes, which

will determine the viability and effectiveness of magnon–exciton-based hybrid quantum systems.

1.1 Thesis overview

The structure of the thesis is as follows:

Chapter 2 presents the theoretical background of the thesis. The reader is first familiarized with the quantum mechanical description of the isolated magnon and exciton systems, and some of the properties of TMDs. The focus then shifts to the framework of open quantum systems and input–output theory, which acts as a starting point to introducing external coupling to an isolated system, and lays the foundation for the generation of an experimental signal. This framework is applied to the coupled magnon–exciton system, and input-output theory is used to derive an expression for the optical output-signal.

Chapter 3 details the construction of an experimental setup capable of generating such a signal, and the signal readout-scheme employed to extract the magnon–exciton coupling strength.

In Chapter 4, experimental results are presented and discussed. Unfortunately, the progress of the experiment was halted for a significant amount of time due to the COVID-19 pandemic, and as such, some of the experimental results could not be obtained in time. This chapter presents the experimental results that were obtained and details the planned procedures of the experiments that were to have taken place.

Chapter 5 presents a conclusion of the thesis, and discusses steps that may be taken to improve future experiments.

2. Theory

The aim of this thesis is to characterize a ferromagnet–TMD heterostructure, specifically how a magnon population in the ferromagnet affects the optical properties of the excitonic modes in the TMD. This chapter presents the reader with the theoretical background that is needed to understand the physics of the individual components and the coupling between them, and how the system can be experimentally probed to obtain information. Section 2.1 will present the Heisenberg picture-formulation of quantum mechanics, and the rotating wave approximation, both of which will dictate the form of the dynamics of the system. Section 2.2 will present the basic mechanisms of ferromagnetism which will be used to derive a model for magnons in a magnetostatic mode in a ferromagnet, and the dynamics of the induced magnetization. Section 2.3 will present a Hamiltonian for excitonic modes in semiconductors, and familiarize the reader with TMDs and their properties. Finally, Section 2.4 will introduce the framework of open quantum systems and input-output theory, which will be used to derive an expression for an optical output signal from the coupled magnon–exciton system.

2.1 The Heisenberg picture and the rotating wave approximation

The Heisenberg picture

In order to characterize the coupling between separate systems in a hybrid quantum system, it is instrumental that the dynamics of the system can be determined. However, the description and determination of the dynamics depend on the formulation of quantum mechanics employed.

There are three main formulations of quantum mechanics, the Schrödinger picture, the Heisenberg picture, and the interaction picture. In the Schrödinger picture, the state of the system is time-dependent whereas the quantum mechanical operators are time-independent. The dynamics are governed by the time-dependent Schrödinger equation

$$\hat{\mathrm{H}} \left|\psi(t)\right\rangle = i\hbar \frac{\partial}{\partial t} \left|\psi(t)\right\rangle , \tag{2.1}$$

where $|\psi(t)\rangle$ is the time-dependent state of the system, and $\hat{\mathrm{H}}$ is the time-independent Hamiltonian of the system. In the Heisenberg picture, however, the operators themselves are time-dependent, whereas the states are time-independent. The dynamics are then given by the equations of motion of the constituent operators, which are governed by the Heisenberg equation

$$\frac{\mathrm{d}\hat{\mathcal{O}}(t)}{\mathrm{d}t} = \frac{i}{\hbar}[\hat{\mathrm{H}}, \hat{\mathcal{O}}], \tag{2.2}$$

where $\hat{\mathcal{O}}$ is an operator in the Hamiltonian. The interaction picture can be seen as something in the middle, where both the states and the operators are time-dependent, but is not of interest for this thesis.

A time-dependent operator in the Heisenberg picture, $\hat{\mathcal{O}}(t)$, is related to a time-independent operator in the Schrödinger picture, $\hat{\mathcal{O}}$, as

$$\hat{\mathcal{O}}(t) = e^{i\hat{\mathrm{H}}t/\hbar}\hat{\mathcal{O}}e^{-i\hat{\mathrm{H}}t/\hbar}. \tag{2.3}$$

It is often notationally convenient to keep the time-dependence implicit, writing Heisenberg picture operators as $\hat{\mathcal{O}}(t)$, and using the relation Eq.(2.3) only when the explicit time-dependence is of interest.

A central difference between the dynamics as formulated in the Schrödinger and Heisenberg pictures is that the Schrödinger picture describes the combined mechanics of the total system, whereas the Heisenberg picture describes the coupled dynamics of the operators themselves. The Heisenberg picture is thus well-suited to describe the dynamics of individual degrees of freedom, which allows for the description of signals going into and coming out of a quantum mechanical system, as will be detailed in Section 2.4.

The rotating wave approximation

Generally, a coupling between quantum mechanical systems may include contributions of many forms, but it is often useful to approximate the coupling in terms of its dominant contributions. For Hamiltonians formulated in terms of creation and annihilation operators, this can be accomplished by employing the *rotating wave approximation* (RWA), which is widely used in the field of quantum optics [13, 14].

The rotating wave approximation is most easily explained in the Heisenberg picture, where the time-dependence of annihilation and creation operators takes the form of a complex exponential factor:

$$\hat{c}_j^{\pm}(t) \propto e^{\mp(iE_jt)/\hbar},$$

where E_j is the energy of the particle j, and the superscript $+$ $(-)$ denotes its creation (annihilation) operator. For products of creation and annihilation operators, each operator is accompanied by a complex exponential, resulting in the expectation value of product of exclusively creation (annihilation) operators being proportional to a complex exponential of the form

$$\left\langle \prod_j \hat{c}_j^{\pm} \right\rangle \propto \exp\Big(\mp i \sum_j E_j t/\hbar \Big).$$

In other words, these operators oscillate at a high frequency compared to linear terms and products of an equal number of creation and annihilation operators, and thus their contributions to the dynamics quickly average to zero. Neglecting the terms oscillating at higher frequencies constitutes the RWA.

2.2 Magnons in a ferromagnet

Magnons, also known as spin waves, are quanta of collective spin excitations in magnetically ordered systems. It is often convenient to distinguish between two types of magnonic modes, exchange spin waves and dipolar spin waves, for which the dynamics are dominated by exchange and dipolar interactions respectively, which relate to the interactions from which magnetic ordering in ferromagnets originates [1]. For the purposes of this thesis, the attention will be restricted to dipolar spin waves, also known as magnetostatic modes. As excitonic modes interact with magnons through the magnon-induced magnetization, it is of interest to characterize the relation between a magnon population and the magnetization in a ferromagnet. To elucidate the dynamics, the reader will first be presented with a recap of fundamental concepts in magnetism, and a quantum description of magnetic ordering in ferromagnets. The latter will also provide useful concepts for the description of physical phenomena in transition metal dichalcogenides.

2.2.1 Magnetic moments

The elementary unit in magnetic systems is the magnetic moment. Magnetic moments in atoms and molecules are generated by charged particles with an angular momentum. In quantum mechanics, total angular momentum, $\boldsymbol{J}$, is generally equal to the sum, $\boldsymbol{J} = \boldsymbol{L} + \boldsymbol{S}$, of the angular orbital momentum, $\boldsymbol{L}$, resulting from the orbital motion of the particle, and spin angular momentum, $\boldsymbol{S}$. As spin angular momentum has no classical analogue, we will for this introductory section restrict the attention to orbital angular momentum in order to elucidate the dynamics of magnetic moments. However, the expressions containing orbital angular momentum can easily be generalized by substituting the orbital angular momentum with total angular momentum, $\boldsymbol{L} \to \boldsymbol{J}$. This section draws inspiration from Chapter 1.2 and 1.3 in Ref. [15].

Charged particles in orbital motion will generate a magnetic moment $\boldsymbol{\mu} = IA\boldsymbol{e}_n$, proportional to the current I and area of the orbit $A\boldsymbol{e}_n$, where $\boldsymbol{e}_n$ is the unit vector perpendicular to the area. This magnetic moment will generate a magnetic dipole field, and interact with other magnetic moments and fields, experiencing the torque

$$\boldsymbol{\tau} = \boldsymbol{\mu} \times \boldsymbol{B}, \tag{2.4}$$

where $\boldsymbol{B}$ is the magnetic flux density at the position of the magnetic moment.

As the normal vector of the orbital is either parallel or antiparallel to the angular momentum vector of the charged particle, the magnetic moment $\boldsymbol{\mu}$ can be reexpressed in terms of angular momentum $\boldsymbol{L}$ as

$$\boldsymbol{\mu} = \pm\gamma\boldsymbol{L}, \tag{2.5}$$

where the sign is the same as the sign of the charge, and γ, a quantity known as the *gyromagnetic ratio*, has been introduced. This gyromagnetic ratio can be expressed as [15]:

$$\gamma = g\frac{|q|}{2m_q}, \tag{2.6}$$

where q and m_q are the charge and mass respectively of the charged particle, and the factor g is known as the *spectroscopic splitting* or simply the *g-factor*. The numerical value of the gyromagnetic ratio is dependent on the origin of the angular momentum, taking the value $g_S \approx 2$ for spin angular momentum, $\boldsymbol{S}$, and $g_L = 1$ for orbital angular

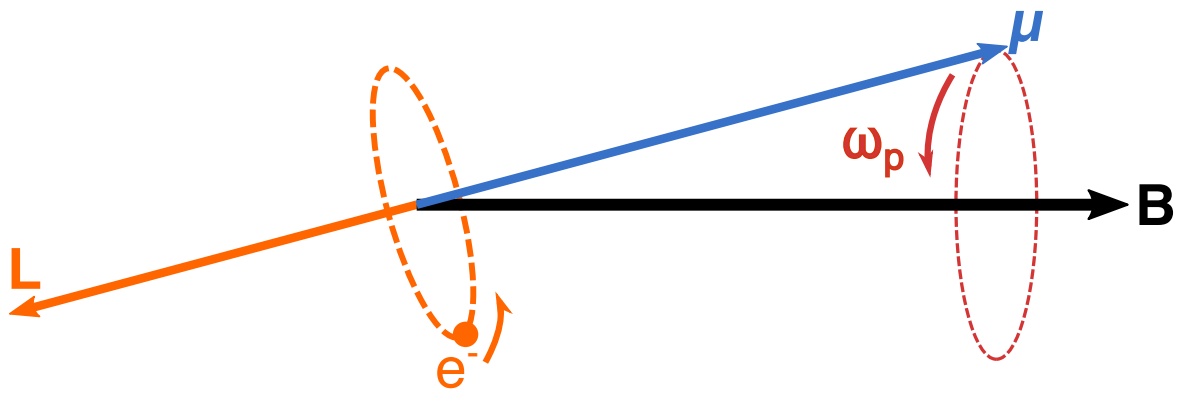

Figure 2.1: Illustration of a magnetic moment $\boldsymbol{\mu}$ induced by an electron in orbital motion. The magnetic moment precesses with precession frequency ω_p about an applied magnetic field with flux density $\boldsymbol{B}$.

momentum, $\boldsymbol{L}$. Though the charged particles in atoms and molecules, electrons and protons[1], both have non-zero angular momentum, the inverse mass dependence in Eq (2.6) means the magnetic moments of protons are negligible compared to the magnetic moments of electrons, as $m_\mathrm{p}/m_\mathrm{e} \approx 10^3$. Hence, proceeding, only the magnetic moments of the electrons will be considered[2].

Substituting Eq. (2.5) into Eq. (2.4) and reexpressing torque in terms of angular momentum yields for an electron:

$$\frac{d\boldsymbol{L}}{\mathrm{d}t} = -|\gamma|\boldsymbol{L} \times \boldsymbol{B}. \tag{2.7}$$

This equation has the same form as the equation of motion for a spinning top in a gravitational field, and as such this is a suitable classical analogue to picture the dynamics of magnetic moments in external magnetic fields. Similarly to the center of mass of a spinning top in a gravitational field, the magnetic moment will precess around an applied magnetic field with a precession frequency ω_P, which can be shown to be [15]:

$$\omega_P = |\gamma B|. \tag{2.8}$$

Unlike the case for the spinning top, this is independent of the angular momentum. The dynamics of a magnetic moment in an external magnetic field is illustrated in Fig. 2.1.

2.2.2 Origins of magnetic ordering

The magnetic properties of a volume of material can be characterized by the dynamics of the *magnetization*. The magnetization, $\boldsymbol{M}$, is defined as the net density of magnetic moments:

$$\boldsymbol{M} = \frac{1}{V}\sum_i \boldsymbol{\mu}_i, \tag{2.9}$$

where $\boldsymbol{\mu}_i$ is the magnetic moment of the ith electron, and V is the volume of the magnetic material. For there to be a net magnetization in a material there has to be some amount

[1]Neutrons also have a non-zero magnetic moment even though they are electrically neutral, owing to the magnetic moments of the charged quarks they are composed of. The magnetic moment of a neutron is quantitatively similar to that of a proton, so the same arguments will apply.

[2]It should, however, be noted that the magnetic moments of protons are important in other contexts, especially as they give rise to nuclear magnetic resonance (NMR)

of ordering in the magnetic moments, as opposing contributions would otherwise sum to zero.

Though one can generally split magnetic materials into various categories depending on the dynamics of the magnetization, we will in this thesis restrict the attention to ferromagnets, which exhibit a net magnetization both in the presence of an external magnetic field, called an *induced* magnetization, as well as in the absence of one, called a *spontaneous* magnetization[3]. From a quantum mechanical perspective, the magnetic ordering can be attributed to two contributions to the Hamiltonian: the Zeeman energy and the exchange interaction.

The Zeeman energy is related to the torque in Eq.(2.4), and can be shown to be [15]:

$$\hat{\mathrm{H}}_{\mathrm{Z}} = -\sum_i B\hat{\mu}_{i,z}, \tag{2.10}$$

where the sum is over all of the electrons in the material, and the z-axis is taken to be parallel to the magnetic flux density such that $\boldsymbol{B} = B\boldsymbol{e}_z$ with $\boldsymbol{e}_z$ the unit vector in the z direction. This means that it is energetically favorable for the magnetic moment to align with the applied magnetic field. The Zeeman energy by itself can explain an induced net magnetization in the presence of an external magnetic field. However, even though magnetic moments are sources of dipole magnetic fields, dipolar coupling between the magnetic moments alone is not strong enough to support long-range magnetic ordering against thermal disruption in the absence of external magnetic fields [16].

The origin of such spontaneous magnetic ordering is known as the *exchange interaction* which has the same physical origin as the Pauli exclusion principle. For neighboring electrons, the spatial wave function of the electrons must be either symmetric or antisymmetric for an antiparallel or parallel spin state respectively. The different spatial distribution leads to a difference in the Coulomb energy, which makes it energetically favorable for the spin of an electron to align either parallel or antiparallel to that of a neighboring electron [17]. The effect of the interaction between two electrons i and j can be modeled using the Heisenberg Hamiltonian, which is of the form

$$\hat{\mathrm{H}}_{\mathrm{e}} = -2J\hat{\boldsymbol{S}}_i \cdot \hat{\boldsymbol{S}}_j, \tag{2.11}$$

where the quantity J is detmermined by the *exchange integral* which depends on the overlap between the wave functions of the two particles. For a multidimensional lattice with N sites, the model can be extended to

$$\hat{\mathrm{H}}_{eN} = -\frac{2}{N}\sum_{\langle i,j\rangle} J_{i,j}\hat{\boldsymbol{S}}_i \cdot \hat{\boldsymbol{S}}_j, \tag{2.12}$$

where the sum is over all sites i and neighboring sites j denoted with the notation $\langle i,j\rangle$. This model assumes that all spins are localized at the sites of the crystal lattice; although the situation in a crystal is much more complicated than that, the Hamiltonian of Eq (2.12) nonetheless predicts many phenomena found in magnets, in particular the phenomena of interest for this thesis. For positive values of J, it will be energetically favorable for neighboring spins to align, resulting in a spontaneous magnetization even in the absence of external magnetic fields.

[3]This definition is also valid for ferrimagnets, which will be considered ferromagnets for the purposes of this thesis.

The total Hamiltonian of a ferromagnetic lattice can now be obtained as the sum of Eq (2.10) and Eq. (2.12). The presence of quantized collective spin excitations, also known as magnons, can then be derived using this as a starting point, resulting in a Hamiltonian of the form [Appendix A]

$$\hat{\mathrm{H}}_{\mathrm{magnon}} = \sum_k \hat{n}_{\boldsymbol{k}} \hbar \omega_{\boldsymbol{k}}. \tag{2.13}$$

where $\hat{n}_{\boldsymbol{k}}$ is the number operator of the magnonic mode with wave vector $\boldsymbol{k}$, and with $\hbar\omega_{\boldsymbol{k}}$ the energy of a single excitation.

2.2.3 Magnetization of magnetostatic modes in a ferromagnet

In order to characterize the magnon–exciton coupling, which originates from the out-of-plane magnetization stemming from the magnons in the magnetic material, the dynamics of the magnetization must be characterized. As the magnitude of the magnon-induced magnetization is highly dependent on the mean magnetization in the system, we will focus on the dynamics in an external magnetic field $\boldsymbol{H} = \boldsymbol{B}/\mu$, where $\boldsymbol{B}$ is the magnetic flux density and μ is the permeability of the medium. This section draws heavily on chapter 1.4-1.5 in [16].

It can be shown, that for the case where the magnetic field has a small harmonically time-dependent component, the magnetization will similarly have a small harmonically time-dependent component [Appendix B]. The oscillating magnetic field and magnetization can then be expressed as the real parts of complex vectors:

$$\begin{aligned} \boldsymbol{h}(t) &= \mathrm{Re}\{\boldsymbol{h}^C(t)\} = \mathrm{Re}\{\tilde{\boldsymbol{h}} e^{-i\omega t}\}, \\ \boldsymbol{m}(t) &= \mathrm{Re}\{\boldsymbol{m}^C(t)\} = \mathrm{Re}\{\tilde{\boldsymbol{m}} e^{-i\omega t}\}, \end{aligned} \tag{2.14}$$

where the complex amplitudes, $\tilde{\boldsymbol{h}}$ and $\tilde{\boldsymbol{m}}$, behave according to the linearized equation of motion

$$-i\omega\tilde{\boldsymbol{m}} + \gamma\mu_0 \tilde{\boldsymbol{m}} \times \boldsymbol{H}_0 = -\gamma\mu_0 \boldsymbol{M}_0 \times \tilde{\boldsymbol{h}}, \tag{2.15}$$

where $\boldsymbol{H}_0$ and $\boldsymbol{M}_0$ are the time-independent parts of the magnetic field and magnetization, respectively, which are assumed to be parallel.

Losses can be accounted for by the transformation [Appendix B]:

$$\gamma\mu_0 H_0 \to \gamma\mu_0 H_0 - i\alpha\omega, \tag{2.16}$$

where α is a dimensionless parameter which characterizes the rate of dissipation and depends on the material.

This equation can be concisely expressed using tensor notation

$$\tilde{\boldsymbol{m}} = \bar{\boldsymbol{\chi}} \tilde{\boldsymbol{h}}, \tag{2.17}$$

where the tensor $\bar{\boldsymbol{\chi}}$ is known as the *susceptibility tensor*. With the mean magnetic field and magnetization along the z-axis, the susceptibility tensor can be expressed as

$$\bar{\boldsymbol{\chi}} = \begin{pmatrix} \chi & -i\chi_{\mathrm{a}} & 0 \\ i\chi_{\mathrm{a}} & \chi & 0 \\ 0 & 0 & 0 \end{pmatrix}, \tag{2.18}$$

where, accounting for losses, the quantities $\chi = \chi' + i\chi''$ and $\chi_{\mathrm{a}} = \chi'_{\mathrm{a}} + i\chi''_{\mathrm{a}}$ are defined by the relations Eq. (B.25).

The linearized equation of motion thus leads to an induced time-dependent magnetization perpendicular to the mean magnetization, with no contributions from time-dependent components parallel to the time-independent part of the magnetic field.

Ferromagnetic resonance

At a specific frequency, $\omega = \omega_{\text{res}}$, the real part of χ_{a} changes sign, and the imaginary parts of χ and χ_{a} pass through a maximum. This frequency is denoted as the *resonance* and is defined by the relation:

$$\omega_{\text{res}}^2 = \frac{\omega_H^2}{1+\alpha^2}, \tag{2.19}$$

where $\omega_H \equiv \gamma\mu_0 H_0$. At resonance, the parameters in the susceptibility tensor have the following values [Eqs. (B.25)]:

$$\begin{aligned} \chi'_{\text{res}} &= \frac{\omega_M}{2\omega_H}, \\ \chi''_{\text{res}} &= \frac{\omega_M}{2\alpha\omega_{\text{res}}}, \\ \chi'_{\text{a,res}} &= 0, \\ \chi''_{\text{a,res}} &= \frac{\omega_M}{2\alpha\omega_H} \approx \chi''_{\text{res}}, \end{aligned} \tag{2.20}$$

where $\omega_M \equiv \gamma\mu_0 M_0$.

To see the result of the damped equation of motion on the time-dependent part of the magnetization one can inspect the time derivative of the oscillating magnetization components $\dot{m}_x$, $\dot{m}_y$ [Eq. (2.14)]:

$$\begin{aligned} \dot{m}_x(t) &= \text{Re}\{\dot{m}_x^C(t)\} = \text{Re}\{-i\omega\tilde{m}_x e^{-i\omega t}\} \\ &= \text{Re}\Big\{ -i\omega\Big[(\chi' + i\chi'')\tilde{h}_x + e^{-i\pi/2}(\chi'_{\text{a}} + i\chi''_{\text{a}})\tilde{h}_y\Big]e^{-i\omega t}\Big\} \\ &= \text{Re}\Big\{ -i\omega\Big(\chi'\tilde{h}_x + e^{-i\pi/2}\chi'_{\text{a}}\tilde{h}_y\Big)e^{-i\omega t} + \omega\Big(\chi''\tilde{h}_x + e^{-i\pi/2}\chi''_{\text{a}}\tilde{h}_y\Big)e^{-i\omega t}\Big\} \\ &= \text{Re}\Big\{ -i\omega\Big(\chi'\tilde{h}_x + e^{-i\pi/2}\chi'_{\text{a}}\tilde{h}_y\Big)e^{-i\omega t}\Big\} + \omega\chi''\text{Re}\Big\{\tilde{h}_x e^{-i\omega t}\Big\} + \omega\chi''_{\text{a}}\text{Re}\Big\{e^{-i(\omega t - \frac{\pi}{2})}\Big\} \\ &= \omega\chi'' h_x(t) + \omega\chi''_{\text{a}} h'_y(t) + \text{Re}\Big\{ -i\omega\Big(\chi'\tilde{h}_x + e^{-i\pi/2}\chi'_{\text{a}}\tilde{h}_y + \Big)e^{-i\omega t}\Big\}, \\ &= \omega\chi'' h_x(t) + \omega\chi''_{\text{a}} h'_y(t) + \chi'\dot{h}_x(t) + \chi'_{\text{a}}\dot{h}'_y(t), \end{aligned} \tag{2.21}$$

where $h'_y(t)$ is $-\pi/2$ out of phase with $h_y(t)$. This means positive χ''_{res} and $\chi''_{\text{a,res}}$ lead to the magnetization increasing proportionally to the oscillating magnetic field. In other words, the magnetization is absorbing magnetic energy from the oscillating magnetic field. This phenomenon is called *ferromagnetic resonance*, and can be measured experimentally. As χ''_{res}, $\chi''_{\text{a,res}}$ are inversely proportional to the rate of dissipation α, a lower rate of dissipation will lead to higher rate of absorption of energy at resonance [Eq. (2.20)].

Uniform-precession magnetostatic mode

In order to determine the spatial distribution of the total magnetic field $\boldsymbol{H}$, it is generally required that one solves Maxwell's equations for the appropriate boundary conditions. Thus, the geometry of the ferromagnet must be known in order to determine the dynamics of the system.

The simplest case to solve is the uniform-precession mode, also known as the Kittel mode, in ellipsoidal samples in a uniform applied magnetic field. In this mode, all

magnetic moments in the magnet precess uniformly and in phase, as is illustrated in Fig. 2.2.

The uniform-precession mode is a magnetostatic mode, which is valid in the magnetostatic approximation to Maxwell's equations. In this approximation, the spatial dependence of the magnetic field is assumed to vary sufficiently slowly to approximate it as constant in space in Maxwell's equations [15]. As exchange interactions are very short-ranged and thus lead to high-frequency spatial variation, they must contribute negligibly to magnetostatic modes compared to the long-ranged dipolar interactions. Hence, magnetostatic modes are also commonly referred to as dipolar spin waves.

In the case of the uniform-precession mode, the total magnetic field can be written as [16]:

$$\boldsymbol{H} = \boldsymbol{H}_{\mathrm{e}} - \bar{\boldsymbol{N}}\boldsymbol{M}, \tag{2.22}$$

where the subscript e denotes an external field, and $\bar{\boldsymbol{N}}$ is the *demagnetization tensor*. The demagnetization tensor is diagonal in the axes of the ellipsoid:

$$\bar{\boldsymbol{N}} = \begin{pmatrix} N_x & 0 & 0 \\ 0 & N_y & 0 \\ 0 & 0 & N_z \end{pmatrix}, \tag{2.23}$$

where N_x, N_y, N_z are known as the *demagnetization factors*, which depend on the shape of the ellipsoid and are generally required to sum up to 1:

$$N_x + N_y + N_z = 1. \tag{2.24}$$

The time-independent part $\boldsymbol{H_0}$ and time-dependent part $\boldsymbol{h}$ can then be expressed as

$$\boldsymbol{H}_0 = \boldsymbol{H}_{0\mathrm{e}} - \bar{\boldsymbol{N}}\boldsymbol{M}_0, \tag{2.25}$$

$$\boldsymbol{h} = \boldsymbol{h}_{\mathrm{e}} - \bar{\boldsymbol{N}}\boldsymbol{m}. \tag{2.26}$$

In order for the magnetostatic approximation to be valid, the sample size must be small compared to the wavelength of the external oscillating magnetic field $\boldsymbol{h}_{\mathrm{e}}$ in the sample. Furthermore, the oscillating magnetization must be uniform across the sample.

For the case of a thin circular disk[4], a limiting case of an ellipsoid, in the xz-plane with the z-axis aligned parallel with the external magnetic field, $\boldsymbol{H}_{0\mathrm{e}} = H_0\boldsymbol{e}_z$, the demagnetization factors are [16]:

$$N_x = 0,\ N_y = 1,\ N_z = 0.$$

Suppose the time-dependent part of the magnetic field is normal to the disk, $\boldsymbol{h}_{\mathrm{e}} = \begin{pmatrix} 0 \\ h_y \\ 0 \end{pmatrix}$, as illustrated in Fig. 2.2. The quantities $\boldsymbol{H}_0$ and $\boldsymbol{h}$ can then be expressed as

[4]Ref. [15] presents the same result for thin films without referencing the geometry, and other papers have made use of similar modes for rectangular films [18]. As such it will be assumed that the thin films need not necessarily be circular.

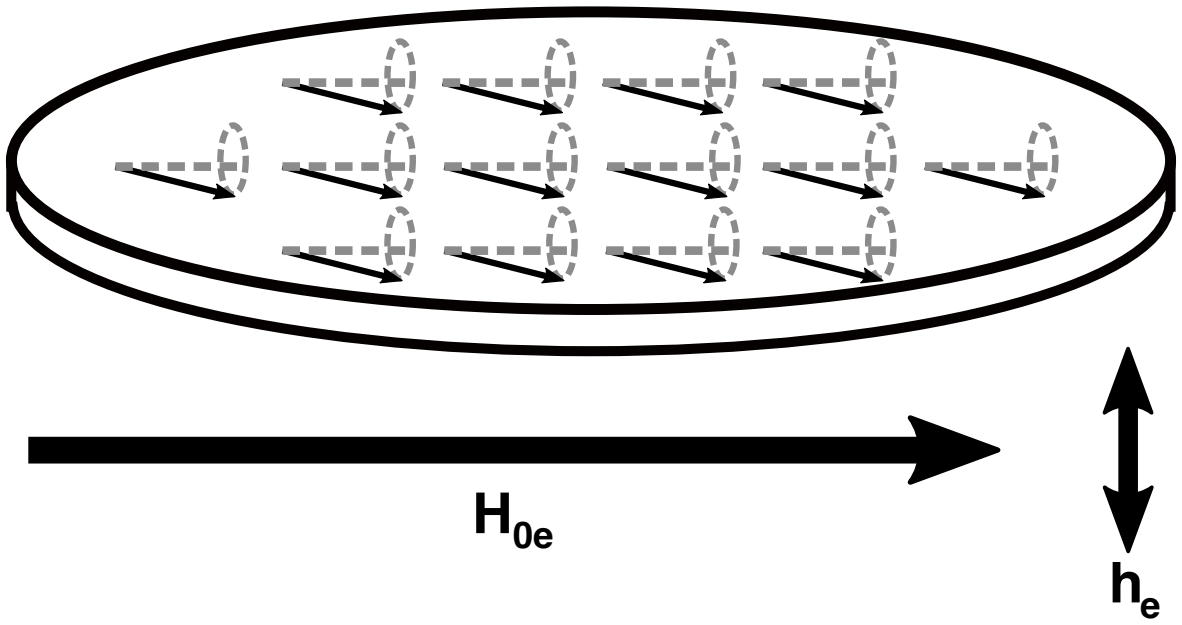

Figure 2.2: Illustration of the uniform-precession magnetostatic mode in a thin circular disk. The static component of the applied magnetic field, $\boldsymbol{H}_{0\mathrm{e}}$ is parallel to the z-axis, whereas the harmonically oscillating component $\boldsymbol{h}_{\mathrm{e}}$ is aligned with the y-axis. The magnetic moments in the thin circular disk will then precess uniformly in phase about the mean magnetization, which is parallel to the applied magnetic field.

$$\begin{aligned}\boldsymbol{H}_0 &= \begin{pmatrix}0\\0\\H_0\end{pmatrix} - \begin{pmatrix}0&0&0\\0&1&0\\0&0&0\end{pmatrix}\begin{pmatrix}0\\0\\M_0\end{pmatrix}\\ &= \begin{pmatrix}0\\0\\H_0\end{pmatrix}, \end{aligned} \tag{2.27}$$

$$\begin{aligned}\boldsymbol{h} &= \begin{pmatrix}0\\h_y\\0\end{pmatrix} - \begin{pmatrix}0&0&0\\0&1&0\\0&0&0\end{pmatrix}\begin{pmatrix}m_x\\m_y\\m_z\end{pmatrix}\\ &= \begin{pmatrix}0\\h_y - m_y\\0\end{pmatrix}. \end{aligned} \tag{2.28}$$

Substituting into the undamped linearized equation of motion (B.10) yields:

$$\begin{aligned}-i\omega\tilde{m}_x + \omega_H\tilde{m}_y &= \omega_M(\tilde{h}_y - \tilde{m}_y)\\ -i\omega\tilde{m}_y - \omega_H\tilde{m}_x &= 0.\end{aligned} \tag{2.29}$$

The solutions to this equation are

$$\begin{aligned}\tilde{m}_x &= -\frac{i\omega_M\omega}{\omega_H(\omega_H+\omega_M)-\omega^2}\tilde{h}_y,\\ \tilde{m}_y &= \frac{1}{\omega_H(\omega_H+\omega_M)-\omega^2}\omega_M\omega_H\tilde{h}_y.\end{aligned} \tag{2.30}$$

From this we can identify the susceptibility tensor as

$$\begin{aligned}\bar{\boldsymbol{\chi}} &= \begin{pmatrix} 0 & -i\omega_M\omega/\Big(\omega_H(\omega_H+\omega_M)-\omega^2\Big) & 0 \\ 0 & \omega_M\omega_H/\Big(\omega_H(\omega_H+\omega_M)-\omega^2\Big) & 0 \\ 0 & 0 & 0 \end{pmatrix} \\ &= \begin{pmatrix} 0 & -i\chi_\mathrm{a} & 0 \\ 0 & \chi & 0 \\ 0 & 0 & 0 \end{pmatrix}. \end{aligned} \tag{2.31}$$

As the amplitude of the ratio $|\tilde{m}_x/\tilde{m}_y| = \omega/\omega_H \neq 1$, the oscillating out-of-plane component of the magnetization will trace an ellipse in the xy-plane.

Taking losses into account, the susceptibility χ (χ_a) can be decomposed into its real and imaginary parts $\chi = \chi' + i\chi''$ ($\chi = \chi'_\mathrm{a} + i\chi''_\mathrm{a}$), where the components can be written as

$$\begin{aligned} \chi' &= \frac{1}{D}\omega_H\omega_M\Big[\omega_H(\omega_H+\omega_M)-(1-\alpha^2)\omega^2\Big] + \frac{1}{D}\alpha^2\omega^2\omega_M^2, \\ \chi'' &= \frac{1}{D}\alpha\omega_M\omega\Big[\omega_H^2+(1+\alpha^2)\omega^2\Big], \\ \chi'_a &= \frac{1}{D}\omega_M\omega\Big[\omega_H(\omega_H+\omega_M)-(1+\alpha^2)\omega^2\Big], \\ \chi''_a &= \frac{1}{D}\alpha\omega_M\omega^2(2\omega_H+\omega_M), \\ D &= \Big[\omega_H(\omega_H+\omega_M)-(1+\alpha^2)\omega^2\Big]^2 + \alpha^2\omega^2(2\omega_H+\omega_M)^2. \end{aligned} \tag{2.32}$$

The resonance frequency of the uniform-precession mode is then the frequency at which the imaginary components, χ'' and χ''_a, pass through a maximum, which can be identified as

$$\omega_\mathrm{res}^2 = \frac{\omega_H(\omega_H+\omega_M)}{1+\alpha^2}. \tag{2.33}$$

Magnons in the uniform-precession magnetostatic mode

For the description of the coupled magnon–exciton system it is of interest to characterize the magnetization of the uniform-precession magnetostatic mode in terms of magnon creation and annihilation operators. In the following derivation, it will be assumed that the uniform-precession mode is driven with a classical radiation field, as is the case in the experiment in this thesis, such that the system is in a coherent state. This state of the quantum uniform-precession mode will have the same properties as before, as coherent states follow Maxwell's equations.

Supposing, as in the previous section, that the magnet is placed in an external magnetic field, and further imposing a temperature of $T = 0\,\mathrm{K}$ and an absence of driving, all of the magnetic moments in the material will align along the external magnetic field $\boldsymbol{H}_0 = H_0\boldsymbol{e}_z$, such that the magnetization of the material can be written as [Eqs. (2.5), (2.9)]:

$$M_z = \gamma\frac{\hbar}{2}\frac{N}{V}, \tag{2.34}$$

where the total angular momentum at a site has been assumed to be equal to $\frac{1}{2}$ for simplicity, and N is the number of magnetic moments.

In the uniform-precession mode, all magnetic moments precess uniformly in phase such that the magnetization is uniform throughout the volume of the magnet at any given time. This allows for the magnetic moments, or correspondingly, angular momentum to be treated collectively, similar to the treatment in Ref. [19]. The system is then treated as a *Dicke state*, named after the paper first detailing such a treatment, Ref. [20]. For such a system, the square of the total angular momentum can be written as [19]:

$$\boldsymbol{J}^2 = \hbar^2 \frac{N}{2}\left(\frac{N}{2}+1\right), \tag{2.35}$$

which corresponds to treating the spins collectively by transforming the eigenvalues of the total angular momentum operator $J \to NJ = \frac{N}{2}$. This allows for the total magnetization to be written as

$$\boldsymbol{M}^2 = \frac{1}{V^2}\gamma^2\hbar^2 \frac{N}{2}\left(\frac{N}{2}+1\right). \tag{2.36}$$

As the excitation of magnons in an in-plane magnetized substrate would increase the transverse component of the magnetization, the transverse magnetization should be expressible in terms of magnon creation and annihilation operators. To this end, the square of the total magnetization is expanded in terms of the components transverse and parallel to the applied magnetic field, yielding [Eq. (2.36)]

$$M_t^2 + M_z^2 = \frac{1}{V}\gamma^2\hbar^2 \frac{N}{2}\left(\frac{N}{2}+1\right), \tag{2.37}$$

where M_t is the transverse magnetization. The non-zero transverse component in the absence of driving and thermal fluctuations can be interpreted as the result of vacuum fluctuations of a magnonic mode. Substituting in the expression Eq. (2.34), the transverse magnetization can then be expressed as

$$M_t = \gamma \frac{\hbar}{2}\frac{\sqrt{N}}{V}. \tag{2.38}$$

In order to proceed, it is useful to specify a basis in which the transverse component is expressed. A conventional choice would be to express the magnetization in terms of the Cartesian x- and y-components:

$$M_t^2 = m_x^2 + m_y^2, \tag{2.39}$$

however, it can just as easily be expressed in the $m_\pm$ basis, specified similarly to the spin $\pm$ basis Eq. (A.2):

$$m_\pm = m_x \pm i m_y. \tag{2.40}$$

In this basis, the square of the transverse magnetization reads:

$$M_t^2 = \frac{1}{2}(m_+ m_- + m_- m_+), \tag{2.41}$$

which means the transverse magnetization can be written as

$$M_t = \sqrt{\frac{1}{2}(m_+ m_- + m_- m_+)}. \tag{2.42}$$

By treating the magnetization components m_+ and m_- as proportional to collective spin operators in a similar manner to $\hat{S}_+$ and $\hat{S}_-$ in Appendix A, the ansatz is made that the magnetization operators $\hat{m}_+$ and $\hat{m}_-$ may be written as

$$\begin{aligned} \hat{m}_+ &= \frac{1}{V}\gamma\frac{\hbar}{2}\sqrt{2N}\hat{a}^\dagger, \\ \hat{m}_- &= \frac{1}{V}\gamma\frac{\hbar}{2}\sqrt{2N}\hat{a}, \end{aligned} \tag{2.43}$$

where $\hat{a}$ ($\hat{a}^\dagger$) is a magnon annihilation operator (creation operator). From Appendix A we know that the creation of a magnon lowers the magnetization parallel to an external magnetic field. Eqs. (2.43) similarly state that the operator $\hat{m}_+$ raises the *transverse* magnetization, by creating a magnon. Substituting into Eq. (2.42) we obtain the operator-valued equation:

$$\begin{aligned} \hat{M}_t &= \gamma\frac{\hbar}{2}\frac{\sqrt{N}}{V}\sqrt{\hat{a}^\dagger\hat{a} + \hat{a}\hat{a}^\dagger} \\ &= \gamma\frac{\hbar}{2}\frac{\sqrt{N}}{V}\sqrt{2\hat{n}+1}, \end{aligned} \tag{2.44}$$

where $\hat{n} \equiv \hat{a}^\dagger\hat{a}$ is the number operator. At $T = 0\,\mathrm{K}$ and no driving, there should be no magnons in the system, meaning the expectation value $\langle\hat{n}\rangle = 0$, which allows for Eq. (2.38) to be recovered from Eq. (2.44).

An equation of motion for the annihilation operator $\hat{a}$ can now be obtained by reexpressing the equation of motion of the uniform-precession mode in terms of m_-. To this end we will follow an approach similar to the treatment of Eq. (2.29). Using instead the time-space linearized equation of motion yields [Eq. (B.7)]

$$\begin{aligned} \dot{\tilde{m}}_x &= -(\omega_M + \omega_H)\tilde{m}_y + \omega_H\tilde{h}_y, \\ \dot{\tilde{m}}_y &= \omega_H\tilde{m}_x. \end{aligned} \tag{2.45}$$

In order to express this in the $m_\pm$ basis, the Cartesian components will have to be scaled in such a way that they can be written as

$$\begin{aligned} \dot{\mathcal{M}}_x &= -\omega_S\mathcal{M}_y + \omega_H\tilde{h}_{S,y}, \\ \dot{\mathcal{M}}_y &= \omega_S\mathcal{M}_x, \end{aligned} \tag{2.46}$$

where $\tilde{h}_{S,y}$ is a scaled magnetic field amplitude, and the scaled components of the magnetization are defined as

$$\begin{aligned} \mathcal{M}_x &= A_1\tilde{m}_x, \\ \mathcal{M}_y &= A_2\tilde{m}_y. \end{aligned} \tag{2.47}$$

Combining Eqs. (2.46) and (2.47) yields the relation:

$$\omega_S = (\omega_M + \omega_H)\frac{A_1}{A_2} = \omega_H\frac{A_2}{A_1} \tag{2.48}$$

which has the solution for ω_S:

$$\omega_S = \sqrt{\omega_H(\omega_M + \omega_H)}, \tag{2.49}$$

which corresponds to the resonance frequency of the uniform-precession mode, Eq. (2.33), with losses neglected. The equation of motion of the scaled magnetization $\mathcal{M}_- \equiv \mathcal{M}_x - i\mathcal{M}_y$, can then be written as

$$\begin{aligned}\dot{\mathcal{M}}_- =& -\omega_S\mathcal{M}_y - i\omega_S\mathcal{M}_x + \omega_H A_1\tilde{h}_y \\ =& -i\omega_S\mathcal{M}_- + \omega_H A_1\tilde{h}_y.\end{aligned} \tag{2.50}$$

Accounting for losses corresponds to the transformation:

$$\begin{aligned}&\omega_S \to \sqrt{(\omega_H - i\alpha\omega)(\omega_H - i\alpha\omega + \omega_M)} = \omega'_S - i\omega''_S, \\ &\omega'_S \equiv \mathrm{Re}(\sqrt{(\omega_H - i\alpha\omega)(\omega_H - i\alpha\omega + \omega_M)}), \\ &\omega''_S \equiv -\mathrm{Im}(\sqrt{(\omega_H - i\alpha\omega)(\omega_H - i\alpha\omega + \omega_M)}).\end{aligned} \tag{2.51}$$

The equation of motion of the magnetization $\mathcal{M}_-$ with losses can then be identified as

$$\dot{\mathcal{M}}_- = -i\omega'_S\mathcal{M}_- - \omega''_S\mathcal{M}_- + (\omega_H - i\alpha\omega)A_1\tilde{h}_y. \tag{2.52}$$

As the magnetic field h_y is proportional to the radiation field it stems from [21], the magnetic field amplitude $\tilde{h}_y$ can be written in terms of the photon flux of the originating radiation, l_{in}, as

$$\tilde{h}_y = \beta l_{\mathrm{in}}, \tag{2.53}$$

where β is the proportionality constant. By replacing the magnetization with the annihilation operator of the magnon using Eq. (2.43) and substituting a quantized version of Eq. (2.53) for the magnetic field amplitude yields an equation of motion for the magnon annihilation operator [Eq. (2.52)]:

$$\begin{aligned}\dot{\hat{a}} =& -\underbrace{i\omega'_S}_{i\omega_0}\hat{a} - \underbrace{\omega'_S}_{\frac{\gamma_T}{2}}\hat{a} + \underbrace{\omega_H\beta A_1\frac{2V}{\hbar\gamma\sqrt{2N}}}_{\sqrt{\gamma_e}}\hat{l}_{\mathrm{in}} \\ =& -i\omega_0\hat{a} - \frac{\gamma_T}{2}\hat{a} + \sqrt{\gamma_{\mathrm{mw}}}\hat{l}_{\mathrm{in}},\end{aligned} \tag{2.54}$$

where the quantities $\omega_0, \gamma_T, \gamma_{\mathrm{mw}}$ can be determined experimentally. This equation is called the *quantum Langevin equation* of the magnonic mode, which will be discussed in more detail in Section 2.4.

2.3 Excitons in transition metal dichalcogenides

Transition metal dichalcogenides is a family of 2D materials which contains a number of semiconductors. By shining light with a specific frequency at such a semiconductor one can create a bound state known as an *exciton*, consisting of an excited valence electron electrostatically bound to the hole it leaves behind. The presence of excitonic modes provides semiconductor transition metal dichalcogenides with a strong optical response, which can be combined with other properties to construct novel and effective quantum hybrid systems. This section will start by presenting a derivation of the excitonic Hamiltonian from a quantum mechanical description of a semiconductor system interacting with classical light. Proceeding, the section will acquaint the reader with the properties of transition metal dichalcogenides, which will present a way to couple the excitonic modes in transition metal dichalcogenides to magnonic modes in a ferromagnet.

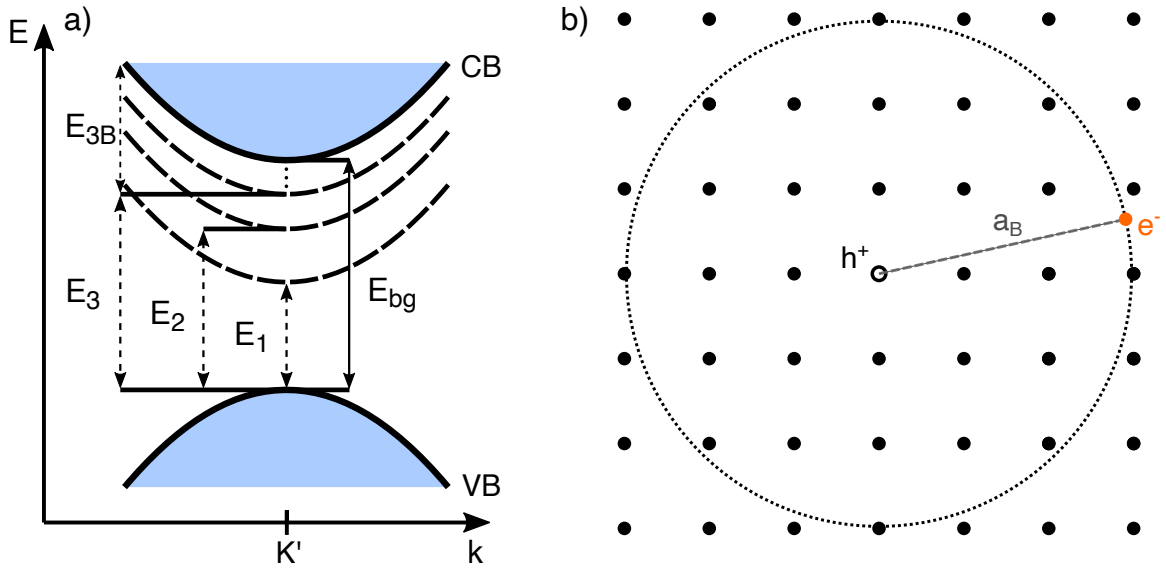

Figure 2.3: a) Illustration of the band structure of a semiconductor with a direct band gap. The resonance energy of the exciton with quantum numbers n is denoted as E_n, whereas the band gap energy is denoted as E_{bg}. The binding energy of the exciton with quantum number $n = 3$ is also shown, denoted as $E_{3\mathrm{B}}$. b) Illustration of the constituent bound electron and hole of a Wannier-Mott exciton, colored orange and white respectively. The Bohr-radius a_{B} of the exciton state is several times larger than the lattice parameter.

2.3.1 Quantum mechanical description of excitons in a semiconductor

In order to describe the dynamics of a magnon–exciton hybrid quantum system, a Hamiltonian for the excitonic modes is needed. To this end, we will first derive a quantum mechanical Hamiltonian of a semiconductor interacting with coherent light in terms of creation and annihilation operators of valence and conduction band electrons. The resulting dynamics will then be used to reexpress the Hamiltonian in terms of exciton creation and annihilation operators. The derivation is an adapted approach from chapter 10 of Ref. [22] combined with elements from chapters 10 and 11 of Ref. [23]. The spin index will be absorbed into the wave vector $\boldsymbol{k}$ for simplicity of notation. Though it generally is possible to excite valence band electrons into states with the opposite spin, such transitions are dipole-forbidden and thus depend on relatively weak interactions. The

corresponding excitonic modes, aptly named *dark exciton* modes, will be neglected due to their significantly lower optical response.

Hamiltonian and dynamics in terms of electronic operators

For a semiconductor system with single valence and conduction bands, the Hamiltonian and the dynamics of the system are most easily expressed in terms of creation and annihilation operators of valence and conduction band electrons, which are quasiparticles representing electrons confined to their given band. Furthermore, it is convenient to replace the valence band electron operators with valence band *hole* operators, which are defined by the following relations [Eq. (C.2)]:

$$\begin{aligned} \hat{c}_{\mathrm{h},\boldsymbol{k}} &= \hat{c}^{\dagger}_{\mathrm{v},-\boldsymbol{k}}, \\ \hat{c}^{\dagger}_{\mathrm{h},\boldsymbol{k}} &= \hat{c}_{\mathrm{v},-\boldsymbol{k}}, \end{aligned} \tag{2.55}$$

where the subscript h (v) denotes the operator for a valence band hole (electron), and $\boldsymbol{k}$ is the quantum number of the particle, which is assumed to correspond to the wave vector and spin.

The Hamiltonian of a semiconductor interacting with light can be written as [Appendix C]

$$\begin{aligned} \hat{\mathrm{H}} = &\sum_{\boldsymbol{k}} \left(\varepsilon_{\mathrm{c},\boldsymbol{k}} \hat{c}^{\dagger}_{\mathrm{c},\boldsymbol{k}} \hat{c}_{\mathrm{c},\boldsymbol{k}} + \varepsilon_{\mathrm{h},\boldsymbol{k}} \hat{c}^{\dagger}_{\mathrm{h},\boldsymbol{k}} \hat{c}_{\mathrm{h},\boldsymbol{k}} \right) \\ &+ \frac{1}{2} \sum_{\boldsymbol{k},\boldsymbol{k}'\boldsymbol{q}\neq 0} V(\boldsymbol{q}) \Big(\hat{c}^{\dagger}_{\mathrm{c},\boldsymbol{k}+\boldsymbol{q}} \hat{c}^{\dagger}_{\mathrm{c},\boldsymbol{k}'-\boldsymbol{q}} \hat{c}_{\mathrm{c},\boldsymbol{k}'} \hat{c}_{\mathrm{c},\boldsymbol{k}} \\ &+ \hat{c}_{\mathrm{h},\boldsymbol{k}+\boldsymbol{q}} \hat{c}_{\mathrm{h},\boldsymbol{k}'-\boldsymbol{q}} \hat{c}^{\dagger}_{\mathrm{h},\boldsymbol{k}'} \hat{c}^{\dagger}_{\mathrm{h},\boldsymbol{k}} \\ &+ 2 \hat{c}^{\dagger}_{\mathrm{c},\boldsymbol{k}+\boldsymbol{q}} \hat{c}_{\mathrm{h},\boldsymbol{k}'-\boldsymbol{q}} \hat{c}^{\dagger}_{\mathrm{h},\boldsymbol{k}'} \hat{c}_{\mathrm{c},\boldsymbol{k}} \Big) \\ &+ \sum_{\boldsymbol{k}} \hbar (g_{\omega_d} \hat{c}^{\dagger}_{\mathrm{c},\boldsymbol{k}} \hat{c}^{\dagger}_{\mathrm{h},-\boldsymbol{k}} e^{-i\omega_d t} + \mathrm{h.c.}). \end{aligned} \tag{2.56}$$

Here, the first two terms constitute the unperturbed Hamiltonian of the two-band semiconductor, where $\hat{c}_{\mathrm{c},\boldsymbol{k}}$ and $\varepsilon_{\mathrm{c},\boldsymbol{k}}$ ($\hat{c}_{\mathrm{h},\boldsymbol{k}}$ and $\varepsilon_{\mathrm{h},\boldsymbol{k}}$) is the annihilation operator and energy, respectively, of a conduction band electron (valence band hole) with quantum number $\boldsymbol{k}$ hereafter simply referred to as electron (hole). The quantity $V(q)$ in the second term is the Fourier transform of the Coulomb potential. The last term represents the interaction with the coherent light with frequency ω_{d}, also referred to as the optical drive. The interaction is characterized by the coupling strength $g_{\omega_{\mathrm{d}}}$, which is proportional to the electric field strength of the light and dipole moment between the electrons and the holes.

The dynamics of the semiconductor–light system can be obtained by inspecting the *semiconductor Bloch equations*. The semiconductor Bloch equations are the coupled equations of motion of the expectations values of the electron and hole populations, $n_{\mathrm{c},\boldsymbol{k}} \equiv \langle \hat{c}^{\dagger}_{\mathrm{c},\boldsymbol{k}} \hat{c}_{\mathrm{c},\boldsymbol{k}} \rangle$ and $n_{\mathrm{c},\boldsymbol{k}} \equiv \langle \hat{c}^{\dagger}_{\mathrm{h},-\boldsymbol{k}} \hat{c}_{\mathrm{h},-\boldsymbol{k}} \rangle$, and the pair operator, $P_{\mathrm{ch},\boldsymbol{k}} \equiv \langle \hat{c}_{h,-\boldsymbol{k}} \hat{c}_{c,\boldsymbol{k}} \rangle$. The semiconductor Bloch equations can be derived from the Hamiltonian Eq. (2.56), which is shown in Appendix C. For the experiment detailed in this thesis, we are interested in the dynamics in the *ultralow density regime*, where the electron and hole populations are low enough to be neglected, such that the dynamics of the system are determined only by the equation of motion of the expectation value of the pair operator. This equation

of motion can be written as [Eq. (C.10)]]:

$$\frac{dP_{\mathrm{ch}}(\boldsymbol{r})}{\mathrm{d}t} = -\frac{i}{\hbar}(E_{\mathrm{g}} + \frac{\hbar^2}{2m_r^*}\nabla^2 + V_{\mathrm{Coulomb}})P_{\mathrm{ch}}(\boldsymbol{r}) + ig_{\omega_{\mathrm{d}}}\delta(\boldsymbol{r})V_{\mathrm{c}}, \tag{2.57}$$

where E_{g} is the band gap energy, V_{Coulomb} is the Coulomb energy of the electron–hole pair, V_{c} is the quantization volume, and the energy of the conduction-band electrons and holes has been written in terms of the energy of effective single particle states with a reduced mass $m_{\mathrm{c}}^* = m_{\mathrm{c}}m_{\mathrm{h}}/(m_{\mathrm{c}} + m_{\mathrm{h}})$, where m_{c} and m_{h} are the effective masses of the electron and hole quasiparticles. The solutions of this inhomogeneous linear differential equation can be expressed in terms of solutions of the corresponding homogeneous differential equation, which satisfies [22, 23]:

$$-\Big[\frac{\hbar^2}{2m_r^*}\nabla^2 + V_{\mathrm{Coulomb}}(\boldsymbol{r})\Big]\psi_n(\boldsymbol{r}) = E_n\psi_n(\boldsymbol{r}), \tag{2.58}$$

where $\psi_n(\boldsymbol{r})$ is the wave function of a combined electron-hole quasiparticle with quantum number n. This equation is known as the *Wannier equation*, and was derived under the assumption that the total variation of the Coulomb potential within the extent of the wave function is small, which is valid as long as the average separation between the conduction-band electron and the hole, i.e. their Bohr radius, is large compared to the lattice parameter [23]. The energy spectrum consists of a discrete part, where $E_n < 0$, corresponding to the case where the Coulomb attraction is strong enough to bind the constituent electron and hole in a hydrogen-like state with a hydrogenic energy spectrum, and a continuous part, where $E_n > 0$ [22]. The bound states with a discrete energy spectrum is commonly referred to as *Wannier* or *Wannier-Mott* excitons. The Wannier equation describes excitons in both 2D and 3D materials, where the two cases have slightly different energy spectrums in terms of the dependence on the quantum number n [23]:

$$E_n^{3D} \propto \frac{1}{n^2} \tag{2.59}$$

$$E_n^{2D} \propto \frac{1}{(n+1/2)^2}. \tag{2.60}$$

An illustration of a Wannier-Mott exciton and the band structure of excitonic modes is shown in Fig. 2.3.

Hamiltonian in terms of excitonic operators

As the wave functions of the excitons satisfy the homogeneous equation of motion, a Hamiltonian constructed from exciton annihilation and creation operators should yield the same equations of motion as Eq. (2.56). The total Hamiltonian may then be expressed in terms of exciton operators if a relation between exciton operators and electron and hole operators is found. The creation of an exciton with quantum number ν and wave vector $\boldsymbol{K}$ can be expressed in bra-ket notation as

$$\hat{C}_{\nu,\boldsymbol{K}}^{\dagger} = |\nu, \boldsymbol{K}\rangle \langle 0| . \tag{2.61}$$

Using the completeness relation $\sum_k |\boldsymbol{k}\rangle \langle \boldsymbol{k}| = 1$ with electron and hole states $|\boldsymbol{k}, -\boldsymbol{k'}\rangle = \hat{c}^\dagger_{c,\boldsymbol{k}} \hat{c}^\dagger_{h,-\boldsymbol{k'}} |0\rangle$, the exciton creation operator can be expressed as

$$\begin{aligned}
\hat{C}^\dagger_{\nu,\boldsymbol{K}} &= \sum_{\boldsymbol{k},\boldsymbol{k'}} |\boldsymbol{k}, -\boldsymbol{k'}\rangle \langle \boldsymbol{k}, -\boldsymbol{k'}| \, |\nu, \boldsymbol{K}\rangle \langle 0| \\
&= \sum_{\boldsymbol{k},\boldsymbol{k'}} \langle \boldsymbol{k}, -\boldsymbol{k'}| \, |\nu, \boldsymbol{K}\rangle \, |\boldsymbol{k}, -\boldsymbol{k'}\rangle \langle 0| \\
&= \sum_{\boldsymbol{k},\boldsymbol{k'}} \langle \boldsymbol{k}, -\boldsymbol{k'}| \, |\nu, \boldsymbol{K}\rangle \, \hat{c}^\dagger_{c,\boldsymbol{k}} \hat{c}^\dagger_{h,-\boldsymbol{k'}},
\end{aligned} \tag{2.62}$$

where the relation $\hat{c}^\dagger_{c,\boldsymbol{k}} \hat{c}^\dagger_{h,-\boldsymbol{k'}} = |\boldsymbol{k}, -\boldsymbol{k'}\rangle \langle 0|$ was used. The term $\langle \boldsymbol{k}, -\boldsymbol{k}| \, |\nu, \boldsymbol{K}\rangle$ can be evaluated as [23]:

$$\begin{aligned}
\langle \boldsymbol{k}, -\boldsymbol{k'}| \, |\nu, \boldsymbol{K}\rangle &= \int \mathrm{d}^3 r \int \mathrm{d}^3 r' \, \langle \boldsymbol{k}, -\boldsymbol{k'} \, | \, \boldsymbol{r}, \boldsymbol{r'}\rangle \langle \boldsymbol{r}, \boldsymbol{r'} \, | \, \nu, \boldsymbol{K}\rangle \\
&= \int \mathrm{d}^3 r \int \mathrm{d}^3 r' e^{-i\boldsymbol{k}\cdot\boldsymbol{r}} e^{-i\boldsymbol{k'}\cdot\boldsymbol{r'}} e^{i\boldsymbol{K}(\boldsymbol{r}+\boldsymbol{r'})/2} \psi_\nu(\boldsymbol{r} - \boldsymbol{r'}) \\
&= \delta\Big[\boldsymbol{K} - (\boldsymbol{k} - \boldsymbol{k'})\Big] \psi_\nu\Big((\boldsymbol{k} + \boldsymbol{k'})/2\Big),
\end{aligned} \tag{2.63}$$

where $\psi_n u(\boldsymbol{k})$ is the Fourier transform of the exciton wave function $\psi_\nu(\boldsymbol{r})$. The exciton creation operator can then be written as [22]:

$$\hat{C}^\dagger_{\nu,\boldsymbol{K}} = \sum_{\boldsymbol{k}} \psi_\nu(\boldsymbol{k}) \hat{c}^\dagger_{c,\frac{1}{2}\boldsymbol{K}+\boldsymbol{k}} \hat{c}^\dagger_{h,\frac{1}{2}\boldsymbol{K}-\boldsymbol{k}}. \tag{2.64}$$

The commutation relation between exciton annihilation and creation operators can then be shown to be [22]:

$$\Big[\hat{C}_{\nu,\boldsymbol{K}}, \hat{C}^\dagger_{\mu,\boldsymbol{K'}}\Big] = \delta_{\nu,\mu}\delta_{\boldsymbol{K},\boldsymbol{K'}} - \sum_{\boldsymbol{k}} |\psi_\nu(\boldsymbol{k})|^2 (n_{c,\boldsymbol{k}} + n_{h,\boldsymbol{k}}). \tag{2.65}$$

Thus, the excitons behave as bosons for sufficiently low densities where $n_{c,\boldsymbol{k}} = n_{h,\boldsymbol{k}} \approx 0$.

The free exciton Hamiltonian can now be written in the form:

$$\hat{\mathrm{H}}_{\mathrm{exc},0} = \sum_{\nu,\boldsymbol{K}} \hbar\omega_{\mathrm{exc},\nu} \hat{C}^\dagger_{\nu,\boldsymbol{K}} \hat{C}_{\nu,\boldsymbol{K}}, \tag{2.66}$$

which, provided $\hbar\omega_{\mathrm{exc},\nu} = \varepsilon_{c,\boldsymbol{K}_{\mathrm{bg}}} + \varepsilon_{h,\boldsymbol{K}_{\mathrm{bg}}} + E_\nu$ where $\boldsymbol{K}_{\mathrm{bg}}$ is the position of the band gap in momentum space, gives approximately the same energy as the unperturbed Hamiltonian, Eq. (2.56).

In order to diagonalize the interaction Hamiltonian, which is the last term in Eq. (2.56), the pair operator $\hat{c}^\dagger_{h,-\boldsymbol{k}} \hat{c}^\dagger_{c,-\boldsymbol{k}}$ must be expressed in terms of exciton operators. To this end, we multiply Eq. (2.64) with $\psi_\nu(\boldsymbol{\kappa})$ from the left, and sum over all quantum numbers ν:

$$\begin{aligned}
\sum_\nu \psi^*_\nu(\boldsymbol{\kappa}) \hat{C}^\dagger_{\nu,\boldsymbol{K}} &= \sum_{\boldsymbol{k}} \underbrace{\Big[\sum_\nu \psi^*_\nu(\boldsymbol{\kappa}) \psi_\nu(\boldsymbol{k})\Big]}_{\delta_{\boldsymbol{k},\boldsymbol{\kappa}}} \hat{c}^\dagger_{c,\frac{1}{2}\boldsymbol{K}+\boldsymbol{k}} \hat{c}^\dagger_{h,\frac{1}{2}\boldsymbol{K}-\boldsymbol{k}} \\
&= \hat{c}^\dagger_{c,\frac{1}{2}\boldsymbol{K}+\boldsymbol{\kappa}} \hat{c}^\dagger_{h,\frac{1}{2}\boldsymbol{K}-\boldsymbol{\kappa}}.
\end{aligned} \tag{2.67}$$

Thus, the pair operator in the interaction Hamiltonian can be identified as

$$\hat{c}^\dagger_{c,\boldsymbol{k}} \hat{c}^\dagger_{h,-\boldsymbol{k}} = \sum_\nu \psi^*_\nu(\boldsymbol{k}) \hat{C}^\dagger_\nu,$$

where $\hat{C}^\dagger_\nu \equiv \hat{C}^\dagger_{\nu,\boldsymbol{q}}\big|_{\boldsymbol{q}=0}$. The interaction Hamiltonian can then be written as

$$\begin{aligned}\hat{\mathrm{H}}_{\text{exc, int}} &\approx \sum_{\boldsymbol{k},\nu} \hbar(g_{\omega_\mathrm{d}}\psi^*_\nu(\boldsymbol{k})\hat{C}^\dagger_\nu + h.c.) \\ &= \sum_{\boldsymbol{k},\nu} \hbar(\tilde{g}_{\boldsymbol{k},\omega_\mathrm{d},\nu}\hat{C}^\dagger_\nu + h.c.),\end{aligned} \tag{2.68}$$

where $\tilde{g}_{\boldsymbol{k},\omega_\mathrm{d},\nu} \equiv g_{\omega_\mathrm{d}}\psi^*_\nu(\boldsymbol{k})$.

The total Hamiltonian of the semiconductor–light system expressed in terms of exciton creation and annihilation operators is then:

$$\hat{\mathrm{H}}_{\text{exc}} = \sum_{\boldsymbol{k},\nu} \hbar\omega_{\text{exc},\nu}\hat{C}^\dagger_{\nu,\boldsymbol{k}}\hat{C}_{\nu,\boldsymbol{k}} + \sum_{\boldsymbol{k},\nu} \hbar(\tilde{g}_{\boldsymbol{k},\omega_\mathrm{d},\nu}\hat{C}^\dagger_\nu + h.c.). \tag{2.69}$$

2.3.2 Transition metal dichalcogenides

Transition metal dichalcogenides (TMDs) is a family of semiconducting and metallic materials which are made up of transition metal and chalcogen atoms. In this thesis, the focus will be restricted to Group-6 TMDs with chemical formula MX_2, $\mathrm{M} \in \{\mathrm{W}, \mathrm{Mo}\}$, $\mathrm{X} \in \{\mathrm{S}, \mathrm{Se}\}$, which are semiconductors with similar electronic band structures, which will be referred to simply as TMDs from this point on. Bulk TMDs are made up of 2D layers with a honeycomb lattice structure where the layers are bound together by weak van der Waals forces, much like graphite. Similar to isolation of graphene from graphite, single layers of TMDs can be extracted from bulk crystals to yield stable 2D materials [3]. A key difference with graphene however, is the absence of a center of inversion in the unit cell of monolayer TMDs, which opens up degenerate direct band gaps at the $\pm K$ points with novel physical properties [24, 25]. The 1st Brillouin zone of TMDs is shown in Fig. 2.4b).

Circular dichroism and valley pseudospin

A qualitative understanding of the optical properties of TMDs can be obtained by inspecting an effective two-band model of the Hamiltonian close to the $\pm K$ points [26]. Using the same coordinate system as in Section 2.2.3 with y as the out-of-plane direction, and ignoring for now spin for simplicity, the Hamiltonian reads

$$\begin{aligned}\hat{\mathrm{H}}_{\pm K} &= at(\pm\hbar k_x\hat{\sigma}_x + \hbar k_z\hat{\sigma}_y) + \hbar\Delta/2\hat{\sigma}_z \\ &= \hbar\begin{pmatrix}\Delta/2 & at(\pm k_x + ik_z) \\ at(\pm k_x - ik_z) & -\Delta/2\end{pmatrix},\end{aligned} \tag{2.70}$$

where k is the wave vector with respect to the $\pm K$ point, the components of $\hat{\boldsymbol{\sigma}}$ are the Pauli matrices, a is the lattice parameter, t is the hopping integral which is related to the electronic transport properties, and $\hbar\Delta = E_\mathrm{g}$ is the band gap energy. The Hamiltonian acts on a spinor of the form

$$|\psi\rangle = \begin{pmatrix}\psi_\mathrm{U} \\ \psi_\mathrm{L}\end{pmatrix}.$$

Unlike valence and conduction bands, the eigenstates ψ_U and ψ_L are coupled by $\boldsymbol{k}$ as evidenced by the $\boldsymbol{k}$ dependence of the off-diagonal elements, meaning the eigenstates generally consist of superpositions of the valence and conduction band. However, at the $\pm K$ points where $k_x = k_z = 0$, the Hamiltonian is diagonalized in $\boldsymbol{k}$, which means the

eigenstate ψ_{U} and ψ_{L} corresponds to the conduction band and valence band, respectively. At the $\pm K$ points, the diagonal and off-diagonal elements describe the energy and coupling respectively, of the valence and conduction band electrons.

Interaction with light can be included by the substitution

$$\hbar \boldsymbol{k} \to \hbar \boldsymbol{k} - e\boldsymbol{A},$$

where $\boldsymbol{A}$ is the vector potential of the light. As $\boldsymbol{A}$ can take complex values, Eq. (2.70) must be adjusted as

$$\hat{\mathrm{H}}_{\pm K} = \begin{pmatrix} \hbar\Delta/2 & at[\pm(\hbar k_x - eA_x) + i(\hbar k_z - e/\hbar A_z)] \\ at[\pm(\hbar k_x - eA_x^*) - i(\hbar k_y - eA_z^*)] & -\hbar\Delta/2 \end{pmatrix}, \tag{2.71}$$

where the superscript * denotes complex conjugation, in order to ensure that the Hamiltonian is Hermitian. For light propagating in the y direction with a right-hand-circular polarization, σ^+ polarized light, there is a $-\pi/2$ phase difference between the x and z components, meaning the components of the vector potential can be written as $A_x = A_0/\sqrt{2}$ and $A_z = -iA_0/\sqrt{2}$. Substituting into Eq. (2.71) with $k_x = k_z = 0$, i. e. at the $\pm K$ points, yields

$$\hat{\mathrm{H}}_K = \begin{pmatrix} \hbar\Delta/2 & -\sqrt{2}A_0 eat \\ -\sqrt{2}A_0 eat & -\hbar\Delta/2 \end{pmatrix}, \tag{2.72}$$

$$\hat{\mathrm{H}}_{-K} = \begin{pmatrix} \hbar\Delta/2 & 0 \\ 0 & -\hbar\Delta/2 \end{pmatrix}. \tag{2.73}$$

This means right-hand-circularly polarized light couples the valence and conduction band for the K points exclusively. This is reversed for left-hand-circularly polarized light, σ^- polarized light, where the bands are coupled exclusively at the $-K$ points. This constitutes an optical selection rule called *circular dichroism*, where the choice of circular polarization corresponds to a choice between the K and $-K$ points in the Brillouin zone, commonly referred to as valleys due to the corresponding minimum in the conduction band.

The choice of valley can be written as a pseudospin, $\tau \in \{-1, 1\}$, where ± 1 corresponds to $\pm K$. The pseudospin τ is commonly referred to as the *valley index*, and constitutes a degree of freedom. The presence of degenerate valleys and optical selection rules makes TMDs promising platforms for research in the field of *valleytronics*, which aims to use the valley degree of freedom to transport, store, and manipulate information. This is similar to the field of *spin*tronics, where the *spin* degree of freedom is used for information processing.

Excitons in TMDs

By shining light at the resonance frequency with the appropriate circular polarization, one can selectively excite excitons in the K or $-K$ valley, making excitons good candidates for information carriers in valleytronics applications. Due to a large spin-orbit splitting, the valence band[5] is split into two sub-bands depending on the spin of the valence electron, such that there are two distinct spin-polarized band gaps in each valley, which are commonly denoted A and B [27], see Fig. 2.5. The spin-orbit coupling, and

[5]The conduction band is also split into sub-bands, though the energy difference is much smaller.

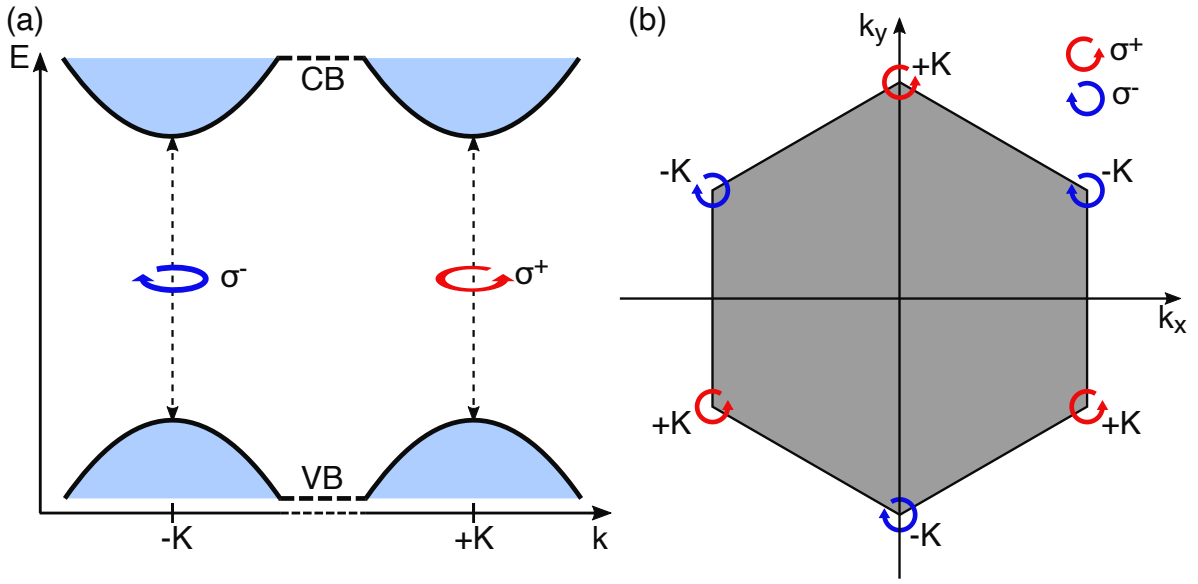

Figure 2.4: a) Illustration of the band gaps in a monolayer TMD, situated in the $\pm K$ valleys, with VB and CB denoting valence band and transduction band, respectively. The valence electrons in the $\pm K$ valley can be selectively addressed by light with circular polarization $\sigma^{\pm}$, meaning the valleys exhibit *circular dichroism*. b) Illustration of the first Brillouin zone, shaded gray, of a transition metal dichalcogenide, with $\pm K$ valleys annotated.

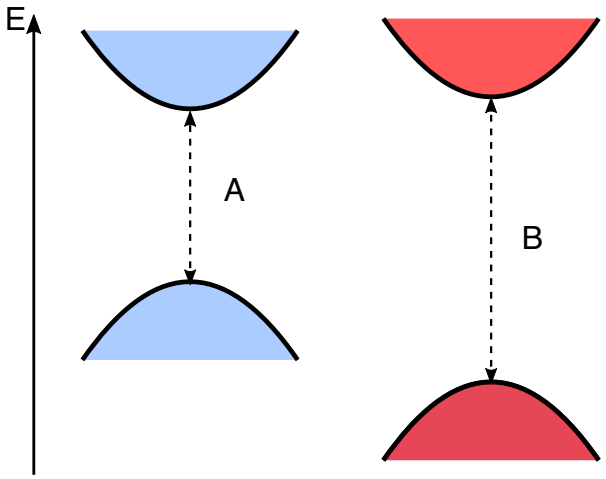

Figure 2.5: Illustration of the spin-orbit splitting of the valence and conduction bands into spin-polarized sub-bands. The red and blue coloring denotes spin-down and spin-up (spin-up and spin-down) polarization of the sub-bands at the K ($-K$) valley respectively.

accordingly spin polarization, is dependent on the valley index, such that the A band gap is entirely spin-up polarized in one valley, and entirely spin-down polarized in the other.

As a side note, though the band gaps at the $\pm K$ points are only direct for monolayers of TMDs [28], similar excitonic resonances have also been experimentally observed in multilayer TMDs [29].

Though TMDs are 2D semiconductors, their excitonic modes are qualitatively different to the ones found in more conventional quasi-2D quantum-well semiconductors. The binding energies of the excitonic modes are substantially greater in TMDs, with typical binding energies around $\sim 300\,\text{meV}$ [30] compared to $\sim 10\,\text{meV}$ for commonly used GaAs quantum-wells [31]. A convenient consequence of the high binding energy is

the presence of robust excitonic resonances at substantially higher temperatures allowing for operation even at room temperature [29]. The high binding energy, combined with a relatively high effective mass [32], leads to an effective Bohr-radius on the order of $\sim 1\,\mathrm{nm}$. This renders the approximation used to obtain the Wannier equation invalid, and consequently, the resonance energies of the excitonic modes in TMDs do not follow a hydrogenic energy spectrum [30, 33]. The excitonic modes are in this case referred to as *tightly-bound* Wannier-Mott excitons[6], which can still be modeled using a Hamiltonian of the form Eq. (2.69)[7].

Magnetic moment of TMDs and valley-Zeeman splitting

As TMDs are 2D materials, the orbital motion of electrons, and the resultant electric currents, are confined in-plane, producing an out-of-plane orbital magnetic moment. Combined with the strong spin-orbit coupling, this results in shift in the Zeeman energy [Eq. (2.10)], and thus a shift in the band gap, in out-of-plane magnetic fields. As the sign of the spin polarization is opposite for the K and $-K$ valleys, the sign of the Zeeman shift will correspond to the valley index, and as such the degeneracy between the valleys will be lifted in strong out-of-plane magnetic fields [35]. This phenomenon is referred to as the *valley-Zeeman effect* in reference to the similar *spin-Zeeman effect*, which lifts the degeneracy of electronic orbitals with opposite spin in magnetic fields.

The valley-Zeeman effect on the resonance energy of excitonic modes can be modelled quantum mechanically in a similar manner as the Zeeman energy, by including a contribtuion to the Hamiltonian of the form

$$\hat{\mathrm{H}}_{\text{v-Z}} = \sum_{\nu} \tau g_{\nu} B_y \hat{C}_{\nu}^{\dagger} \hat{C}_{\nu}, \tag{2.74}$$

where ν is the quantum number of the excitonic mode, τ is the valley index, B_y is the out-of-plane magnetic flux density, and g_ν is the related coupling strength for the given excitonic mode.

Van der Waals heterostructures and proximity-enhanced valley-Zeeman effect

By isolating layers of 2D materials and piling them on a substrate to form a stack of one or more layers, we can create artificial structures known as *van der Waals heterostructures* with a form similar to layered van der Waals materials such as bulk TMDs [3]. Exchange interactions in the interfaces between the materials may then result in drastically different properties, such as one material adopting a property of the other. As exchange interactions are very short-ranged, the resultant effects, aptly named *proximity effects*, will only apply to the first few successive layers [36].

The *magnetic proximity effect* is an example of such an effect, obtained by piling the layer onto a magnetic substrate. The magnetic proximity effect in TMDs leads to a substantially enhanced valley-Zeeman splitting dependent on the out-of-plane magnetization of the substrate rather than a magnetic field [12, 37]; we will call this effect the *proximity-enhanced valley-Zeeman effect*. Exchanging magnetic flux density for magnetization, this can be modeled as a contribution to the Hamiltonian of the form [Eq. (2.74)]

$$\hat{\mathrm{H}}_{\text{p-v-Z}} = \sum_{\nu} \tau g_{\nu,p} \hat{m}_y \hat{C}_{\nu}^{\dagger} \hat{C}_{\nu}, \tag{2.75}$$

[6] Not to be confused with Frenkel excitons which are made up of electrons and holes at the same site, and are commonly referred to as *tightly-bound excitons*.

[7] As is done in the literature, see for instance Ref. [34]

where $\hat{m}_z$ is the operator for the out-of-plane magnetization in the substrate. This effect may be used to couple the excitonic modes to magnonic modes by way of a dynamically induced shift in the exciton resonance frequency due to a magnon-induced oscillating out-of-plane magnetization.

2.4 Open quantum systems

The purpose of this thesis is to characterize the coupling between an excitonic and a magnonic system. It is not uncommon for a system to be described quantum-mechanically in an isolated form, where the connection to an environment outside of the system is neglected. Indeed, both excitons and magnons can be described in such a manner, yielding Hamiltonians in the familiar form of harmonic oscillators. However, just as the excitonic and magnonic systems may couple to each other, they will also couple to the environment, and as such, it is natural to treat the magnon–exciton system as coupled *open quantum systems*, connected to each other and the environment.

The quantum theory for such systems, commonly referred to as *open quantum systems*, can be split into two main approaches: the master equation approach, and input–output theory. The master equation yields insight as to how the system evolves when connected to the environment. This is achieved by a procedure where the environmental degrees of freedom are traced out, yielding a *coarse-grained time-evolution* of the reduced density matrix of the system [21]. Input–output theory on the other hand, focuses instead on how the environment is affected by the system, providing a relation between an input field in the environment, the state of the environment *before* an interaction with the system, and the corresponding output field, the state of the environment *after* the interaction, see Fig. 2.6.

In this thesis, input–output theory will be used to characterize the dependency of an environmental output field on the internal magnon–exciton coupling strength in a coupled magnon–exciton system. The coupling strength may then be determined experimentally by measurement and analysis of the environmental output fields.

The first section will present the basic principles of input-output theory, which will be used to derive a relation between the outgoing and incoming modes of a field in the environment when it is allowed to interact with a quantum system as a heat bath. In the next section, this approach will be extended to include the effects of external driving of the system, in the form of a coherent state of the bath modes. This will be used in the last section to find an expression for the optical output-signal from a magnon–exciton system that is driven doubly with classical microwave-domain and optical radiation.

2.4.1 Quantum Langevin equation and input–output theory

The coupling between a quantum mechanical system and the environment, in this context referred to as a heat bath, provides the system with a channel by which excited states can decay in a dissipative process. As such, the coupling to the heat bath may effectively be described as a form of damping. Unfortunately, describing a damped system quantum-mechanically is not possible with the canonical-quantization approach as that would require the system to be conservative. As an alternative approach, one can construct a total Hamiltonian for the coupled system and environment from the Hamiltonians of the undamped system, the environment, and the interaction between them. The total Hamiltonian can then be used to obtain the combined dynamics of the system and the environment. This section will follow the steps laid out in Ref. [13] to derive an equation of motion known as the *quantum Langevin equation* using the input–output theory procedure. The derivation is done in the Heisenberg picture. where the operators themselves are time-dependent. The time-dependence of operators will generally be suppressed, i.e writing $\hat{\mathcal{O}}(t)$ as $\hat{\mathcal{O}}$, but will be written out explicitly in some cases, such as when time is an integration parameter.

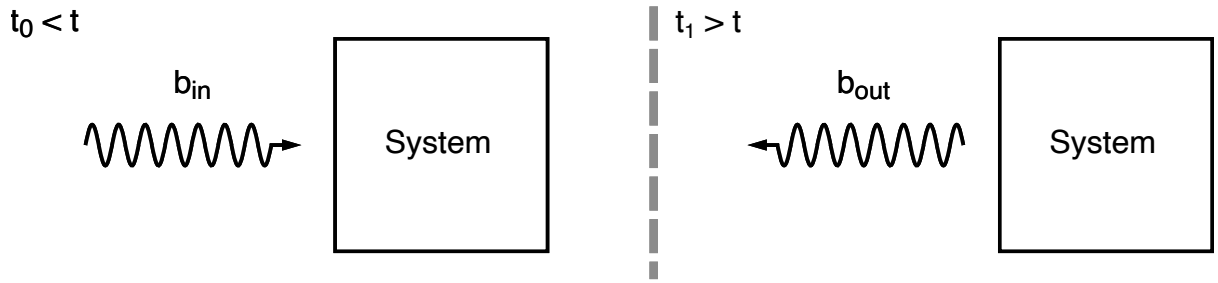

Figure 2.6: Illustration of the input field at time t_0, defined in Eq. (2.121), and output field at time t_1, defined in Eq. (2.92) in relation to the system.

The total Hamiltonian of the system coupled to the environment can be written as

$$\hat{\mathrm{H}} = \hat{\mathrm{H}}_{\mathrm{S}} + \hat{\mathrm{H}}_{\mathrm{b}} + \hat{\mathrm{H}}_{\mathrm{int}}, \tag{2.76}$$

where $\hat{\mathrm{H}}_{\mathrm{S}}$ is the Hamiltonian of the isolated system, $\hat{\mathrm{H}}_{\mathrm{b}}$ is the Hamiltonian of the heat bath, and $\hat{\mathrm{H}}_{\mathrm{int}}$ is the Hamiltonian of the system-bath interaction.

The Hamiltonian of the heat bath will be written in the form:

$$\hat{\mathrm{H}}_{\mathrm{b}} = \hbar \int_{-\infty}^{\infty} \frac{\mathrm{d}\omega}{2\pi} \omega \hat{b}^{\dagger}(\omega)\hat{b}(\omega), \tag{2.77}$$

where the operators $\hat{b}(\omega)$ and $\hat{b}^{\dagger}(\omega)$ are bosonic annihilation and creation operators which satisfy the commutation relation:

$$\left[\hat{b}(\omega), \hat{b}^{\dagger}(\omega')\right] = 2\pi\delta(\omega - \omega'). \tag{2.78}$$

The expression for the heat bath corresponds to the Hamiltonian of a continuum of independent harmonic oscillators. For the case where the system is coupled to a radiative heat bath, such that it dissipates radiatively, the integral form of the heat bath Hamiltonian can be obtained from the Hamiltonian of quantized photonic modes [21]:

$$\hat{\mathrm{H}}_{\mathrm{photon}} = \sum_{k} \hbar\omega_k (\hat{b}_k^{\dagger}\hat{b}_k + \frac{1}{2}), \tag{2.79}$$

where the operator $\hat{b}_{\boldsymbol{k}}^{\dagger}$ ($\hat{b}_{\boldsymbol{k}}$) creates (annihilates) a photon with quantum number k, usually taken to be the wave number. By neglecting the constant vacuum contribution $1/2$ and taking the continuum limit, Eq. (2.77) is recovered. Physically, this corresponds to taking the limit $V_c \to \infty$ for the quantization volume, which is also known as the thermodynamic limit. Though the physical limit of a frequency is zero, and one might then expect the lower limit of an integration over frequency to be zero, this is not the case in a frame rotating at frequency Ω, where the range will shift to $(-\Omega, \infty)$. In optical experiments such as the one detailed in this thesis, characteristic frequencies of the system are high enough that the lower limit can be approximated as $-\Omega \to -\infty$ [13].

The interaction between the system and the heat bath is assumed to be linear[8] in one of the system operators $\hat{c}$. This allows the interaction Hamiltonian to be written in the form:

$$\hat{\mathrm{H}}_{\mathrm{int}} = i\hbar \int_{-\infty}^{\infty} \frac{\mathrm{d}\omega}{2\pi} \kappa(\omega) \left[\hat{b}^{\dagger}(\omega)\hat{c} - \hat{c}^{\dagger}\hat{b}(\omega)\right], \tag{2.80}$$

[8]Though this assumption does not give the most general form of a coupling, it is practically ubiquitous in quantum optics [13].

where $\kappa(\omega)$ is the coupling strength between the system and the heat bath mode at frequency ω. Generally, a linear coupling would also allow for coupling terms of the form $\hat{c}^\dagger\hat{b}^\dagger$ or $\hat{b}\hat{c}$, but such terms are neglected in the rotating wave approximation.

The dynamics of the coupled system and environment can be characterized by the equations of motion of the constituent operators, which are governed by the Heisenberg equation, Eq. (2.2). Using this relation, the equations of motion of the bath operator $\hat{b}(\omega)$ and system operator $\hat{c}$ are written as:

$$\dot{\hat{b}}(\omega) = -i\omega\hat{b}(\omega) + \kappa(\omega)\hat{c} \tag{2.81}$$

$$\dot{\hat{c}} = \frac{i}{\hbar}\big[\hat{\mathrm{H}}_\mathrm{S}, \hat{c}\big] - \int_{-\infty}^{\infty}\frac{\mathrm{d}\omega}{2\pi}\kappa(\omega)\hat{b}(\omega). \tag{2.82}$$

Eq. (2.81) can be solved by referring to the initial conditions, at a time $t_0 < t$:

$$\hat{b}(\omega) = e^{-i\omega(t-t_0)}\hat{b}_0(\omega) + \kappa(\omega)\int_{t_0}^{t}\mathrm{d}t' e^{-i\omega(t-t')}\hat{c}(t'), \tag{2.83}$$

where $\hat{b}_0(\omega) \equiv \hat{b}(\omega)|_{t=t_0}$ is the annihilation operator of the bath mode at frequency ω at an initial time $t_0 < t$, which satisfies the same commutation relation as $\hat{b}$. Substituting into the equation of motion of the system operator $\hat{c}$ yields [Eq (2.82)]:

$$\begin{aligned}\dot{\hat{c}} = \frac{i}{\hbar}\big[\hat{\mathrm{H}}_\mathrm{S}, \hat{c}\big] &- \int_{-\infty}^{\infty}\frac{\mathrm{d}\omega}{2\pi}\kappa(\omega)e^{-i\omega(t-t_0)}\hat{b}_0(\omega) \\ &- \int_{-\infty}^{\infty}\frac{\mathrm{d}\omega}{2\pi}\big[\kappa(\omega)\big]^2\int_{t_0}^{t}\mathrm{d}t' e^{-i\omega(t-t')}\hat{c}(t').\end{aligned} \tag{2.84}$$

In order to proceed we employ the *first Markov approximation*, in which the coupling constant is assumed to be independent of frequency, such that it can be written as

$$\kappa(\omega) = \sqrt{\gamma_\mathrm{b}}, \tag{2.85}$$

where γ_b can be shown to be the spontaneous rate of dissipation to the thermal bath, given by Fermi's golden rule [38]. The now-constant coupling strength can then be taken outside the integral, and the order of the integrals in the second term of Eq. (2.84) can be exchanged.

By using the relations [13]:

$$\int_{-\infty}^{\infty}\frac{\mathrm{d}\omega}{2\pi}e^{-i\omega(t-t')} = \delta(t-t'), \tag{2.86}$$

$$\int_{t_0}^{t}\mathrm{d}t' f(t')\delta(t-t') = \frac{1}{2}f(t), \tag{2.87}$$

and defining the *input field*, $\hat{b}_\mathrm{in}$ as

$$\hat{b}_\mathrm{in} \equiv \int_{-\infty}^{\infty}\frac{\mathrm{d}\omega}{2\pi}e^{-i\omega(t-t_0)}b_0(\omega), \tag{2.88}$$

Eq. (2.84) becomes:

$$\dot{\hat{c}} = \frac{i}{\hbar}\big[\hat{\mathrm{H}}_\mathrm{S}, \hat{c}\big] - \frac{\gamma_\mathrm{b}}{2}\hat{c} - \sqrt{\gamma_\mathrm{b}}\hat{b}_\mathrm{in}. \tag{2.89}$$

This equation is known as the *quantum Langevin equation*, and is also commonly referred to as the *Heisenberg-Langevin equation*. For the simple case where the system is a harmonic oscillator, with the system Hamiltonian $\hat{\mathrm{H}}_{\mathrm{S}} = \hbar\omega_0\hat{c}^\dagger\hat{c}$, Eq. (2.89) reduces to

$$\dot{\hat{c}} = -i\omega_0\hat{c} - \frac{\gamma_{\mathrm{b}}}{2}\hat{c} - \sqrt{\gamma_{\mathrm{b}}}\hat{b}_{\mathrm{in}}. \tag{2.90}$$

The equation of motion of the system variable $\hat{c}$ has been found by referring to the initial conditions of the bath modes, $\hat{b}_{\mathrm{in}}$. However, it is also possible to obtain an equation of motion by instead referring to the *final* conditions of the bath modes, at a time $t_1 > t$, writing the solution to Eq. (2.81) as

$$\hat{b}(\omega) = e^{-i\omega(t-t_1)}\hat{b}_1(\omega) - \sqrt{\gamma_{\mathrm{b}}}\int_t^{t_1} \mathrm{d}t' e^{-i\omega(t-t')}\hat{c}(t'), \tag{2.91}$$

where $\hat{b}_1(\omega) \equiv \hat{b}(\omega)|_{t=t_1}$ is the annihilation operator of the bath mode at frequency ω at a final time $t_1 > t$, satisfying the same commutation relation as $\hat{b}$. Defining the *output field* $\hat{b}_{\mathrm{out}}$ as

$$\hat{b}_{\mathrm{out}} = \int_{-\infty}^{\infty} \frac{\mathrm{d}\omega}{2\pi} e^{-i\omega(t-t_1)} b_1(\omega), \tag{2.92}$$

and following the same procedure as for the quantum Langevin equation, we arrive at the *time-reversed* quantum Langevin equation [13]:

$$\dot{\hat{c}} = \frac{i}{\hbar}\big[\hat{\mathrm{H}}_{\mathrm{S}}, \hat{c}\big] + \frac{\gamma_{\mathrm{b}}}{2}\hat{c} - \sqrt{\gamma_{\mathrm{b}}}\hat{b}_{\mathrm{out}}. \tag{2.93}$$

For the case of a harmonic oscillator, this expression reduces to

$$\dot{\hat{c}} = -i\omega_0\hat{c} + \frac{\gamma_{\mathrm{b}}}{2}\hat{c} - \sqrt{\gamma_{\mathrm{b}}}\hat{b}_{\mathrm{out}}. \tag{2.94}$$

Subtracting Eq. (2.94) from Eq. (2.90) yields the *input–output relation*:

$$\hat{b}_{\mathrm{out}}(t) - \hat{b}_{\mathrm{in}}(t) = \sqrt{\gamma_{\mathrm{b}}}\hat{c}(t). \tag{2.95}$$

The procedure of obtaining an input–output relation from the quantum Langevin and time-reversed quantum Langevin equations is referred to as *input–output theory*. The output field can now be determined by solving the quantum Langevin equation and substituting into the input–output relation, with the input field specified as an initial condition.

In general, the system may be coupled to the environment through more than one dissipative processes. Additional processes can be taken into account by adding corresponding bath and interaction Hamiltonians to Eq. (2.76), and following the same procedure as for the single heat bath case to obtain additional terms in the quantum Langevin equation as well as an additional input–output relation

$$\dot{\hat{c}} = -i\omega_0\hat{c} - \frac{\gamma_{\mathrm{b}}}{2}\hat{c} - \frac{\gamma_{\mathrm{e}}}{2}\hat{c} - \sqrt{\gamma_{\mathrm{b}}}\hat{b}_{\mathrm{in}} - \sqrt{\gamma_{\mathrm{e}}}\hat{e}_{\mathrm{in}}, \tag{2.96}$$

$$\hat{e}_{\mathrm{out}}(t) - \hat{e}_{\mathrm{in}}(t) = \sqrt{\gamma_{\mathrm{e}}}\hat{c}(t), \tag{2.97}$$

where γ_{e}, $\hat{e}_{\mathrm{in}}$, and $\hat{e}_{\mathrm{out}}$ is the coupling rate, input-, and output field respectively of the external heat bath or heat baths. As we might not control these other bath modes, and as

such might not be able to specify their input or output modes, the added damping stemming from the other heat baths may be approximated by writing the quantum Langevin equation as

$$\dot{\hat{c}} = -i\omega_0\hat{c} - \frac{\gamma_\mathrm{T}}{2}\hat{c} - \sqrt{\gamma_\mathrm{b}}\hat{b}_\mathrm{in}, \tag{2.98}$$

where $\frac{\gamma_\mathrm{T}}{2} \equiv \frac{\gamma_\mathrm{b}+\gamma_\mathrm{e}}{2}$ is the *total* damping rate of the harmonic oscillator, and where the input field of the external heat bath has been neglected.

2.4.2 Input–output theory for driven harmonic oscillators

The relation Eq. (2.95) between the input and output fields was derived for a system with a simple harmonic oscillator Hamiltonian. Certain systems have multiple harmonic oscillator modes, as is the case for both the magnonic and excitonic systems. By applying monochromatic radiation in a coherent state to selectively drive a specific mode, such systems can effectively be considered as simple harmonic oscillator systems. The added coherent-state radiation, which can be described classically using numbers rather than operators, can be treated in two ways. The first option is to treat the drive as part of the input field, such that the input field contains both a classical part and a quantum mechanical part, using the previously derived input-output theory. However, the classical radiation will excite a population in the system, which may lead to interactions. In our case, where a microwave drive induces a magnon population that interacts with the excitonic modes, it is practical to treat the added excitations explicitly, as part of the system. This is the second option, which will be the focus of this section. The procedure presented is based on a similar procedure in Refs. [39, 40].

The classical drive adds a field in the heat bath that can be represented with numbers rather than operators, and as such, the bath modes are split into a classical part and a quantum part

$$\hat{b}(\omega) \to \hat{b}(\omega) + 2\pi l_\mathrm{d} e^{-i\omega_\mathrm{d}t}\delta(\omega-\omega_\mathrm{d}), \tag{2.99}$$

$$\hat{b}^\dagger(\omega) \to \hat{b}^\dagger(\omega) + 2\pi l_\mathrm{d} e^{i\omega_\mathrm{d}t}\delta(\omega-\omega_\mathrm{d}), \tag{2.100}$$

where ω_d is the frequency of the driving radiation and l_d is the photon flux of the drive given by the relation $l_\mathrm{d} = \sqrt{P_\mathrm{d}/(\hbar\omega_\mathrm{d})}$ where P_d is the power of the drive. This results in the addition of the term

$$\hat{\mathrm{H}}_\mathrm{d} = i\hbar\sqrt{\gamma_\mathrm{b}}l_\mathrm{d}\left(\hat{c}^\dagger e^{-i\omega_\mathrm{d}t} - \hat{c}e^{i\omega_\mathrm{d}t}\right), \tag{2.101}$$

to the Hamiltonian Eq. (2.76). The total Hamiltonian of the driven harmonic oscillator coupled to a heat bath then reads

$$\begin{aligned}\hat{\mathrm{H}} = {} & \underbrace{\hbar\omega_0\hat{c}^\dagger\hat{c}}_{\hat{\mathrm{H}}_\mathrm{S}} + \underbrace{i\hbar\sqrt{\gamma_\mathrm{b}}l_\mathrm{d}\hat{c}^\dagger e^{-i\omega_\mathrm{d}t} - i\hbar\sqrt{\gamma_\mathrm{b}}l_\mathrm{d}\hat{c}e^{i\omega_\mathrm{d}t}}_{\hat{\mathrm{H}}_\mathrm{d}} + \underbrace{\hbar\int_{-\infty}^{\infty}\frac{\mathrm{d}\omega}{2\pi}\omega\hat{b}^\dagger(\omega)\hat{b}(\omega)}_{\hat{\mathrm{H}}_\mathrm{b}} \\ & + \underbrace{i\hbar\int_{-\infty}^{\infty}\frac{\mathrm{d}\omega}{2\pi}\sqrt{\gamma_\mathrm{b}}\left[\hat{b}^\dagger(\omega)\hat{c} - \hat{c}^\dagger\hat{b}(\omega)\right]}_{\hat{\mathrm{H}}_\mathrm{int}}\end{aligned} \tag{2.102}$$

In order to obtain a Hamiltonian in a similar form as in the previous section, the driving term will have to be dealt with. To this end, a unitary transformation is applied

to the Hamiltonian using the displacement operator [40]:

$$\hat{D}(\alpha) = e^{\alpha\hat{c}^\dagger - \alpha^*\hat{c}}, \tag{2.103}$$

transforming the Hamiltonian as [40]:

$$\hat{\tilde{\mathrm{H}}} = \hat{D}^\dagger(\alpha)\hat{\mathrm{H}}\hat{D}(\alpha) - i\hbar\hat{D}^\dagger(\alpha)\dot{\hat{D}}(\alpha) \tag{2.104}$$

$$\begin{aligned} &= \hbar\omega_0(\hat{c}^\dagger + \alpha^*)(\hat{c} + \alpha) + i\hbar\sqrt{\gamma_\mathrm{b}}l_\mathrm{d}(\hat{c}^\dagger + \alpha^*)e^{-i\omega_\mathrm{d}t} - i\hbar\sqrt{\gamma_\mathrm{b}}l_\mathrm{d}(\hat{c} + \alpha)e^{i\omega_\mathrm{d}t} \\ &\quad + i\hbar\int_{-\infty}^{\infty}\frac{\mathrm{d}\omega}{2\pi}\sqrt{\gamma_\mathrm{b}}\Big[\hat{b}^\dagger(\omega)(\hat{c} + \alpha) - (\hat{c}^\dagger + \alpha^*)\hat{b}(\omega)\Big] + \hat{\mathrm{H}}_\mathrm{b} + i\hbar(\dot{\alpha}^*\hat{c} - \dot{\alpha}\hat{c}^\dagger). \end{aligned} \tag{2.105}$$

The displaced Hamiltonian can be written as

$$\hat{\tilde{\mathrm{H}}} = \hbar\omega_0\hat{c}^\dagger\hat{c} + i\hbar\int_{-\infty}^{\infty}\frac{\mathrm{d}\omega}{2\pi}\sqrt{\gamma_\mathrm{b}}\Big[\hat{b}^\dagger(\omega)(\hat{c} + \alpha) - (\hat{c}^\dagger + \alpha^*)\hat{b}(\omega)\Big] + \hat{\mathrm{H}}_\mathrm{b}, \tag{2.106}$$

by neglecting all non-operator valued terms in Eq. (2.105), and setting

$$\dot{\alpha} = -i\omega_0\alpha + \sqrt{\gamma_\mathrm{b}}l_\mathrm{d}e^{-i\omega_\mathrm{d}t}. \tag{2.107}$$

The first term of Eq. (2.105) adds the constant term $\hbar\omega_0|\alpha|^2$ to the Hamiltonian, which is promptly neglected. From this one can surmise that the displacement transformation changes the driving term into a displacement of the annihilation and creation operators, where the square of the displacement corresponds to a number of excitations $n_a = |\alpha|^2$ added to the system. For the purposes of solving for α, the additional damping term $-(\gamma_\mathrm{T}/2)\alpha$ is added to the equation of motion Eq. (2.107). This ensures that the number of added excitation does not grow infinitely in the case where the system is driven on resonance, $\omega_\mathrm{d} = \omega_0$. The equation of motion for α now reads

$$\dot{\alpha} = -i\omega_0\alpha - \frac{\gamma_\mathrm{T}}{2}\alpha + \sqrt{\gamma_\mathrm{b}}l_\mathrm{d}e^{-i\omega_\mathrm{d}t}, \tag{2.108}$$

where $\gamma_\mathrm{T} \equiv \gamma_\mathrm{b} + \gamma_\mathrm{e}$ is the total dissipation rate of the system, with γ_e the dissipation rate to other heat baths, which in this case corresponds to the nonradiative dissipation rate. Writing α as

$$\alpha(t) = \tilde{\alpha}e^{-i\omega_\mathrm{d}t}, \tag{2.109}$$

and substituting this expression into Eq. (2.108), the solution for $\tilde{\alpha}$ can be identified as

$$\tilde{\alpha} = \frac{\sqrt{\gamma_\mathrm{b}}}{i(\omega_0 - \omega_d) - \frac{\gamma_\mathrm{T}}{2}}\sqrt{\frac{P_d}{\hbar\omega_d}}. \tag{2.110}$$

The solution for α may then be identified as [Eq. (2.109)]

$$\alpha = \frac{\sqrt{\gamma_\mathrm{b}}}{i(\omega_0 - \omega_d) - \frac{\gamma_\mathrm{T}}{2}}\sqrt{\frac{P_d}{\hbar\omega_d}}e^{-i\omega_d t}. \tag{2.111}$$

Substituting Eq. (2.111) into the expression for the displaced Hamiltonian yields [Eq. (2.106)]:

$$\begin{aligned} \hat{\tilde{\mathrm{H}}} &= \hbar\omega_0\hat{c}^\dagger\hat{c} \\ &\quad + i\hbar\int_{-\infty}^{\infty}\frac{\mathrm{d}\omega}{2\pi}\sqrt{\gamma_\mathrm{b}}\Big[\hat{b}^\dagger(\omega)e^{-i\omega_d t}(\hat{c}e^{i\omega_d t} + \tilde{\alpha}) - (\hat{c}^\dagger e^{-i\omega_d t} + \tilde{\alpha}^*)\hat{b}(\omega)e^{i\omega_d t}\Big] \\ &\quad + \hat{\mathrm{H}}_\mathrm{b}. \end{aligned} \tag{2.112}$$

Proceeding, a set of unitary transformations will be applied in order to express the Hamiltonian in a more convenient form. These transformations are characterized by unitary operators of the form

$$\hat{U} = e^{-i\beta t\hat{x}^\dagger\hat{x}}, \tag{2.113}$$

where $\hat{x}$ is an annihilation operator. As with the displacement transformation, the transformed Hamiltonian can be found by the relation:

$$\hat{\mathrm{H}}_{\text{transformed}} = \hat{U}^\dagger\hat{\mathrm{H}}\hat{U} - i\hat{U}^\dagger\dot{\hat{U}}. \tag{2.114}$$

This transformation can be done term by term, where all terms that commute with $\hat{x}^\dagger\hat{x}$ can be neglected, leaving terms proportional to $\hat{x}$ or its Hermitian conjugate. The transformation of the operator $\hat{x}$ can be expressed as

$$\hat{x}_{\text{transformed}} = \hat{U}^\dagger\hat{x}\hat{U}, \tag{2.115}$$

where the final term in Eq. (2.114), here equal to

$$-i\hat{U}^\dagger\dot{\hat{U}} = -\beta\hat{x}^\dagger\hat{x} \tag{2.116}$$

is added to the sum of all transformed terms of the Hamiltonian. A simple way of evaluating Eq. (2.115) is to take the partial time derivative of both sides, yielding:

$$\begin{aligned}
\frac{\partial}{\partial t}\hat{x}_{\text{transformed}} &= \frac{\partial\hat{U}^\dagger}{\partial t}\hat{x}\hat{U} + \hat{U}^\dagger\hat{x}\frac{\partial\hat{U}}{\partial t} \\
&= i\beta\hat{x}^\dagger\hat{x}\hat{U}^\dagger\hat{x}\hat{U} - i\beta\hat{U}^\dagger\hat{x}\hat{U}\hat{x}^\dagger\hat{x} \\
&= -i\beta\Big[\hat{U}^\dagger\hat{x}\hat{U}, \hat{x}^\dagger\hat{x}\Big] \\
&= -i\beta\hat{U}^\dagger[\hat{x}, \hat{x}^\dagger\hat{x}]\hat{U} \\
&= -i\beta\hat{U}^\dagger\hat{x}\hat{U} \\
&= -i\beta\hat{x}_{\text{transformed}}
\end{aligned} \tag{2.117}$$

the solution to this equation can be written as

$$\begin{aligned}
\hat{x}_{\text{transformed}} &= \hat{x}_{\text{transformed}}\big|_{t=0}e^{-i\beta t} \\
&= \hat{x}e^{-i\beta t},
\end{aligned} \tag{2.118}$$

where Eq. (2.115) was used to evaluate $\hat{x}_{\text{transformed}}|_{t=0}$.

By applying the unitary transformation $\hat{U}_1 = e^{-i\omega_d t\hat{c}^\dagger\hat{c}}$ and subsequently $\hat{U}_2 = e^{-i\omega_d t\int \mathrm{d}\omega'\hat{b}^\dagger(\omega')\hat{b}(\omega')}$, all exponentials in the integral in Eq. (2.112) can be removed. The full effective Hamiltonian can then be written as

$$\begin{aligned}
\hat{\mathrm{H}}_{\text{eff}} = \hbar\underbrace{(\omega_0 - \omega_d)}_{\Delta\omega_0}\hat{c}^\dagger\hat{c} + i\hbar\int_{-\infty}^{\infty}\frac{\mathrm{d}\omega}{2\pi}\sqrt{\gamma_\mathrm{b}}\Big[\hat{b}^\dagger(\omega)(\hat{c}+\tilde{\alpha}) - (\hat{c}^\dagger+\tilde{\alpha}^*)\hat{b}(\omega)\Big] \\
+ \hbar\int_{-\infty}^{\infty}\frac{\mathrm{d}\omega}{2\pi}\underbrace{(\omega - \omega_d)}_{\Delta\omega}\hat{b}^\dagger(\omega)\hat{b}(\omega).
\end{aligned} \tag{2.119}$$

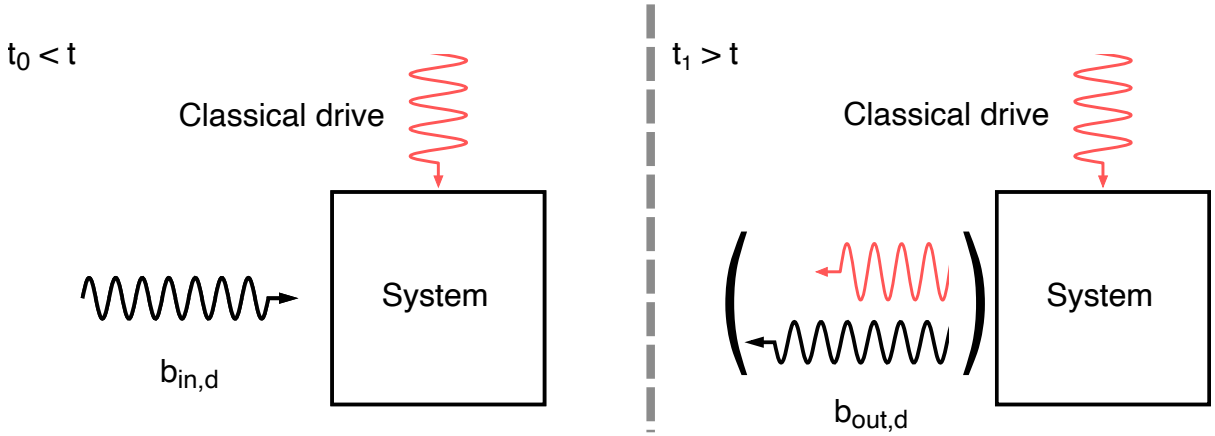

Figure 2.7: Illustration of the detuned input and output fields interacting with a classically driven system. The output field contains a contribution from the classical drive, here colored red, which corresponds to the term proportional to $\tilde{\alpha}$ in Eq. (2.123).

Following the same procedure as for the harmonic oscillator in the absence of driving, the quantum Langevin equation for a driven harmonic oscillator can be written as

$$\dot{\hat{c}} = -i\Delta\omega_0\hat{c} - \frac{\gamma_\mathrm{b}}{2}(\hat{c} + \tilde{\alpha}) - \sqrt{\gamma_\mathrm{b}}\hat{b}_{\mathrm{in},d}, \tag{2.120}$$

where the *detuned* input field $\hat{b}_{\mathrm{in},d}$ has been defined as

$$\hat{b}_{\mathrm{in},d} \equiv \int_{-\infty}^{\infty} e^{i\Delta\omega(t-t_0)} b_0(\omega). \tag{2.121}$$

The effect of the driving on the quantum Langevin equations can thus be summarized as the set of transformations:

$$\begin{aligned} \omega_0 &\to (\omega_0 - \omega_d), \\ \frac{\gamma_\mathrm{b}}{2}\hat{c} &\to \frac{\gamma_\mathrm{b}}{2}(\hat{c} + \tilde{\alpha}), \\ \int_{-\infty}^{\infty} \frac{\mathrm{d}\omega}{2\pi} e^{i\omega(t-t_0)} &\to \int_{-\infty}^{\infty} \frac{\mathrm{d}\omega}{2\pi} e^{i\Delta\omega(t-t_0)}, \\ \int_{-\infty}^{\infty} \frac{\mathrm{d}\omega}{2\pi} e^{i\omega(t-t_1)} &\to \int_{-\infty}^{\infty} \frac{\mathrm{d}\omega}{2\pi} e^{i\Delta\omega(t-t_1)}. \end{aligned} \tag{2.122}$$

Applying these transformation to the input–output relation in the absence of driving, Eq. (2.95), yields the input–output relation for the driven harmonic oscillator:

$$\hat{b}_{\mathrm{out},d}(t) - \hat{b}_{\mathrm{in},d}(t) = \sqrt{\gamma_\mathrm{b}}\Big(\hat{c}(t) + \tilde{\alpha}\Big). \tag{2.123}$$

A sketch of the input and output fields for a classically driven system is shown in Fig. 2.7

2.4.3 Coupling excitons in a transition metal dichalcogenide to magnons

The valley-Zeeman splitting induced by a static out-of-plane magnetic field has been experimentally demonstrated for several different species of TMD [36, 41]. However, we propose that the proximity-induced valley-Zeeman splitting may be used to facilitate a

coupling between magnons and excitons in the TMD by way of the oscillating out-of-plane magnetization induced by magnons in an in-plane magnetized magnetic substrate. In this section we will derive the Hamiltonian and quantum Langevin equations for a system consisting of driven magnons in the uniform-precession magnetostatic mode of an in-plane magnetized thin film magnetic substrate, as discussed in Section 2.2.3, coupled to a driven exciton in a thin layer of TMD piled onto the substrate.

Supposing excitons in the K valley of the TMD are selectively driven close to resonance by coherent optical light with polarization σ^+ and frequency $\omega_{\mathrm{d,op}}$, and magnons in the uniform-precession mode in the magnetic substrate are selectively driven by coherent microwave radiation at the resonance with frequency $\omega_{\mathrm{d,mw}} = \omega_{\mathrm{mag}}$, and neglecting all other excitonic and magnonic modes, the total Hamiltonian of the system may be written as [Section 2.4.2, Eqs. (2.54) and (2.69)]:

$$\begin{aligned}\hat{\mathrm{H}}_{\text{exc-mag}} = \hbar\omega_{\mathrm{exc}}\hat{C}^\dagger\hat{C} + \hbar\omega_{\mathrm{mag}}\hat{a}^\dagger\hat{a} + \underbrace{\hbar g_{\text{mag-exc}}\hat{m}_y\hat{C}^\dagger\hat{C}}_{\hat{\mathrm{H}}_{\text{int,exc-mag}}} \\ + \hbar\int_{-\infty}^{\infty}\frac{\mathrm{d}\omega}{2\pi}\omega\hat{b}^\dagger_{\mathrm{op}}(\omega)\hat{b}_{\mathrm{op}}(\omega) + \hbar\int_{-\infty}^{\infty}\frac{\mathrm{d}\omega}{2\pi}\omega\hat{b}^\dagger_{\mathrm{mw}}(\omega)\hat{b}_{\mathrm{mw}}(\omega) \\ + i\hbar\sqrt{\gamma_{\mathrm{op}}}\int_{-\infty}^{\infty}\frac{\mathrm{d}\omega}{2\pi}\left[\hat{b}^\dagger_{\mathrm{op}}(\omega)\hat{C} - \hat{C}^\dagger\hat{b}_{\mathrm{op}}(\omega)\right] + i\hbar\sqrt{\gamma_{\mathrm{mw}}}\int_{-\infty}^{\infty}\frac{\mathrm{d}\omega}{2\pi}\left[\hat{b}^\dagger_{\mathrm{mw}}(\omega)\hat{a} - \hat{a}^\dagger\hat{b}_{\mathrm{mw}}(\omega)\right] \\ + l_{\mathrm{d,op}}\hat{C}^\dagger e^{-i\omega_{\mathrm{d,op}}t} + l_{\mathrm{d,op}}\hat{C}e^{i\omega_{\mathrm{d,op}}t} + l_{\mathrm{d,mw}}\hat{a}^\dagger e^{-i\omega_{\mathrm{mag}}t} + l_{\mathrm{d,mw}}\hat{a}e^{i\omega_{\mathrm{mag}}t},\end{aligned} \tag{2.124}$$

where $\hat{C}$ ($\hat{C}^\dagger$) is the annihilation (creation) operator of a single excitonic mode in the K-valley, $\hat{a}$ ($\hat{a}^\dagger$) is the annihilation (creation) operator of the magnons in the uniform precession magnetostatic mode, $\hat{b}$ ($\hat{b}^\dagger$) are bath mode fields, and l_{d} are the photon fluxes of the drives, where the subscript 'op' ('mw') corresponds to optical modes (microwave modes). To proceed, the out-of-plane magnetization $\hat{m}_y$ will have to be expressed in terms of magnon annihilation and creation operators. In the classical limit, the out-of-plane magnetization can be expressed as

$$\tilde{m}_y = \frac{i}{2}(\tilde{m}_- - \tilde{m}_+). \tag{2.125}$$

Using the relations Eq. (2.43), the out-of-plane magnetization operator can be written as

$$\hat{m}_y = \frac{1}{V}\gamma\frac{\hbar}{4}\sqrt{2N}\frac{i(\hat{a} - \hat{a}^\dagger)}{2}. \tag{2.126}$$

This allows for $\hat{\mathrm{H}}_{\text{int,exc-mag}}$ in Eq. (2.124) to be expressed as

$$\hat{\mathrm{H}}_{\text{int,exc-mag}} = \hbar g_{\text{mag-exc}}\frac{i(\hat{a} - \hat{a}^\dagger)}{2}\hat{C}^\dagger\hat{C}, \tag{2.127}$$

where the prefactor from Eq. (2.126) has been absorbed into the coupling rate $g_{\text{mag-exc}}$.

The Hamiltonian is in a similar form as Eq. (2.102) with the exception of the added interaction term $\hat{\mathrm{H}}_{\text{int,exc-mag}}$. In order to determine the effective Hamiltonian, the transformation of this term must be determined whereas the rest of the Hamiltonian can be treated in a similar manner to Eq. (2.102) in Section 2.4.2. For the displacement transformations, only the first term of Eq. (2.104) will have to be calculated as the last term is

already accounted for in the transformation of the rest of the Hamiltonian: Taking first the displacement transformation for the microwave drive yields

$$\hat{\tilde{\mathrm{H}}}_{\text{int,exc-mag}} = D^{\dagger}(\alpha_{\text{mag}})\hat{\mathrm{H}}_{\text{int,exc-mag}}D(\alpha_{\text{mag}}), \tag{2.128}$$

where $D(\alpha_{\text{mag}}) \equiv e^{\alpha_{\text{mag}}\hat{a}^{\dagger}-\alpha^{*}_{\text{mag}}\hat{a}}$, with the solutions for α_{mag} [Section 2.4.2]

$$\alpha_{\text{mag}} = \underbrace{-\frac{2\sqrt{\gamma_{\text{mw}}}}{\gamma_{\text{T, mag}}}\sqrt{\frac{P_{\text{d,mw}}}{\hbar\omega_{\text{mag}}}}}_{\sqrt{n_{\text{mag}}}e^{i\pi}} e^{-i\omega_{\text{mag}}t}, \tag{2.129}$$

$$\sqrt{n_{\text{mag}}} \equiv \frac{2\sqrt{\gamma_{\text{mw}}}}{\gamma_{\text{T, mag}}}\sqrt{\frac{P_{\text{d,mw}}}{\hbar\omega_{\text{mag}}}}, \tag{2.130}$$

where n_{mag} is the added number of magnons induced by the microwave drive, and $\gamma_{\text{T, mag}} \equiv \gamma_{\text{mw}} + \gamma_{\text{e, mag}}$ is the total dissipation rate of the magnons, with $\gamma_{\text{e, mag}}$ denoting the nonradiative dissipation rate of the magnons. The transformed interaction Hamiltonian can then be written as [Section 2.4.2]:

$$\begin{aligned}
\hat{\tilde{\mathrm{H}}}_{\text{int,exc-mag}} &= \hbar g_{\text{mag-exc}} i\Big(\frac{\hat{a} + \alpha_{\text{mag}} - \hat{a}^{\dagger} - \alpha^{*}_{\text{mag}}}{2}\Big)\hat{C}^{\dagger}\hat{C} \\
&= \hbar g_{\text{mag-exc}} i\frac{\hat{a} - \hat{a}^{\dagger}}{2}\hat{C}^{\dagger}\hat{C} + \hbar g_{\text{mag-exc}}\sqrt{n_{\text{mag}}} i \underbrace{\frac{e^{-i(\omega_{\text{mag}}t-\pi)} - e^{i(\omega_{\text{mag}}t-\pi)}}{2}}_{-i\sin(\omega_{\text{mag}}t-\pi)}\hat{C}^{\dagger}\hat{C} \\
&\approx \hbar g_{\text{mag-exc}}\sqrt{n_{\text{mag}}}\sin(\omega_{\text{mag}}t+\pi)\hat{C}^{\dagger}\hat{C}.
\end{aligned} \tag{2.131}$$

The first term in the second line is ignored as it is dependent on quantum fluctuations of the magnonic mode and provides a negligible contribution compared to the term dependent on the coherent drive. The sine function is rewritten as $\sin(\omega_{\text{mag}}t - \pi) = \cos(\omega_{\text{mag}}t - 3\pi/2)$ in order to comply with conventions used in Section 3.2.1[9]. The phase offset $-3\pi/2$ in the cosine is neglected as the instantaneous phase has no impact on the dynamics of the system. Applying the transformation for the optical drive yields

$$\hat{\mathrm{H}}_{\text{int,exc-mag,eff}} = D^{\dagger}(\alpha_{\text{exc}})\hat{\tilde{\mathrm{H}}}_{\text{int,exc-mag}}D(\alpha_{\text{exc}}), \tag{2.132}$$

$$D(\alpha_{\text{exc}}) \equiv e^{\alpha_{\text{exc}}\hat{C}^{\dagger}-\alpha^{*}_{\text{exc}}\hat{C}}, \tag{2.133}$$

$$\alpha_{\text{exc}} = \underbrace{\frac{\sqrt{\gamma_{\text{op}}}}{i(\omega_{\text{exc}} - \omega_{\text{d,op}}) - \frac{\gamma_{\text{T, exc}}}{2}}\sqrt{\frac{P_{\text{d,op}}}{\hbar\omega_{\text{d,op}}}}}_{\tilde{\alpha}_{\text{exc}}} e^{-i\omega_{\text{d,op}}t}, \tag{2.134}$$

$$\tilde{\alpha}_{\text{exc}} \equiv \frac{\sqrt{\gamma_{\text{op}}}}{i(\omega_{\text{exc}} - \omega_{\text{d,op}}) - \frac{\gamma_{\text{T,exc}}}{2}}\sqrt{\frac{P_{\text{d,op}}}{\hbar\omega_{\text{d,op}}}}, \tag{2.135}$$

where $\gamma_{\text{T,exc}} \equiv \gamma_{\text{op}} + \gamma_{\text{e, exc}}$ is the total dissipation rate of the excitons, with $\gamma_{\text{e, exc}}$ denoting the nonradiative dissipation rate. Ignoring the non-operator valued terms then yields the effective interaction Hamiltonian

$$\begin{aligned}
\hat{\mathrm{H}}_{\text{int,exc-mag,eff}} &= \hbar g_{\text{mag-exc}}\sqrt{n_{\text{mag}}}\cos(\omega_{\text{mag}}t)\hat{C}^{\dagger}\hat{C} \\
&\quad + \hbar g_{\text{mag-exc}}\sqrt{n_{\text{mag}}}\cos(\omega_{\text{mag}}t)\Big(\hat{C}^{\dagger}\tilde{\alpha}^{*}_{\text{exc}}e^{-i\omega_{\text{d,op}}t} + \tilde{\alpha}_{\text{exc}}\hat{C}e^{i\omega_{\text{d,op}}t}\Big) \\
&\approx \hbar g_{\text{mag-exc}}\cos(\omega_{\text{mag}}t)\hat{C}^{\dagger}\hat{C}.
\end{aligned} \tag{2.136}$$

[9] In the case where the microwave drive is not exactly on resonance, the cosine term should additionally include a contribution corresponding to $\mathrm{Arg}(\tilde{\alpha}_{\text{mag}})$ which is dependent on the drive frequency.

The first term in the first line is linear in $\hat{C}^\dagger\hat{C}$, and thus represents an energy shift of the excitonic mode, whereas the second term has the same shape as the driving term in Eq. (2.102), and thus represents a magnon-induced displacement of the excitonic mode. The magnon-induced displacement is expected to be small compared to the optical drive-induced displacement, and has been neglected in the final line.

As the effective magnon–exciton interaction term can be approximated as a shift to the resonance frequency of the excitonic mode, we suppose the effect of the coupling is most easily measured on the optical side. Hence, it is of interest to find an expression for the output optical field $\hat{b}_{\mathrm{op,out}}$, which can be obtained using the input-output relation for the excitonic coupled to optical fields, and the solution of the quantum Langevin equation of the excitonic annihilation operator.

Following the derivation in Section 2.4.2 yields an approximate effective Hamiltonian of the form

$$\begin{aligned}\hat{\mathrm{H}}_{\text{exc-mag,eff}} &= \hbar\Delta\omega_{\text{exc,eff}}(t)\hat{C}^\dagger\hat{C} + \hbar\Delta\omega_{\mathrm{mag}}\hat{a}^\dagger\hat{a} \\ &\quad + \hbar\int_{-\infty}^{\infty}\frac{\mathrm{d}\omega}{2\pi}\Delta\omega_{\mathrm{op}}\hat{b}^\dagger_{\mathrm{op}}(\omega)\hat{b}_{\mathrm{op}}(\omega) + \hbar\int_{-\infty}^{\infty}\frac{\mathrm{d}\omega}{2\pi}\Delta\omega_{\mathrm{mw}}\hat{b}^\dagger_{\mathrm{mw}}(\omega)\hat{b}_{\mathrm{mw}}(\omega) \\ &\quad + i\hbar\sqrt{\gamma_{\mathrm{op}}}\int_{-\infty}^{\infty}\frac{\mathrm{d}\omega}{2\pi}\Big[\hat{b}^\dagger_{\mathrm{op}}(\omega)(\hat{C}+\tilde{\alpha}_{\mathrm{exc}}) - (\hat{C}^\dagger+\tilde{\alpha}^*_{\mathrm{exc}})\hat{b}_{\mathrm{op}}(\omega)\Big] \\ &\quad + i\hbar\sqrt{\gamma_{\mathrm{mw}}}\int_{-\infty}^{\infty}\frac{\mathrm{d}\omega}{2\pi}\Big[\hat{b}^\dagger_{\mathrm{mw}}(\omega)(\hat{a}+\sqrt{n_{\mathrm{mag}}}) - (\hat{a}^\dagger+\sqrt{n_{\mathrm{mag}}})\hat{b}_{\mathrm{mw}}(\omega)\Big],\end{aligned} \tag{2.137}$$

where the quantities $\Delta\omega_{\text{exc,eff}}$, $\Delta\omega_{\mathrm{mag}}$, $\Delta\omega_{\mathrm{op}}$, and $\Delta\omega_{\mathrm{mw}}$ have been defined as

$$\begin{aligned}\Delta\omega_{\text{exc,eff}}(t) &\equiv (\omega_{\mathrm{exc}} - \omega_{\mathrm{d,op}}) + g_{\text{mag-exc}}\sqrt{n_{\mathrm{mag}}}\cos\Big(\omega_{\mathrm{mag}}t\Big), \\ \Delta\omega_{\mathrm{mag}} &\equiv \omega_{\mathrm{mag}} - \omega_{\mathrm{mag}}, \\ \Delta\omega_{\mathrm{op}} &\equiv \omega - \omega_{\mathrm{d,op}}, \\ \Delta\omega_{\mathrm{mw}} &\equiv \omega - \omega_{\mathrm{mag}},\end{aligned} \tag{2.138}$$

The quantum Langevin equation for the excitonic mode can then be obtained as [Eq. (2.120)]

$$\dot{\hat{C}} = -i\Delta\omega_{\text{exc,eff}}(t)\hat{C} - \frac{\gamma_{\mathrm{T,\,exc}}}{2}(\hat{C}+\tilde{\alpha}_{\mathrm{exc}}) - \sqrt{\gamma_{\mathrm{op}}}\hat{b}_{\mathrm{op,in}}, \tag{2.139}$$

where the input field is defined as

$$\hat{b}_{\mathrm{op,in}} \equiv \int_{-\infty}^{\infty}\frac{\mathrm{d}\omega}{2\pi}e^{i\Delta\omega_{\mathrm{op}}(t-t_0)}b_{0,\mathrm{op}}(\omega), \tag{2.140}$$

where $b_{0,\mathrm{op}} \equiv b_{\mathrm{op}}|_{t=t_0}$.

In order to make use of the input-output relation, the quantum Langevin equation Eq. (2.139) must be solved. Conventionally, this is achieved by solving the Fourier-transformed quantum Langevin equation to find an expression for $\hat{C}(\omega)$ which can be put into the Fourier-transformed input-output relation to find an expression for the output field. However, as $\Delta\omega_{\text{exc,eff}}$ contains a cosine term, the Fourier transform of the quantum Langevin equation will contain an implicit relation on $\hat{C}(\omega \pm \omega_{\mathrm{mag}})$.

There are at least two ways to find approximate solutions to the implicit equation. If the implicit relation can be expanded perturbatively in orders of a small parameter,

one can approximate the solution to arbitrary order. Alternatively, if the frequency ω_{mag} varies slowly compared to the relevant timescale of the system, it can be approximated as constant. Thus, one can ignore the time-dependence of the cosine for the purposes of the Fourier transform, and use the solution of the Fourier-transformed quantum Langevin equation to find an expression for the output field. Transforming this expression back using the reverse-Fourier transform, and considering again the time-dependence of the cosine term, yields an approximate expression for the time-domain output signal.

As the signal analysis will examine the Fourier spectrum of the output field, we will take the first approach. Taking the Fourier transform of the quantum Langevin equation, Eq. (2.139), yields:

$$\begin{aligned} -i\omega\hat{C}(\omega) = &-i(\omega_{\text{exc}} - \omega_{\text{d,op}})\hat{C}(\omega) \\ &- \frac{1}{2}g_{\text{mag-exc}}\sqrt{n_{\text{mag}}}\Big[\hat{C}(\omega+\omega_{\text{mag}}) + \hat{C}(\omega-\omega_{\text{mag}})\Big] \\ &- \frac{\gamma_{\text{T, exc}}}{2}\Big[\hat{C}(\omega) + \tilde{\alpha}_{\text{exc}}\delta(\omega)\Big] - \sqrt{\gamma_{\text{op}}}\hat{b}_{\text{op,in}}(\omega), \end{aligned} \tag{2.141}$$

which has the solution for $\hat{C}(\omega)$:

$$\begin{aligned} \hat{C}(\omega) = &\frac{-\sqrt{\gamma_{\text{op}}}\hat{b}_{\text{op,in}}(\omega) - \frac{\gamma_{\text{T, exc}}}{2}\tilde{\alpha}_{\text{exc}}\delta(\omega)}{-i\Big(\omega - (\omega_{\text{exc}} - \omega_{\text{d,op}})\Big) + \frac{\gamma_{\text{T, exc}}}{2}} \\ &- \frac{g_{\text{mag-exc}}\sqrt{n_{\text{mag}}}}{2}\frac{\hat{C}(\omega+\omega_{\text{mag}}) + \hat{C}(\omega-\omega_{\text{mag}})}{-i\Big(\omega - (\omega_{\text{exc}} - \omega_{\text{d,op}})\Big) + \frac{\gamma_{\text{T, exc}}}{2}}. \end{aligned} \tag{2.142}$$

Setting $\hat{b}_{\text{op,in}} = 0$, as the thermal occupancy of optical modes is negligible even at room-temperature, and defining the function

$$\beta(\omega) = \frac{g_{\text{mag-exc}}\sqrt{n_{\text{mag}}}}{2i\Big(\omega - (\omega_{\text{exc}} - \omega_{\text{d,op}})\Big) - \gamma_{\text{T, exc}}},$$

Eq. (2.142) can be solved iteratively in powers of $\beta(\omega)$ as

$$\begin{aligned} \hat{C}_1(\omega) &= \frac{\gamma_{\text{T, exc}}\tilde{\alpha}_{\text{exc}}}{g_{\text{mag-exc}}\sqrt{n_{\text{mag}}}}\beta(\omega)\delta(\omega) \\ \hat{C}_2(\omega) &= \hat{C}_1(\omega) + \beta(\omega)\Big(\hat{C}_1(\omega+\omega_{\text{mag}}) + \hat{C}_1(\omega-\omega_{\text{mag}})\Big) \\ \hat{C}_3(\omega) &= \hat{C}_2(\omega) + \beta(\omega)\Big(\hat{C}_2(\omega+\omega_{\text{mag}}) + \hat{C}_2(\omega-\omega_{\text{mag}})\Big) \\ &\vdots \\ \hat{C}_n(\omega) &= \hat{C}_{n-1}(\omega) + \beta(\omega)\Big(\hat{C}_{n-1}(\omega+\omega_{\text{mag}}) + \hat{C}_{n-1}(\omega-\omega_{\text{mag}})\Big), \end{aligned} \tag{2.143}$$

where $\hat{C}_n$ is the nth iteration of the Fourier solution to the quantum Langevin equation.

As terms from higher iteration orders will contain factors of $\beta(a\omega_{\text{mag}})\beta(b\omega_{\text{mag}})$ where a is a non-zero integer and b is an integer, $\beta(a\omega_{\text{mag}})\beta(b\omega_{\text{mag}})) < 1$ denotes the domain of validity for our approach, as the nth solution would otherwise diverge for increasing n. Thus a strict requirement for the validity of the approach is $g^2_{\text{exc-mag}}n_{\text{mag}} < (\omega_{\text{mag}} + \gamma_{\text{T, exc}})\gamma_{\text{T, exc}}$.

One can generally split coupled systems into a set of regimes depending on how strong the coupling g is compared to the dissipation γ and characteristic frequency ω_0. Of special interest is the *strong coupling regime*, where $g > \kappa$, and the *ultrastrong* and *deep-strong coupling regimes*, where $g \lesssim \omega_0$ and $g > \omega_0$, respectively [42]. The derivation can accommodate coupling in the strong regime, $g_{\text{mag-exc}}\sqrt{n_{\text{mag}}} > \gamma_{\text{T, exc}}$, as long the coupling is significantly weaker than ultrastrong and deep-strong coupling, $g_{\text{mag-exc}}\sqrt{n_{\text{mag}}} \ll \omega_{\text{mag}}$, such that $g^2_{\text{exc-mag}} n_{\text{mag}} < \omega_{\text{mag}}\gamma_{\text{T, exc}}$. It is expected that the derivation will be invalid in the ultrastrong and deep-strong coupling regimes, as the RWA is not valid for such strongly coupled systems [42].

Neglecting terms of second order in $\beta(\omega - a\omega_{\text{mag}}))$, i. e. approximating $\hat{C}(\omega) \approx \hat{C}_2(\omega)$, the solution to the quantum Langevin equation is written as

$$\begin{aligned}\hat{C}(\omega) \approx{}& \frac{\gamma_{\text{T, exc}}\tilde{\alpha}_{\text{exc}}\delta(\omega)}{2i\Big(\omega - (\omega_{\text{exc}} - \omega_{\text{d,op}})\Big) - \gamma_{\text{T, exc}}} \\ &+ \frac{g_{\text{mag-exc}}\sqrt{n_{\text{mag}}}}{2i\Big(\omega - (\omega_{\text{exc}} - \omega_{\text{d,op}})\Big) - \gamma_{\text{T, exc}}}\Bigg[\frac{\gamma_{\text{T, exc}}\tilde{\alpha}_{\text{exc}}\delta(\omega + \omega_{\text{mag}})}{2i\Big(\omega + \omega_{\text{mag}} - (\omega_{\text{exc}} - \omega_{\text{d,op}})\Big) - \gamma_{\text{T, exc}}} \\ &+ \frac{\gamma_{\text{T, exc}}\tilde{\alpha}_{\text{exc}}\delta(\omega - \omega_{\text{mag}})}{2i\Big(\omega - \omega_{\text{mag}} - (\omega_{\text{exc}} - \omega_{\text{d,op}})\Big) - \gamma_{\text{T, exc}}}\Bigg].\end{aligned} \tag{2.144}$$

Substituting into the input-output relation for driven systems, the Fourier transform of Eq. (2.123), and setting $\hat{b}_{\text{op,in}}(\omega) = 0$, the output field in the optical channel from the magnon–exciton system is expressed as

$$\begin{aligned}\hat{b}_{\text{op,out}}(\omega) &= \sqrt{\gamma_{\text{op}}}\Big(\hat{c}(\omega) + \tilde{\alpha}_{\text{exc}}\delta(\omega)\Big) \\ &= \sqrt{\gamma_{\text{op}}}\frac{2i(\omega_{\text{exc}} - \omega_{\text{d,op}})}{2i\Big(\omega_{\text{exc}} - \omega_{\text{d,op}}\Big)\Big) + \gamma_{\text{T, exc}}}\delta(\omega) \\ &\quad + \sqrt{\gamma_{\text{op}}}\frac{g_{\text{mag-exc}}\sqrt{n_{\text{mag}}}}{2i\Big(\omega - (\omega_{\text{exc}} - \omega_{\text{d,op}})\Big) - \gamma_{\text{T, exc}}}\Bigg[\frac{\gamma_{\text{T, exc}}\tilde{\alpha}_{\text{exc}}\delta(\omega + \omega_{\text{mag}})}{2i\Big(\omega + \omega_{\text{mag}} - (\omega_{\text{exc}} - \omega_{\text{d,op}})\Big) - \gamma_{\text{T, exc}}} \\ &\quad + \frac{\gamma_{\text{T, exc}}\tilde{\alpha}_{\text{exc}}\delta(\omega - \omega_{\text{mag}})}{2i\Big(\omega - \omega_{\text{mag}} - (\omega_{\text{exc}} - \omega_{\text{d,op}})\Big) - \gamma_{\text{T, exc}}}\Bigg].\end{aligned} \tag{2.145}$$

3. Experimental setup

Now that an expression for an output field containing a dependency on the magnon–exciton coupling strength has been derived, the attention is shifted to how this can be measured with an experimental setup. The goal of the experimental setup is two-fold, it should: 1. Facilitate the doubly driven magnon–exciton interaction in such a way that the optical output-fields can be measured, and 2. Establish a signal readout scheme, in which the magnon–exciton coupling strength can be determined. Both goals have related requirements that must be satisfied. There is a multitude of setups which may successfully achieve both of these goals; however, we are ultimately limited by the availability of equipment in the lab. Furthermore, a specific choice made to satisfy one of the requirements might result in additional requirements or restrictions on the experimental setup. The chapter will be structured as to give the reader a clear picture of which restrictions follow from what.

3.1 Generating a signal

In order to measure an output signal it will first have to be generated. To this end it is useful to physically picture the procedure presented in Section 2.4.3: Itinerant microwaves excite magnons which interact with the excitonic modes in an in-plane magnetized magnetic substrate–TMD monolayer heterostructure. By selectively driving the exciton in either the $+K$ or $-K$ valley by a circularly polarized optical drive, the excited exciton will experience an oscillating shift in its excitonic resonance, effectively resulting in an oscillating shift in its reflectivity. This is illustrated in Fig. 3.1.

This process requires the experimental setup to contain all of the following:

- A magnetic substrate–TMD heterostructure
- In-plane magnetic field
- Microwave drive for the magnetic substrate
- Circularly polarized optical drive for the TMD monolayer

3.1.1 YIG–$MoSe_2$ Heterostructure

The system presented in Section 2.4.3 consists of a monolayer of TMD piled onto a thin-film magnetic substrate. Yttrium iron garnet(YIG) was chosen as the magnetic substrate. YIG has a high Curie temperature of 559 K, and is widely used in microwave devices, particularly in applications of magnetostatic modes [15].

The high Curie temperature of the YIG combined with the strong excitonic binding energies of the TMDs allow for experiments to be performed on YIG–TMD samples at room temperature. Though it is of interest to characterize the magnon–exciton coupling

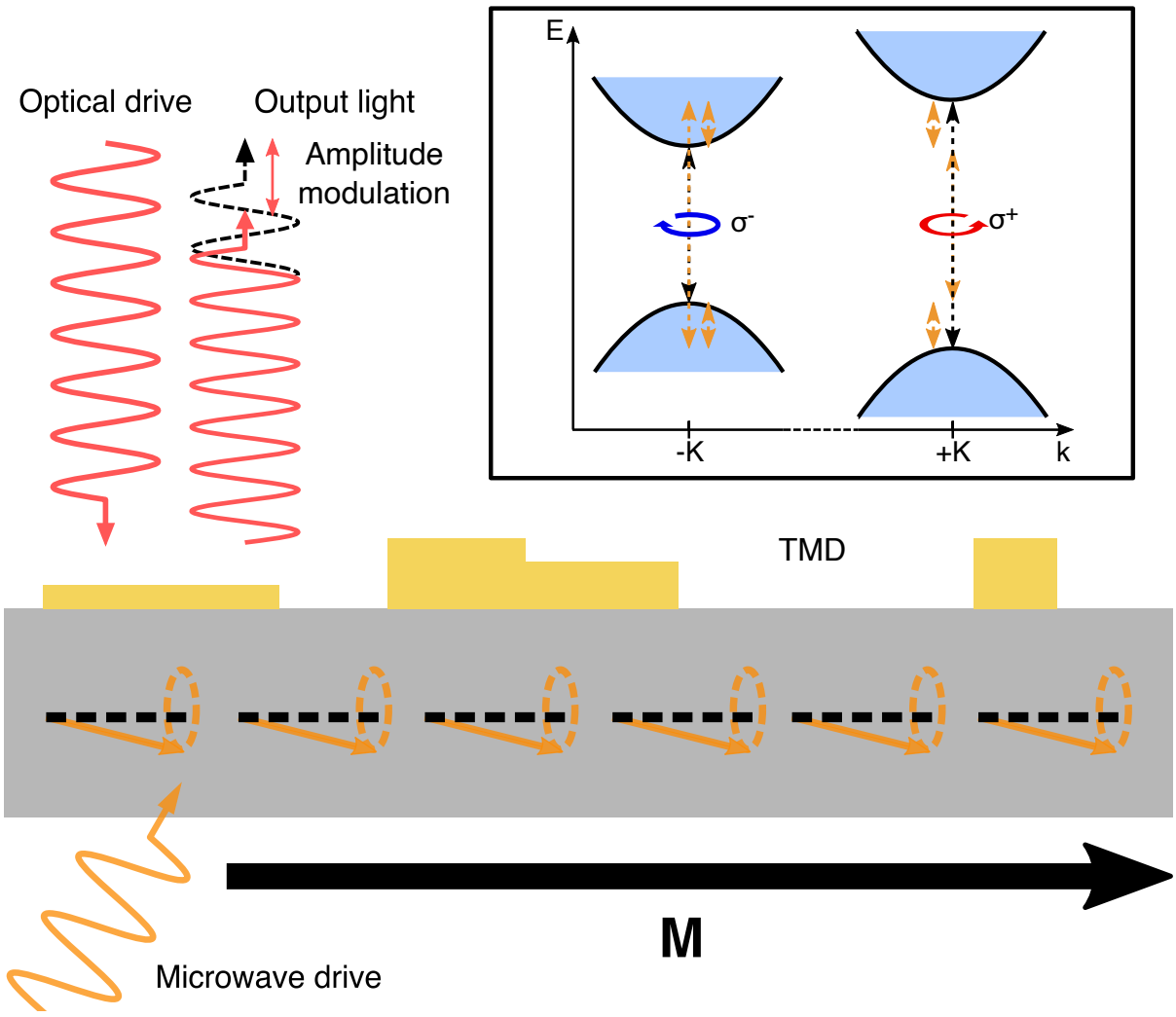

Figure 3.1: Illustration of the signal generation process. Flakes of TMD of varying thickness are situated on top of an in-plane magnetized substrate. The oscillating magnetization stemming from magnons in the uniform-precession mode induces a dynamic shift in the resonance frequency of the excitonic modes of the TMD, leading to a dynamic shift in the reflectivity for circularly polarized light. The inset is an illustration of the magnon-induced oscillation in the band gap energies at the $\pm K$ points.

at cryogenic temperatures, as many candidates for hybrid quantum systems require operation at such temperatures, the use of YIG–TMD heterostructures allowed for preliminary experiments to be performed at room temperature. The results of the preliminary experiments can be found in Ref. [39]. For these preliminary experiments, molybdenum diselenide, $MoSe_2$, was chosen as the TMD, due to the availability of a diode laser operating at a wavelength of 785 nm which is close to the resonance wavelength of the A exciton at room temperature. This diode laser was also used in the development of the experimental setup detailed in this thesis. As molybdenum diselenide samples were available from the previous experiment, Ref. [39], $MoSe_2$ was chosen as the TMD for this experimental setup. It should be noted that the experiment in Ref. [39] was limited to studying thicker multi-layer flakes of $MoSe_2$, as the signal-to-noise ratio of the thinner flakes was too small. This further motivates going to lower temperatures, as this leads to an increase in the optical response [29].

Reaching cryogenic temperatures requires the sample to be placed in a cryogenic

environment. To this end the sample is connected to the cold-finger component of a continuous-flow cryostat. In order to ensure the integrity of the sample, and in order to reach low temperatures, the sample must additionally be placed in a vacuum chamber. Otherwise, the moisture in the air might corrode the surface at low temperatures [3], and the surrounding air may act as a heat bath, limiting the cool down of the sample. Even at room temperature, placing the sample in a vacuum environment might help in minimizing degradation of the sample, as surrounding gases might otherwise react with the optical drive laser to damage the surface.

As going to cryogenic temperatures shifts the excitonic resonance frequencies of $MoSe_2$ [29], the optical drive source in such an experiment should have an adjustable frequency, ruling out the use of the fixed-frequency diode laser employed in the preliminary experiments. Hence, a Ti:sapphire laser with an adjustable driving frequency was acquired.

The samples were provided by the Iwasa lab at the University of Tokyo. The fabricated samples consist of a 10 µm thick 5 mm × 5 mm film of YIG with flakes of $MoSe_2$ piled on top. The thickness of the TMD flakes range from mono- and bilayers to flakes of thicknesses on the order of tens of layers. A single flake may itself contain several areas with different thicknesses, with areas of uniform thickness typically having dimensions of 10 µm × 10 µm. This imposes a number of new requirements on the optical drive. Firstly, the laser spot size on the surface of the sample should be confined to an area smaller than 10 µm × 10 µm. Additionally, the laser spot must be focused at the position of a given flake with high precision. To this end, it is of interest to image the surface of the sample in such a way that the position of the drive can be determined.

3.1.2 Optical drive and optics

Using a laser as the optical drive allows for the use of optical elements to control the intensity, polarization, and beam waist of the driving laser beam. This section presents the optical elements necessary for signal creation, whereas the construction of the optical elements in terms of optical components in the lab is left for Appendix D

The laser light can be modeled as a *Gaussian beam*, the shape of which can be characterized by two quantities, the *beam waist* and the *depth-of-focus*, both illustrated in Fig. 3.2. The beam waist is defined as the radial distance from the optical axis at which the beam intensity has been reduced by a factor of $1/e^2$, and can be regarded as the radius of the beam at a given point along the optical axis. The depth-of-focus on the other hand, is defined as the distance from a focus point of a beam, i. e. where the beam waist is minimized, to the point where the beam waist is a factor of $\sqrt{2}$ larger than that of the minimum value.

For most of the optical path it is practical for the light to be collimated, which means that the beam is neither converging nor diverging, i. e. a fixed beam waist. In this case the depth-of-focus is approximately infinite and will not be of any concern; the depth-of-focus is only relevant for when the light beam is focused. As for the beam waist, certain optical components require the use of optical fibers, which puts restrictions on the size of the beam waist. Hence, in the experiment, the beam waist was around 0.5 mm − 1 mm for most of the optical path.

Though the sample is placed in a vacuum environment, the vacuum chamber used is outfitted with a window, allowing for most of the optical elements to be placed outside of the vacuum chamber with no need for vacuum compatibility.

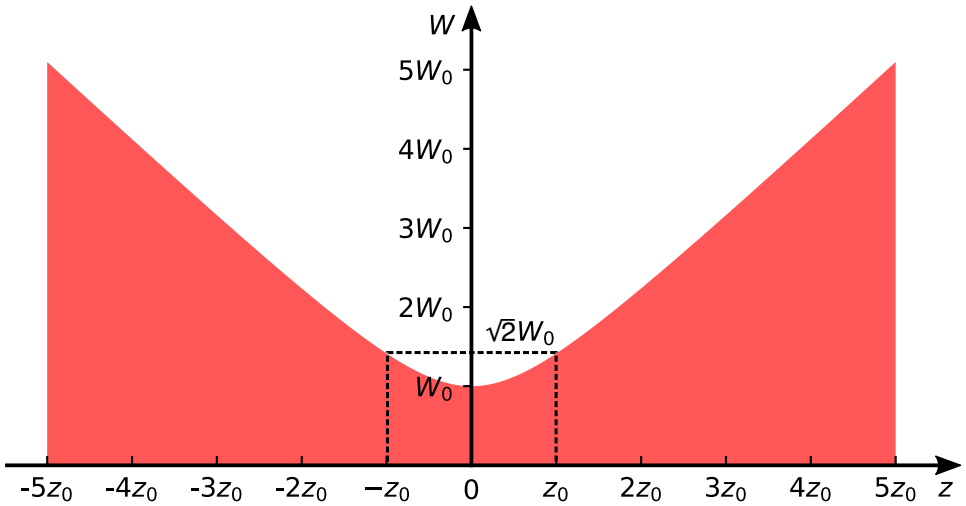

Figure 3.2: Graph of the beam waist of a focused beam. The beam waist has a minimum value of W_0 at the focal point, which is situated at $z = 0$ in the graph. The beam waist increases to a value of $\sqrt{2}W_0$ after a length z_0 which is defined as the depth of focus.

Objective lens

As the typical single-thickness dimensions of a sample TMD flake are small, the laser beam must be focused into a small spot at the sample surface by employing an objective lens. In order for the focused beam waist to be sufficiently small, the focal length of the objective lens must be quite short. Due to the placement of the sample in the vacuum chamber, the objective lens must be placed inside of the vacuum chamber to be sufficiently close to the sample surface. As a result, the conventional objective lenses available in the lab could not be used, as they consist of multiple lenses separated by media such as air, and the pressure in the pockets between the lenses is incompatible with a vacuum environment.

A single lens was instead used as the objective lens. In the case where the incoming beam is collimated, the beam waist at the focal point of a single lens, W'_{fp}, can be approximated as [43]

$$W'_{\text{fp}} \approx \frac{\lambda}{\pi W_0} f, \tag{3.1}$$

where λ is the wavelength of the light, W_0 is the beam waist of the incident light, and f is the focal length of the lens.

In order to achieve a sufficiently small spot size using a single lens with the shortest focal length commercially available, the beam waist must be increased to the order of 10 mm. To this end, an optical element known as a *Galilean expander* is added to the optical path. The Galilean expander increases or decreases the beam width of incoming light depending on its direction. The working principle and construction of the expander is detailed in Appendix D.

Using the expander and objective lens, an optical drive can be provided to a sufficiently small area of the sample. The output signal will then be contained in the light reflected from the sample. To complete the signal generation, the reflected light should be collected and isolated from the incident light. A simple way of doing so is to illuminate the sample perpendicularly, and separate the input and output light by adding a *circulator* before the objective lens. A circulator is a component with three ports where light entering

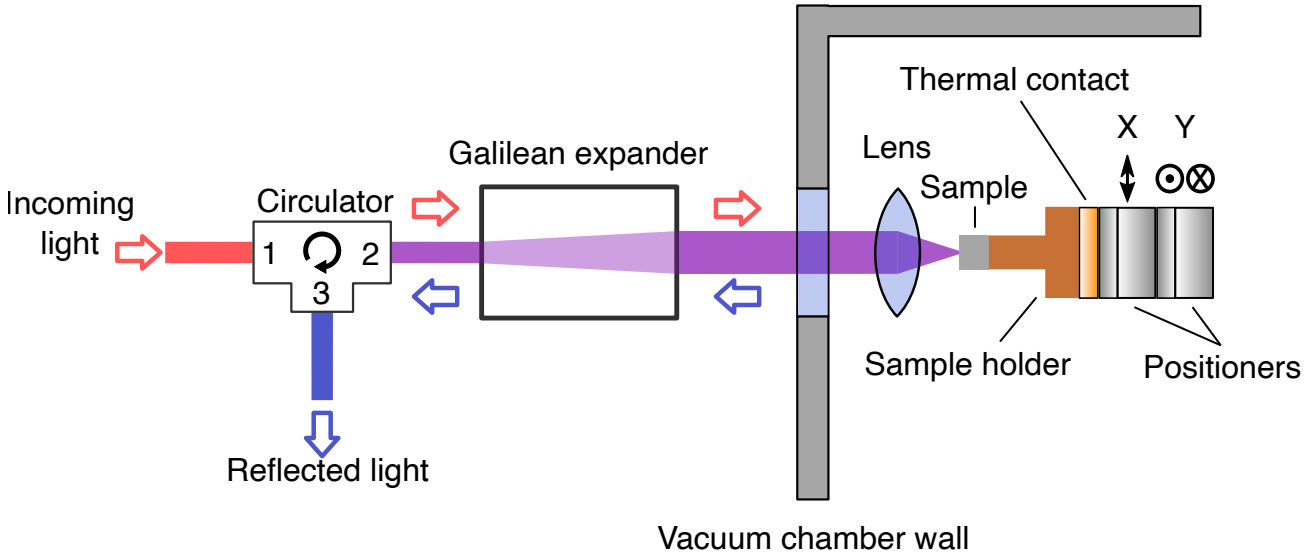

Figure 3.3: Illustration of setup of optical elements required to obtain an output signal and to perform scanning focal microscopy. The input field is colored red, and the reflected output field is colored blue. Areas where the input and output field overlap are colored purple.

one port will exit through the next port in a cyclical fashion. For our purposes, an effective circulator with functioning first and second ports suffices to separate the reflected light from the incident light, as is shown in Fig. 3.3. The construction of a circulator is detailed in Appendix D. Rather conveniently, the circulator component employed in the experiment shifts the polarization of linearly polarized light in port 1 to circularly polarized light out of port 2, such that the optical drive has the correct polarization at the sample surface provided it is linearly polarized before entering the circulator.

An optical setup with the components necessary to create an optical signal is illustrated in Fig 3.3. The schematic of the complete optical setup is shown in Fig. 3.4 where the construction of the optical components is explained in Appendix D.

Controlling the position of the optical drive and imaging the sample

With small TMD flakes and an even smaller laser spot at the sample surface, it is important that the position of the laser relative to the flakes can be determined and controlled. Additionally, as TMDs only have direct band gaps in the monolayer limit, it is important that the thickness of a given area of a flake can be identified.

To control the position of the laser spot on the sample, the sample is attached to vacuum-compatible positioners with sub-micrometer precision. An additional positioner was attached to the lens to control the relative distance to the sample surface.

Using the setup illustrated in Fig. 3.3, the sample surface can be imaged with a technique known as *scanning confocal microscopy* [44]. In scanning confocal microscopy, the reflected intensity from a contiguous set of coordinates is measured and stored as pixels, which can be put together to create an image of the sample surface. This process is illustrated in Fig. 3.5. As a coordinate position of the laser spot on the sample surface is known for every pixel of the image, scanning confocal microscopy additionally facilitates the control of the laser spot in relation to TMD flakes.

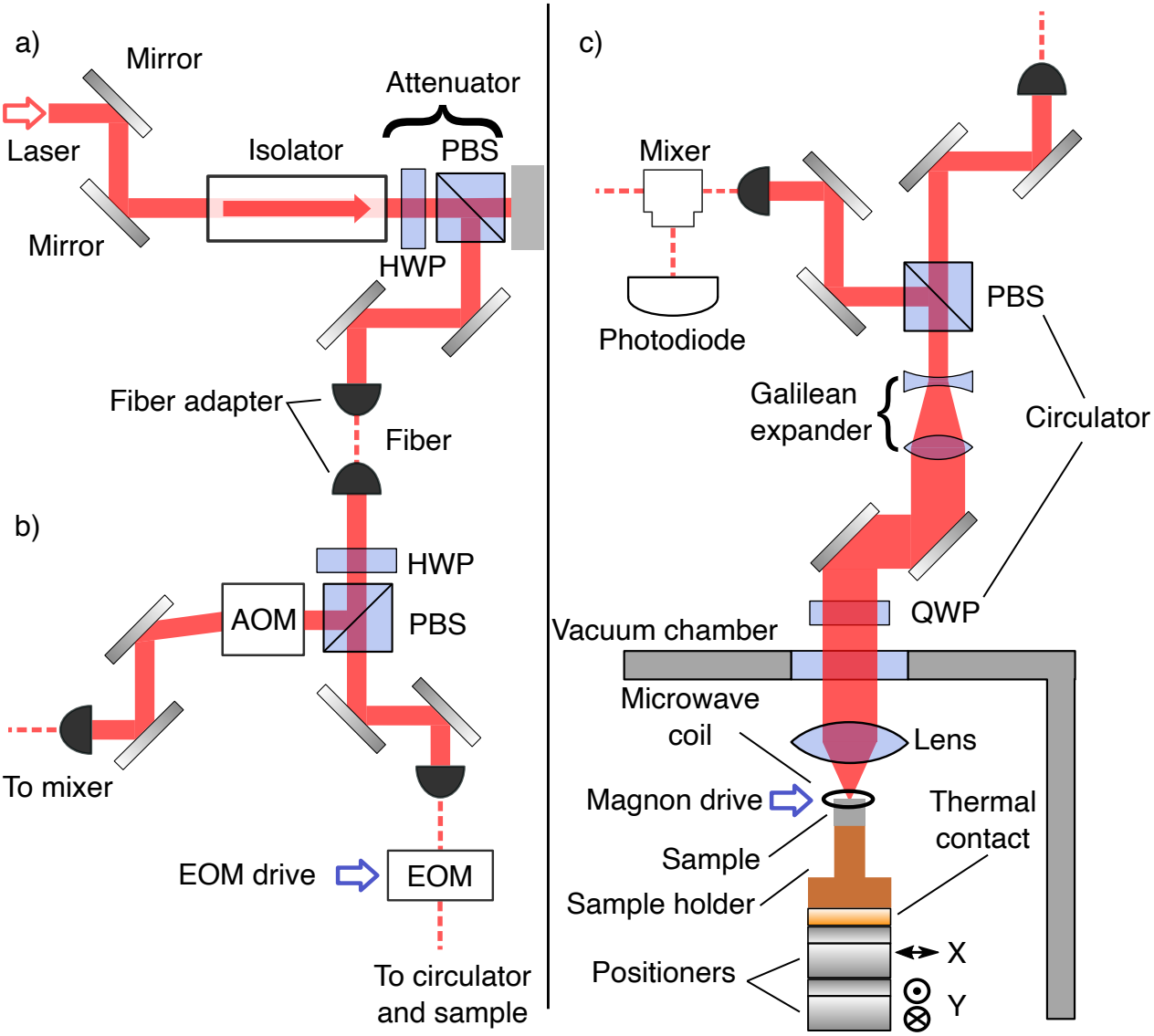

Figure 3.4: Schematic of the optical setup employed in the lab for the experiment. a) shows the setup just after the laser, which polarizes the laser with an isolator, and adjusts the intensity with an attenuator. This part is connected to area b) through an optical fiber. b) shows the construction of a local oscillator branch. A half-wave plate (HWP) is used in conjunction with a polarizing beam splitter to adjust the proportions of light that enters to the local oscillator and the sample optical path. The local oscillator branch passes through an acousto-optic modulator (AOM). When the AOM is active the resulting diffracted light of first order is passed into an optical fiber. The other branch is sent into an optical fiber where it passes through an EOM. When the EOM drive is active, the light entering into the sample optical path will be phase-modulated. c) shows optical path to the sample. The incoming light is entirely transmitted through the PBS, and the beam waist is increased by the Galilean expander. Passing through a quarter-wave plate (QWP) the light has its polarization shifted to a clockwise or counterclockwise circular polarization before entering the vacuum chamber and being focused and reflected at the sample surface. Passing back through the QWP, the reflected light has its polarization shifted to the orthogonal linear polarization, such that the polarization has been shifted 90° compared to the light prior to the QWP. The reflected light then has its beam waist reduced by the Galilean expander before its entirely reflected by the PBS, and passed into an optical fiber. The reflected light is then mixed with the local oscillator before detection by a photodiode. Not pictured is the permanent magnet, which is situated over and under the sample, such that the magnetic field is in the y direction.

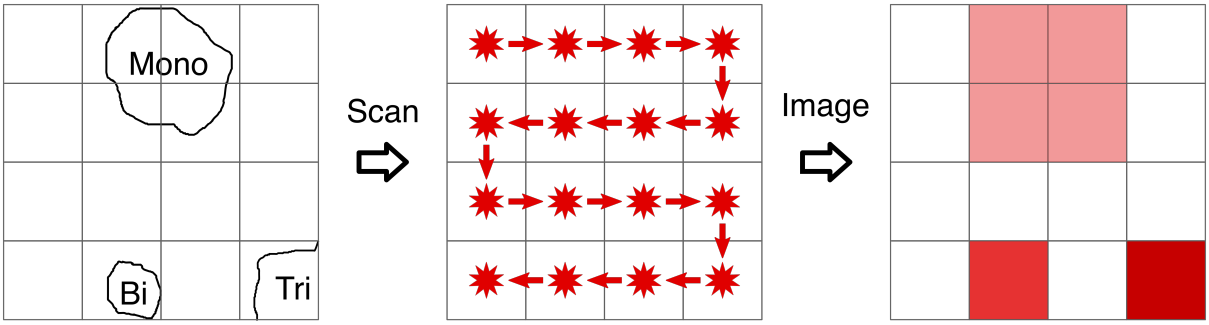

Figure 3.5: Illustration of the process of creating scanned images using scanning confocal microscopy. The star symbol corresponds to measurement of the reflected light intensity. The red arrows correspond to movement of the focused laser spot on the sample surface, which in the experiment is achieved by moving the sample.

Determination of flake thickness

Flake positions can be identified from the images by the contrast in reflectivity as compared to the substrate. Furthermore, as the light will not be completely transmitted by a single layer of TMD, the reflected light from underlying layers will yield a higher reflected intensity for areas with more layers of TMD, facilitating identification of thickness for a given area of a flake.

This can be modeled, in a manner similar to what is done in Ref. [39], by writing the reflectivity of a flake with a number of layers N_L as

$$r(N_\mathrm{L}) = r_\mathrm{bg}(1 - r_\mathrm{1L})^{2N_\mathrm{L}} + r_\mathrm{1L} \sum_{k=0}^{N_\mathrm{L}-1} (1 - r_\mathrm{1L})^{2k}, \tag{3.2}$$

where r_bg is the reflectivity of the background, in this case the YIG film, and r_1L is the reflectivity of a single layer of TMD. The amplitude of the electric field of the reflected light, E_refl, can then be written as

$$E_\mathrm{refl} = r(N_\mathrm{L})E_\mathrm{i}, \tag{3.3}$$

where E_i is the amplitude of the electric field of the incoming light. The intensity of the reflected light, I_refl will then be proportional to the square of $r(N_\mathrm{L})$:

$$I_\mathrm{refl} \propto |E_\mathrm{refl}|^2 = \Big(r(N_\mathrm{L})\Big)^2 |E_\mathrm{i}|^2. \tag{3.4}$$

The model assumes each layer of TMD reflects (transmits) a ratio r_1L ($(1 - r_\mathrm{1L})$) of the incoming light. The reflected light from a given layer will then have to be transmitted through all preceding layers, each transmitting a ratio $(1 - r_\mathrm{1L})$ of the reflected light. As for the light transmitted through all layers of TMD, a fraction r_bg will be reflected by the YIG film, of which each layer of TMD will transmit a fraction of $(1 - r_\mathrm{1L})$. The total reflected light is then the sum of the light reflected by each layer of TMD and the YIG film. The treatment does not take internal reflection between layers into account, but this is expected to be negligible, as the single layer reflection was determined to be 6 % in the experiment in Ref. [39].

Thus, by determining the single layer reflectivity r_1L and background reflectivity r_bg, one can determine the thickness of a flake by comparing the reflected intensity to the reflected intensity of the background.

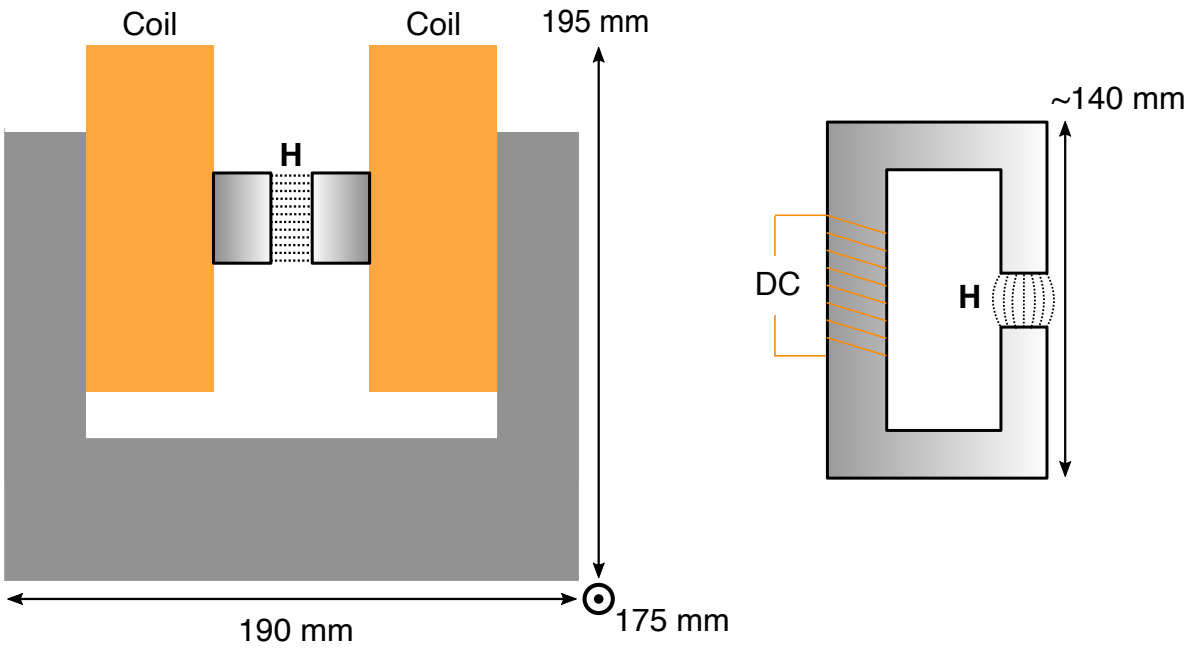

Figure 3.6: Sketch of the dimensions of the electromagnet (left) and permanent magnet (right) as well as their respective magnetic fields.

In order to determine the thickness more accurately, one can compare the scanned images with atomic force microscopy (AFM) measurements, given that the relation between the coordinates of the scanned images and AFM measurements is known. For Ref. [39], such measurements were performed by the Iwasa lab, where the sample was additionally imaged using white-light imaging, allowing for relative coordinates to be determined by comparing flake positions with scanned images. This characterization was scheduled to be performed on a given sample after the experiments in our lab had been completed. As our experiments could not be completed due to delays, this characterization was not performed on our sample.

3.1.3 Microwave drive and in-plane magnetization

In order to excite magnons with a corresponding out-of-plane magnetization, a harmonically oscillating out-of-plane microwave drive must be supplied to an in-plane magnetized substrate.

To magnetize the substrate, a magnet must be placed in the vacuum chamber. Two types of magnets were available in the lab for this purpose: an electromagnet and a permanent magnet. The electromagnet provides a highly uniform magnetic field with good controllability of the applied field strength over a relatively large volume, at the expense of taking up a lot of space. The permanent magnet on the other hand, taking up considerably less space, provides a less uniform magnetic field over a smaller volume, with no controllability of the applied field strength. Due to the limited space available in the vacuum chamber, the permanent magnet was chosen. Additionally, a coil was attached to the magnet to allow for small adjustments of the magnetic field by supplying a DC voltage. As the sample dimensions themselves were small, the smallness and relative lack of uniformity of the magnetic field were not expected to be problematic. Fig. 3.6 shows a comparative illustration of the spatial dimensions and applied magnetic fields of the permanent magnet and electromagnet.

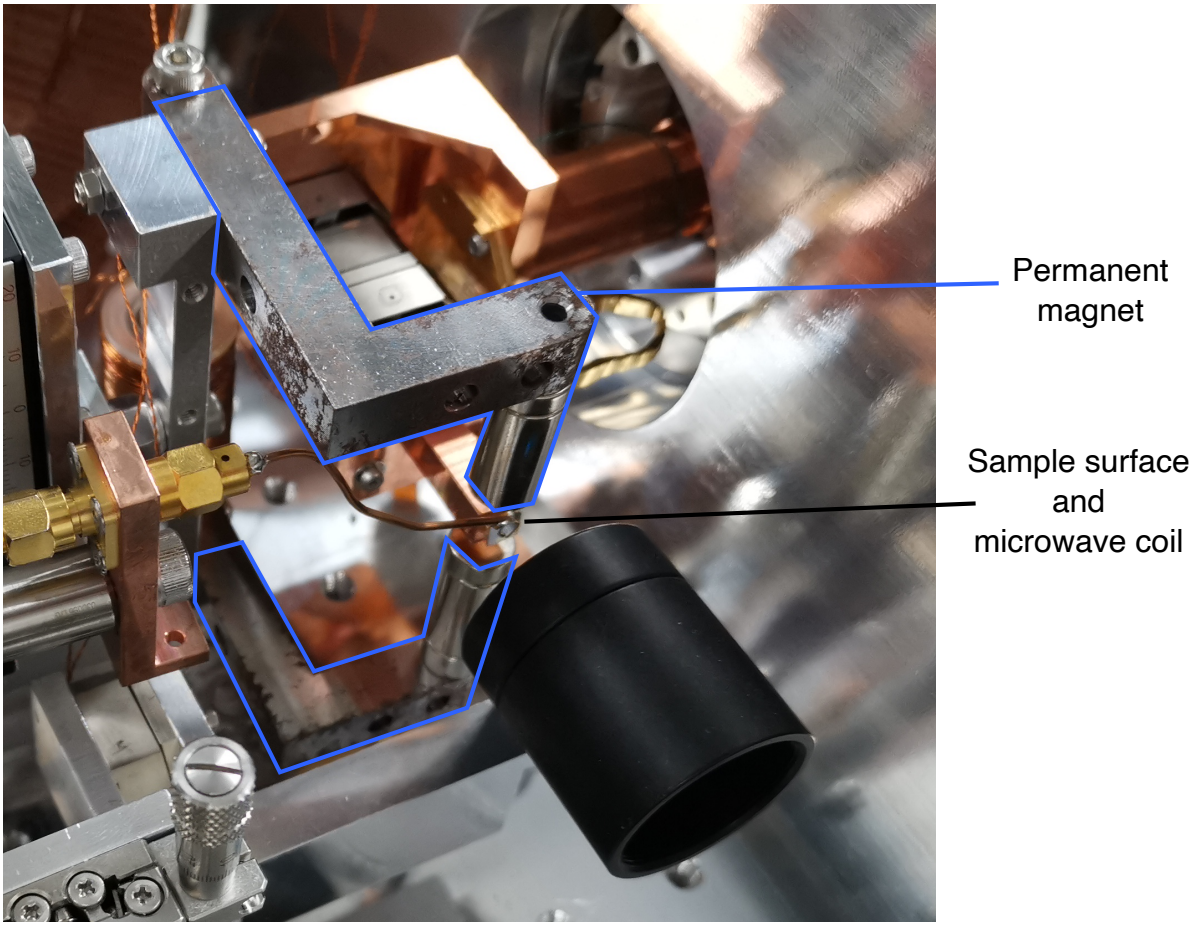

Figure 3.7: Photo of the permanent magnet, sample, and the microwave coil in the vacuum chamber. The permanent magnet is outlined in blue. The objective lens is also visible down and to the right of the sample surface.

With the substrate magnetized, magnons can be excited by placing a one-loop coil bearing a microwave-frequency alternating current close to the sample surface. The current in the coil will induce an oscillating out-of-plane magnetic field which can be described in the form presented in Section 2.2.3. Fig. 3.7 shows a photo of the permanent magnet, sample, and microwave coil placed inside of the vacuum chamber.

The coil is connected to a *network analyzer*, allowing for the measurement of ferromagnetic resonance, which is measured by recording the proportion between the output power of the network analyzer and the power returning from the coil, referred to as the reflected power. The excitation of magnons will absorb some of the microwave power, and as such decrease the reflected power relative to the incoming power. Plotting the ratio $\mathrm{S11} \equiv \frac{\text{reflected power}}{\text{output power}}$ for a range of frequencies, the resonance frequencies of different magnon modes can be identified as dips in the spectrum. Substituting the solution to the Fourier transform of Eq. (2.98) into the input–output relation[1] Eq. (2.95) one can obtain the following expression for $\mathrm{S11} \equiv \hat{b}_{\mathrm{out}}/\hat{b}_{\mathrm{in}}$

$$\mathrm{S11}(\omega) = \frac{i(\omega - \omega_{\mathrm{m}}) - \frac{1}{2}(\gamma_{\mathrm{e}} - \gamma_{\mathrm{mw}})}{i(\omega - \omega_{\mathrm{m}}) - \frac{1}{2}(\gamma_{\mathrm{e}} + \gamma_{\mathrm{mw}})}, \tag{3.5}$$

[1]The input–output relation for the undriven case was chosen in order to treat the drive as the input field.

where ω is the frequency of the alternating current, ω_{m} is the resonance frequency of the magnonic mode, γ_{mw} is the coupling to the microwave coil and γ_{e} is the coupling to other external modes.

By fitting the measured ferromagnetic resonance to this formula, the magnon resonance frequency ω_{mag} and coupling rate γ_{mw} can be determined, which can be used to determine the effective number of magnons n_{mag}.

3.2 Signal readout

Now that the signal has been created, the magnon–exciton coupling strength can be extracted by measurement and analysis. In order to figure out how this information can be extracted from the signal, we must first understand how the information is stored.

3.2.1 Information storage in modulation-induced sidebands

To store information using light one can make use of one of its degrees of freedom. In our case, we may restrict the attention to information storage in the amplitude and phase of the complex electric field of the light

$$E(t) = A(t)e^{i\theta(t)}, \tag{3.6}$$

where $A(t)$ and $\theta(t)$ is the amplitude and phase of the light, respectively, and spatial dependence has been suppressed for simplicity. Assuming the light is initially in the form of a plane wave with amplitude A_0 and frequency ω,

$$E_0(t,\omega) = A_0 e^{-i\omega t}, \tag{3.7}$$

information may be stored by *amplitude modulation*(AM) or *phase modulation*(PM). These methods are also conventionally used in radio communication for information storage and transmission using radio waves [45]. Using amplitude- and phase-modulation, the information is stored in what is known as *sidebands* in the frequency spectrum of the waves. Assuming harmonic time-dependence for simplicity, modulation of amplitude and phase can be expressed as [45]

$$A(t) = A_0\Big(1 - \frac{M}{2}\big[1 - \cos(\omega_{\mathrm{mod}}t)\big]\Big), \tag{3.8}$$

$$\theta(t) = \omega t + M\cos(\omega_{\mathrm{mod}}t), \tag{3.9}$$

where M and ω_{mod} are denoted as the *modulation depth* and *modulation frequency* respectively.

The electric field of amplitude-modulated light can then be expressed as

$$\begin{aligned} E(t,\omega)_{\mathrm{AM}} &= A_0\Big(1 - \frac{M}{2}\big[1 - \cos(\omega_{\mathrm{mod}}t)\big]\Big)e^{-i\omega t} \\ &= A_0\Big(1 - \frac{M}{2}\Big)e^{-i\omega t} + A_0\frac{M}{4}\Big(e^{-i\left(\omega+\omega_{\mathrm{mod}}\right)t} + e^{-i\left(\omega-\omega_{\mathrm{mod}}\right)t}\Big), \end{aligned} \tag{3.10}$$

which is equivalent to the sum of three waves, one with the original frequency denoted as the *carrier*, and an additional two with a positive or negative frequency shift denoted as the upper and lower *sideband* respectively. The term sideband originates from the shape of the Fourier spectrum of such a wave, as seen in Fig 2a).

The electric field of phase-modulated light can be written as [45]:

$$E(t,\omega)_{\mathrm{PM}} = A_0 e^{-i\omega t} e^{-iM\cos(\omega_{\mathrm{mod}}t)} \tag{3.11}$$

$$\begin{aligned} &= A_0 e^{-i\omega t}\Big[1 + iM\cos(\omega_{\mathrm{mod}}t) - \frac{M^2}{2}\cos^2(\omega_{\mathrm{mod}}t) + \dots\Big] \\ &= A_0\Big[\Big(1 - \frac{M^2}{4} + \cdots\Big)e^{i\omega t} \\ &\quad + i\Big(\frac{M}{2} + \cdots\Big)\Big(e^{-i\Big(\omega+\omega_{\mathrm{mod}}\Big)t} + e^{-i\Big(\omega-\omega_{\mathrm{mod}}\Big)t}\Big) \\ &\quad - \Big(\frac{M^2}{8} + \cdots\Big)\Big(e^{-i\Big(\omega+2\omega_{\mathrm{mod}}\Big)t} + e^{-i\Big(\omega-2\omega_{\mathrm{mod}}\Big)t} \\ &\quad + \cdots\Big). \end{aligned} \tag{3.12}$$

In principle, phase-modulated light contains an infinite number of sidebands. In the case where the modulation depth is small $M \ll 1$, higher order terms can be neglected to obtain a two-band approximation for phase-modulated light:

$$E(t,\omega)_{\mathrm{PM}} \approx A_0\Big[e^{-i\omega t} + i\frac{M}{2}\Big(e^{-i(\omega+\omega_{\mathrm{mod}})t} + e^{-i(\omega-\omega_{\mathrm{mod}})t}\Big)\Big]. \tag{3.13}$$

An illustration of the spectrum of phase-modulated light is shown in Fig. 3.8b).

Beating

When two plane waves with different frequencies are added together, the total signal will have the frequency of the wave with the higher amplitude, whereas the amplitude will oscillate at the difference in frequency between the waves, a phenomenon known as *beating*. As the upper and lower sidebands from both AM and PM are equally spaced with respect to the carrier frequency, they will produce beating signals of the same frequency, where the relative phase between the beating signals determines whether the signals interfere constructively or destructively. For amplitude-modulated light, the two sidebands interfere constructively. For phase-modulated light, however, the upper and lower sidebands interfere destructively in such a way that the beating signals cancel [45]. This can also be seen from the expressions for the intensities of AM and PM signals [Eqs;(3.10) and (3.11)]:

$$I_{\mathrm{PM}}(t) \propto |E(t,\omega)_{\mathrm{PM}}|^2 = |A_O|^2, \tag{3.14}$$

$$I_{\mathrm{AM}}(t) \propto |E(t,\omega)_{\mathrm{AM}}|^2 = |A_O|^2\Big(1 - \frac{M}{2}\Big[1 - \cos(\omega_{\mathrm{mod}}t)\Big]\Big)^2, \tag{3.15}$$

meaning the intensity is oscillating for the amplitude-modulated signal, whereas the phase-modulated intensity is no different from the unmodulated intensity. This means pure phase modulation cannot be detected by a photodiode. Graphs of beating signals resulting from amplitude modulation and phase modulation are shown in Fig 3.8c) and Fig 3.8d) respectively.

3.2.2 Modulation resulting from magnon–exciton coupling

The magnon–exciton coupling results in a harmonically oscillating shift of the exciton resonance frequency, and the resultant oscillating reflectivity will modulate the amplitude of reflected light. The dynamic shift in the resonance frequency can be considered as

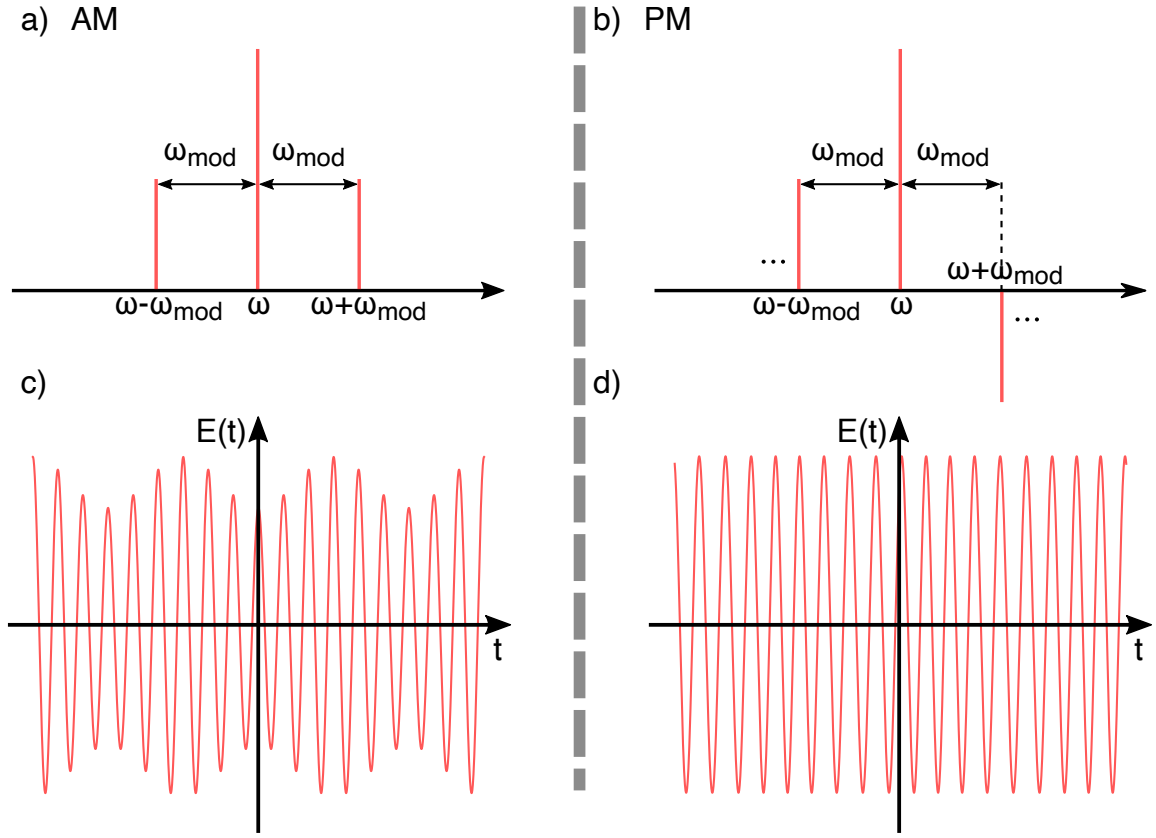

Figure 3.8: Illustration of the Fourier spectrum and recorded beating of AM- and PM-signals. a) Fourier spectrum of an amplitude-modulated signal. b) Fourier spectrum of a phase-modulated signal, showing only the first order sidebands. c) Graph of beating signal produced by amplitude modulation. Vertical axis is the electric field of the signal. d) Graph of beating signal produced by phase modulation. Vertical axis is the electric field of the signal.

a modulation, with modulation frequency $\omega_{\text{mod}} \equiv \omega_{\text{mag}}$, and modulation depth $M \equiv g_{\text{mag-exc}}\sqrt{n_{\text{mag}}}$:

$$\begin{aligned}\omega_{\text{exc, eff}} &= \omega_{\text{exc}} - \omega_{\text{d,op}} + g_{\text{mag-exc}}\sqrt{n_{\text{mag}}}\cos(\omega_{\text{mag}}t) \\ &= \omega_{\text{exc}} - \omega_{\text{d,op}} + M\cos(\omega_{\text{mod}}t).\end{aligned} \tag{3.16}$$

From this expression, it is evident that the same effect can be achieved without magnons present by using a phase-modulated drive with the same modulation frequency and modulation depth, effectively reproducing Eq. (2.145). Though the reflected signal will be both amplitude-modulated and phase-modulated, only the AM-induced sidebands will contribute to the beating with the carrier, as the PM-induced sidebands will produce beating signals that cancel.

Electro-optic modulator and optical setup for calibration

In order to introduce a controlled phase-modulation of the light, we make use of an optical component known as an *electro-optic modulator* (EOM). Light passing through an EOM experiences a phase shift as [43]

$$\theta(t) = \theta_0(t) - \pi\frac{V}{V_\pi} \tag{3.17}$$

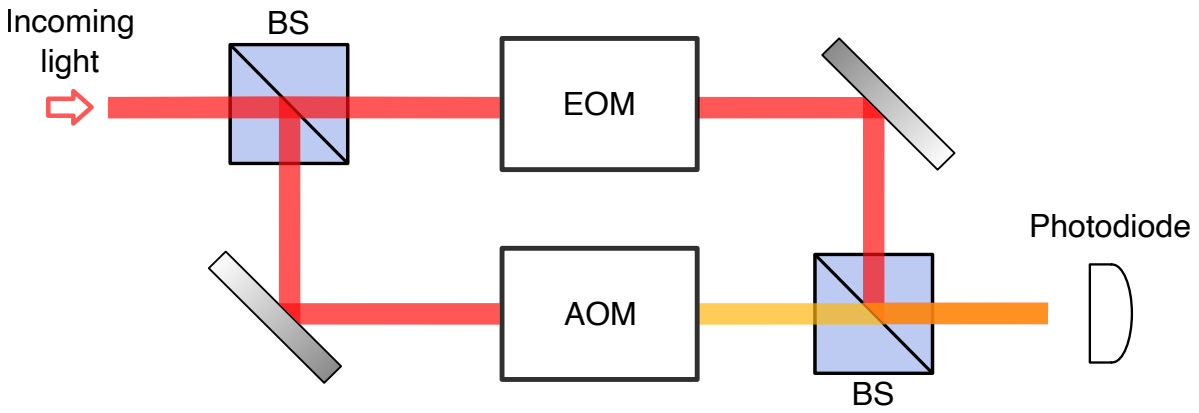

Figure 3.9: Illustration of the setup used to calibrate the electro-optic modulator. The input light and phase-modulated light is colored red, whereas the freuqency shifted local oscillator is colored yellow. Areas where the phase-modulated light and local oscillator overlap are colored orange.

where $\theta_0(t)$ is the phase of the unmodulated light, V is the voltage applied to the EOM, and V_π is a parameter known as the *half-wave voltage* which is constant for a specific EOM. By applying an AC voltage, the phase of the modulated wave can be written as

$$\theta(t) = \theta_0(t) + \underbrace{\frac{-\pi V_{\text{amp}}}{V_\pi}}_{M(V_{\text{amp}})} \cos(\omega_{\text{mod}} t), \tag{3.18}$$

where V_{amp} and ω_{mod} is the amplitude and frequency, respectively, of the applied voltage, which results in a phase modulation with effective modulation depth M and modulation frequency ω_{mod} [Eq. (3.9)]. Thus, if the half-wave voltage is known, a controlled output signal can be generated in order to determine a relation between modulation depth and measured sideband amplitude.

To determine the half-wave voltage, one can examine the Fourier spectrum amplitude of one of the sidebands compared to that of the carrier and use Eq. (3.12) to determine the modulation depth. As mentioned previously, one cannot measure the sidebands of purely phase-modulated light, as the beating signals of the upper and lower sidebands cancel exactly. A simple way of circumventing this issue is to split the light into two paths, modulating the light in one path and shifting the frequency of the light in the other before mixing the two paths and measuring the light with a photodiode. The sidebands and the carrier will then produce individual beating signals with the frequency shifted unmodulated light, usually denoted as the *local oscillator*. The setup for this calibration procedure is illustrated in Fig. 3.9.

The frequency shift is provided by an *acousto-optic modulator*(AOM). Light passing through an AOM interacts with an acoustic wave, which leads to diffraction of the light beam [43]. The diffracted light experiences a Doppler frequency shift with the sign and magnitude dependent on the order of the diffraction peak [43]. Thus, by isolating a diffraction peak of non-zero order, the acousto-optic modulator will effectively provide an attenuation[2] and frequency shift of the incident light.

[2]As all other diffraction peaks are blocked.

4. Experimental results

Using the experimental setup presented in the previous chapter we can perform a number of experiments. The first experiments aim to determine the resonance frequency of the magnons and excitons, and identify flake positions on the sample. Using this information, the final experiment can be carried out to determine the magnon–exciton coupling strength. Unfortunately, due to the COVID-19 pandemic, only the first two experiments presented could be performed. As for the rest of the experiments, the planned experimental procedure is presented.

4.1 Ferromagnetic resonance

Ferromagnetic resonance is measured by recording the S11 spectrum, which in this case is defined as the reflected microwave power from the microwave coil normalized by the power sent into the coil. By measuring the ferromagnetic resonance, one can determine the resonance frequencies of the magnetostatic modes in the substrate. This information is used in subsequent experiments to drive the magnetostatic mode of interest at resonance.

Measured ferromagnetic resonance is shown in Fig. 4.1, along with a curve fitting of one of the modes obtained using Eq. (3.5). The unknown parameters in Eq. (2.54) were determined by the fitting to be $\omega_0 = \omega_{\text{mag}} = 7.148\,\text{GHz}$, $\gamma_{\text{mw}} = 0.235\,\text{MHz}$, $\gamma_{\text{T}} = \gamma_{\text{e}} + \gamma_{\text{mw}} = 2.334\,\text{MHz}$ for the specific mode shown in Fig.4.1b).

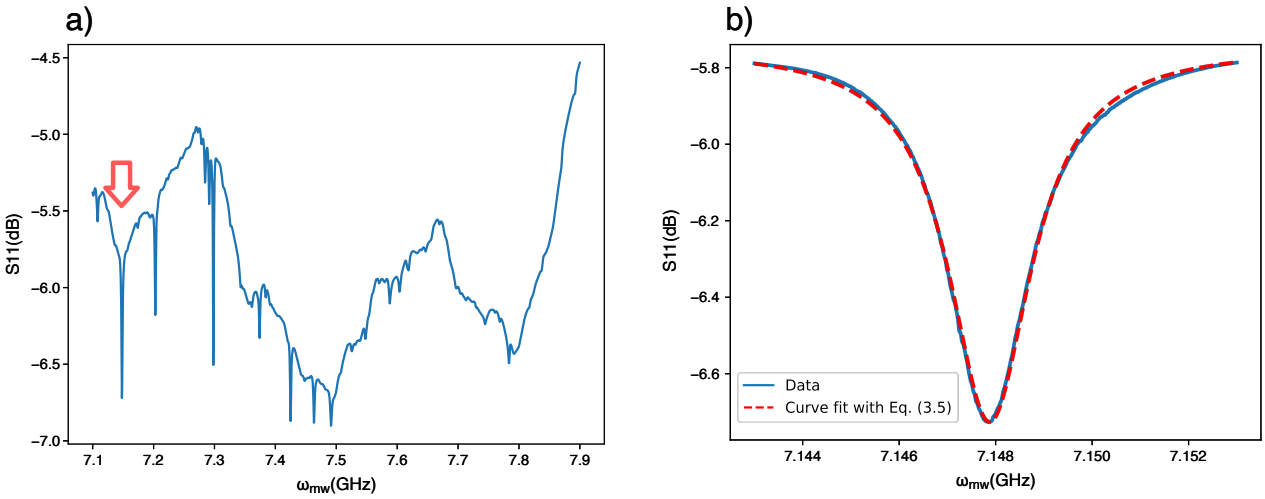

Figure 4.1: Ferromagnetic resonance (FMR) characterized by the S11 spectrum for the microwave coil. a) FMR spectrum over a large frequency span. The dips correspond to absorption of energy due to excitation of magnons in a magnetostatic mode in the substrate. The large variations over long spans of frequency are due to the spectral response of the components and constitute noise. The red arrow shows the relative position of the high-resolution spectrum. b) High-resolution spectrum around a single magnetostatic mode. The dashed red line corresponds to a curve fit of Eq. (3.5) with the parameters $\omega_{\text{mag}} = 7.148\,\text{GHz}$, $\gamma_{\text{e}} = 2.099\,\text{MHz}$, and $\gamma_{\text{mw}} = 0.235\,\text{MHz}$.

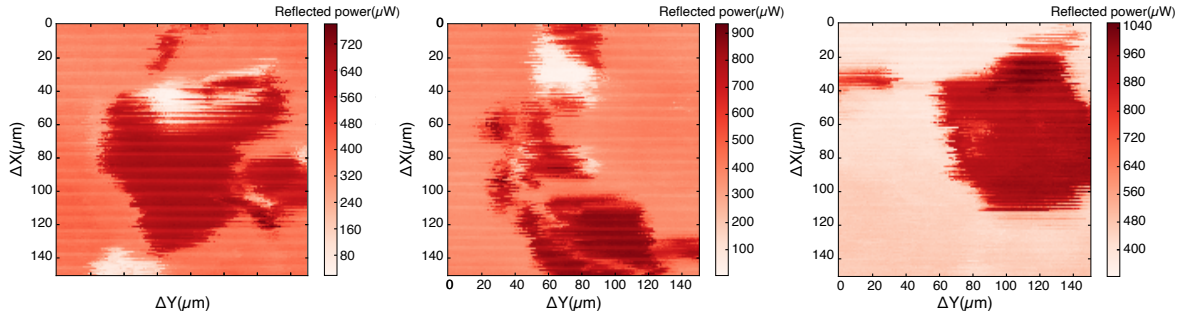

Figure 4.2: High resolution scans of three areas on the sample surface obtained with a Galilean expander in the optical setup. The areas with a higher reflectivity correspond to flakes of $MoSe_2$.

4.2 Imaging with scanning confocal microscopy

The sample surface is imaged using a technique known as *scanning confocal microscopy*, which is presented in more detail in Section 3.1.2.

Fig. 4.2 shows scanned images of three areas containing particularly large flakes on the sample. The results presented are preliminary results obtained during the development of the experimental procedure, using the diode laser. The white areas shown are expected to be the result of the surface being uneven, i. e. not completely flat, such that light was reflected out of the optical setup. Unfortunately, sufficient data was not recorded to determine the parameters in Eq. (3.2), and as such, the thickness of the flakes in the scan cannot be estimated.

4.2.1 Effect of the Galilean expander

The addition of a Galilean expander results in a smaller focused spot size on the sample surface, leading to an increased contrast in the recorded image. The difference in contrast in the image of three flakes with and without the Galilean expander is shown in Fig. 4.3. The intensity of the incident light was adjusted between measurements, however the reflected light in the setup with a Galilean expander was reduced by about a factor of 3 compared to the setup without an expander.

4.3 Reflection spectroscopy

When going to lower temperatures, it is important that the resonance frequency and the reflection spectrum at a specific temperature can be determined. To this end reflection spectroscopy was supposed to be performed as follows.

The laser spot is placed at a flake position, and the reflected intensity is recorded for a range of wavelengths. As the Ti:sapphire laser has a non-trivial power spectrum, the change in optical drive power at different wavelengths must be compensated for. This can be done by either normalizing the reflected spectrum by the spectrum of the incoming light, or by adjusting the incoming intensity for each wavelength to a set intensity.

For reference, the temperature dependence of the reflection spectrum of $MoSe_2$ on a non-magnetic substrate can be seen in Ref. [29], and the reflection spectrum of $MoSe_2$ on a ferromagnetic substrate at a low temperature can be seen in Ref. [6].

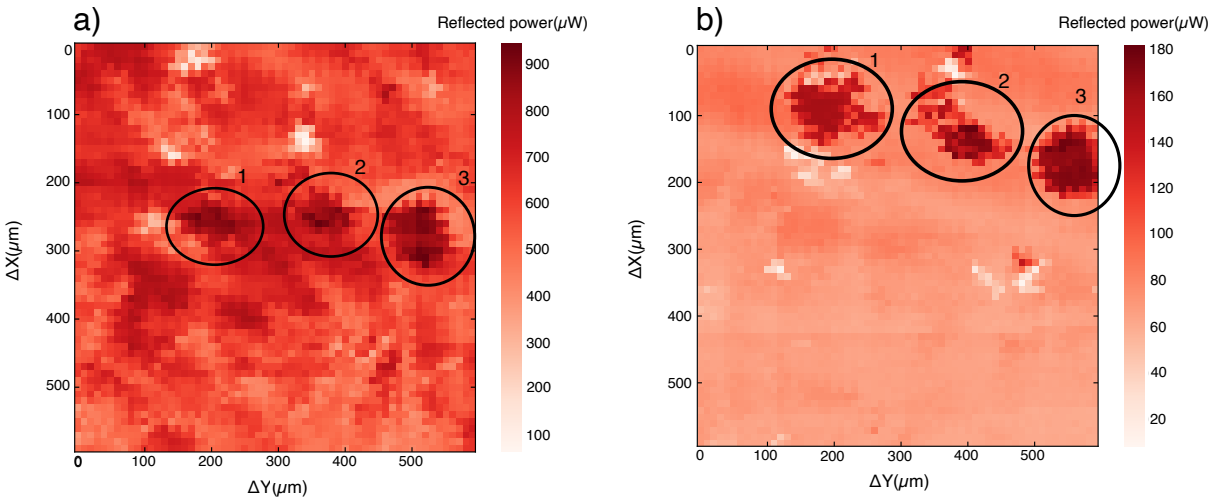

Figure 4.3: a) Low resolution scan of the sample surface performed without a Galilean expander in the optical setup. Each pixel in the scanned image corresponds to a 10 µm × 10 µm area on the sample. b) Low resolution scan of the sample surface performed with a Galilean expander added to the optical setup. Each pixel in the scanned image corresponds to a 10 µm × 10 µm area on the sample. The areas annotated as 1, 2, and 3 are assumed to represent the same areas of the sample surface for both scanned images. Higher resolution scans of these areas, taken with a higher incident optical intensity, are shown in Fig. 4.2

4.4 Determination of the magnon–exciton coupling strength

The experimental procedure to determine the coupling strength can be split into three stages. The first stage is to establish the voltage dependence of the modulation depth provided by the EOM in the experimental setup, as is detailed in Section 3.2.2. In this stage, the optical drive only passes through the AOM and EOM. For the second stage, the AOM and magnon drive are deactivated, and the phase-modulated drive is applied to the sample. The phase-modulation of the drive results in an amplitude modulation in the light reflected from the TMD flakes, and measuring the beating without the local oscillator results in the sidebands induced by the phase-modulation of the light canceling. The amplitude of the AM-induced beating can then be recorded for a range of modulation depths. In the third and final stage, the EOM is deactivated and the magnon drive is activated, such that one can compare the magnon-induced beating amplitude with the previously recorded EOM-induced beating to determine the modulation depth of the magnons. This modulation depth is equal to $g_{\text{mag-exc}}\sqrt{n_{\text{mag}}}$, where n_{mag} at resonance is given by the relation [Eq.(2.130)]

$$n_{\text{mag}} = \frac{4\gamma_{\text{mw}}}{\gamma_{\text{T, mag}}^2}\frac{P_{\text{mw}}}{\hbar\omega_{\text{mag}}}.$$

Thus, by calculating n_{mag}, one can determine the magnon–exciton coupling strength from the modulation depth.

Though this procedure was not performed in this experiment, Ref. [39] determined the magnon–exciton coupling to be $g_{\text{mag-exc}} = (6.2 \pm 0.8) \times 10^{-2}\,\text{Hz}/\sqrt{\text{magnon}}$ [$g_{\text{mag-exc}} = (7.1 \pm 0.8) \times 10^{-2}\,\text{Hz}/\sqrt{\text{magnon}}$] for $+K$ [$-K$] valley excitons in a 19-layer flake of $MoSe_2$ using a similar procedure[1]. The findings of Ref. [39] suggested that the magnon–exciton coupling may increase substantially for a decreasing number of layers of $MoSe_2$, and as such, the aim of this experiment was to characterize the magnon–exciton coupling of thinner flakes by lowering the temperature to obtain a sufficiently strong signal-to-noise ratio.

[1]It should be noted that the procedure in Ref. [39] compared the beating of single sidebands of the reflected phase-modulated drive with single sidebands of the magnon-modulated light, by using the AOM-modulated light as a local oscillator. This means the pure phase-modulation of the light also contributed to the sideband amplitude, resulting in an underestimation of the magnon–exciton coupling. The measured value may rather be considered as a lower bound for the magnon–exciton coupling of a 19-layer flake.

5. Conclusion and future directions

This thesis describes the experimental characterization of the proximity-mediated coupling between magnons and excitons in a TMD-ferromagnet van der Waals heterostructure. Using input-output theory and a Hamiltonian description of driven excitonic and magnonic modes as open quantum systems we have established an expression for an optical output signal of the coupled magnon–exciton system, where the magnon–exciton interaction induces sidebands in the spectrum of the output signal. We have constructed an experimental setup that can generate such a signal and designed a set of experiments to determine the numerical value of the magnon–exciton coupling strength. Though the final experiments could not be performed, the results of the first two experiments yield insight as to what can be done to improve the prospects of future experiments.

YIG film and ferromagnetic resonance

As is evident in Fig. 4.1, multiple magnonic modes where observed in the magnetic substrate. Though the uniform-precession mode was of most interest, discerning the resonance frequency of this specific mode from the others is a difficult task. The number of observed modes may be a result of the inhomogeneity of the magnetic field supplied by the permanent magnet. As such, it could be beneficial to replace the permanent magnet with an electromagnet with a more uniform magnetic field. The added controllability compared to the permanent magnet would also enable the investigation of the dependence of the magnonic resonance frequency on the external magnetic field, which should follow Eq. (2.33) for the uniform-precession mode.

If the difficulty in discerning the appropriate magnetostatic modes turns out to be a limiting factor even with a homogeneous magnetic field, one could additionally change the magnetic substrate geometry to a sphere. YIG spheres have well-characterized magnetostatic modes [46], and have seen extensive use in the literature [2, 7]. However, switching the substrate to a spherical geometry would make it exceedingly difficult to collect the reflected light, and as such one would have to find a different way of obtaining an experimental signal, such as placing the sphere in a cavity and examining reflection and transmission coefficients in a similar manner as Refs. [2,8]. Such a setup could potentially also facilitate the construction of TMD–magnon–superconducting qubit hybrid quantum systems, by adding a microwave cavity containing a superconducting qubit to make a double optical-and-microwave cavity.

Optical drive and Galilean expander

Due to the placement of the sample in the vacuum chamber and the strict requirements on the focused beam waist, a single lens had to be used as the objective lens, with a Galilean expander placed outside of the chamber to increase the incident beam waist. It is evident from the scans that the addition of a Galilean expander improves contrast between flakes and background and allows for the acquisition of higher resolution scans. However, as was noted in the experimental results, the reflected intensity was reduced

by around a factor of 3 compared to the setup without the expander. As the incident laser intensity should be kept low to prevent degradation of the sample quality, and for the low-excitation limit to be valid for the excitons, the Galilean expander limits the strength of the reflected signal that can be achieved with the setup. The Galilean expander also adds a considerable amount of complexity to the alignment procedure, as the laser should pass through the center of both lenses to achieve the desired result. In actuality, the alignment was not perfect, and as such, the Galilean expander added an element of noise and uncertainty to the experimental setup.

A significant issue with the single lens and the Galilean expander, which is composed of single lenses, is that of chromatic aberration, which means the focal lengths of the lenses are dependent on the wavelength of the light. The issue can be dealt with by realigning the system for a new wavelength. However, as realignment is a time-consuming process, chromatic aberration represents a substantial challenge in the case where the wavelength of the light is changed during the experimental procedure, such as for the reflection spectroscopy experiment. This issue is especially pronounced in higher temperatures, at which the linewidth of the exciton resonance is on the order of 10 nm [29].

There are at least two ways of solving this problem. The simplest solution is to acquire a cryo-compatible objective lens, which can be used in a vacuum environment. It should be noted that such lenses are expensive and typically have a long lead time for delivery. The second option is to address the placement of the sample in the vacuum chamber. One can either use a vacuum chamber with a different geometry, or redesign the sample holder, both of which to move the placement of the sample close to the window of the vacuum chamber. This would allow for the use of a commercial objective lens outside of the vacuum chamber, which would provide a sufficiently small focused beam waist without the need for a Galilean expander.

Other sample combinations

As the Ti:sapphire laser provides an optical drive with an adjustable frequency, the setup is not restricted to the use of $MoSe_2$ as the TMD. Different TMD species have exhibited static valley-Zeeman shifts of substantially different magnitudes under otherwise similar conditions [36], and as such, other TMDs may couple more strongly to magnetostatic modes.

A. Magnons in a ferromagnetic lattice

For a ferromagnet, the presence of quantized spin excitations in the lattice, also known as magnons, can be derived from its Hamiltonian. The derivation presented is known as the method of Holstein and Primakoff [47]. This appendix will take an adapted approach drawing heavily on the derivation in Ref. [15]. For simplicity, orbital angular momentum will be neglected in the following derivation, $\boldsymbol{L} = 0$, and for interactions between sites only nearest neighbor interactions will be taken into account.

The Hamiltonian of a ferromagnet can then be written as

$$\hat{\mathrm{H}} = -2\frac{J}{\hbar^2}\sum_{j,\boldsymbol{\delta}} \hat{\boldsymbol{S}}_j \cdot \hat{\boldsymbol{S}}_{j+\boldsymbol{\delta}} - \frac{g\mu_B B_0}{\hbar}\sum_j \hat{S}_{jz}, \tag{A.1}$$

where the subscript j runs over all lattice sites, and the subscript $j + \boldsymbol{\delta}$ runs over all nearest neighbor sites with $\boldsymbol{\delta}$ a nearest neighbor vector. The first term is identified as the Heisenberg Hamiltonian (2.11), whereas the second represents the Zeeman energy of the ferromagnet (2.10), with the z-axis oriented in the same direction as the applied magnetic field.

The spin product in (A.1) can be reexpressed in terms of raising and lowering operators:

$$\begin{aligned} \hat{S}_j^+ &= \hat{S}_{jx} + i\hat{S}_{jy}, \\ \hat{S}_j^- &= \hat{S}_{jx} - i\hat{S}_{jy}. \end{aligned} \tag{A.2}$$

The basis for the raising and lowering operators (A.2) is a set of states with quantum number s_{jz} for the spin in direction z located at lattice site j, denoted as $|s_{jz}\rangle$. These are the eigenstates of the operator $\hat{S}_{jz}$ with eigenvalues s_{jz} obeying:

$$\hat{S}_{jz}\,|s_{jz}\rangle = \hbar s_{jz}\,|s_{jz}\rangle\,.$$

Application of the raising and lowering operators obeys

$$\hat{S}_j^{\pm}\,|s_{jz}\rangle = \lambda_{\pm}\,|s_{jz} \pm 1\rangle \tag{A.3}$$

$$\implies \langle s_{jz}|\,\hat{S}_j^{\mp} = \langle s_{jz} \pm 1|\,\lambda_{\pm}^*, \tag{A.4}$$

where the value $\lambda_{\pm}$ is a complex number. Taking the inner product between Eqs. (A.3) and (A.4) yields:

$$\langle s_{jz}|\,\hat{S}_j^{\mp}\hat{S}_j^{\pm}\,|s_{jz}\rangle = \langle s_{jz} \pm 1|\,\lambda_{\pm}^*\lambda_{\pm}\,|s_{jz} \pm 1\rangle = |\lambda_{\pm}|^2. \tag{A.5}$$

The relation

$$S_j^2 = \frac{1}{2}(S_j^+ S_j^- + S_j^- S_j^+) + S_{jz}^2, \tag{A.6}$$

can be combined with the commutation relation

$$\left[S_j^+, S_j^-\right] = S_j^+ S_j^- - S_j^- S_j^+ = 2\hbar S_{jz}, \tag{A.7}$$

to yield:

$$S_j^- S_j^+ = S_j^2 - S_{jz}(S_{jz} + \hbar), \tag{A.8}$$
$$S_j^+ S_j^- = S_j^2 - S_{jz}(S_{jz} - \hbar). \tag{A.9}$$

Inserting these equations into Eq. (A.5) yields:

$$\begin{aligned}
+ : |\lambda_+|^2 &= \langle s_{jz}| \hat{S}_j^- \hat{S}_j^+ |s_{jz}\rangle \\
&= \langle s_{jz}| S_j^2 - S_{jz}(S_{jz} + \hbar) |s_{jz}\rangle \\
&= \hbar^2(s(s+1) - s_{jz}(s_{jz}+1)) \\
\implies \lambda_+ &= \hbar\sqrt{(s(s+1) - s_{jz}(s_{jz}+1))} \\
\implies S_{jz}^+ |s_{jz}\rangle &= \hbar\sqrt{(s(s+1) - s_{jz}(s_{jz}+1))}\, |s_{jz}+1\rangle\,. \qquad \text{(A.10)} \\
- : |\lambda_-|^2 &= \langle s_{jz}| \hat{S}_j^+ \hat{S}_j^- |s_{jz}\rangle \\
&= \langle s_{jz}| S_j^2 - S_{jz}(S_{jz} - \hbar) |s_{jz}\rangle \\
&= \hbar^2(s(s+1) - s_{jz}(s_{jz}-1)) \\
\implies \lambda_- &= \hbar\sqrt{(s(s+1) - s_{jz}(s_{jz}-1))} \\
\implies S_{jz}^- |s_{jz}\rangle &= \hbar\sqrt{(s(s+1) - s_{jz}(s_{jz}-1))}\, |s_{jz}-1\rangle\,, \qquad \text{(A.11)}
\end{aligned}$$

where the relation $S_j^2 = \hbar^2 s_j(s_j+1)$ with s_j the total spin at site j has been used.

Substituting the ladder operators Eq. (A.2) into the Hamiltonian yields:

$$\hat{\mathrm{H}} = -2\frac{J}{\hbar^2}\sum_{j,\boldsymbol{\delta}}\left[\frac{1}{2}\left(\hat{S}_j^-\hat{S}_{j+\boldsymbol{\delta}}^+ + \hat{S}_j^+\hat{S}_{j+\boldsymbol{\delta}}^-\right) + \hat{S}_{jz}\hat{S}_{j+\boldsymbol{\delta},z}\right] - \frac{g\mu_B B_0}{\hbar}\sum_j \hat{S}_{jz}. \tag{A.12}$$

Proceeding, the basis states are changed. Due to the first term of the Hamiltonian, Eq. (A.1), the ground state of the system will have all spins aligned. Due to the second term, all spins in the ground state are aligned in the direction of the applied magnetic field. Thus, ground state energy is identified as

$$E_g = -2\frac{JNZS^2}{\hbar^2} - g\frac{\mu_B B_0}{\hbar}NS, \tag{A.13}$$

where N is the number of lattice sites, and $2Z$ is the number of nearest neighbors.

As an attempt at a first excited state one can inspect what happens when a single spin in the lattice is flipped. For simplicity, we will inspect the energy of the spin flip in a one dimensional lattice, $Z = 2$, where a single spin flip yields the energy [Eq. (A.1)]

$$E_{sf} = E_g + 8\frac{JS^2}{\hbar^2} + 2g\frac{\mu_B B_0}{\hbar}S. \tag{A.14}$$

If the single spin flip is instead spread out over multiple sites, such that the sum of deviations is equal to one spin, the first term in Eq. (A.1) will yield a lower energy. This is due to the the increase in energy being quadratic in small angles between neighboring

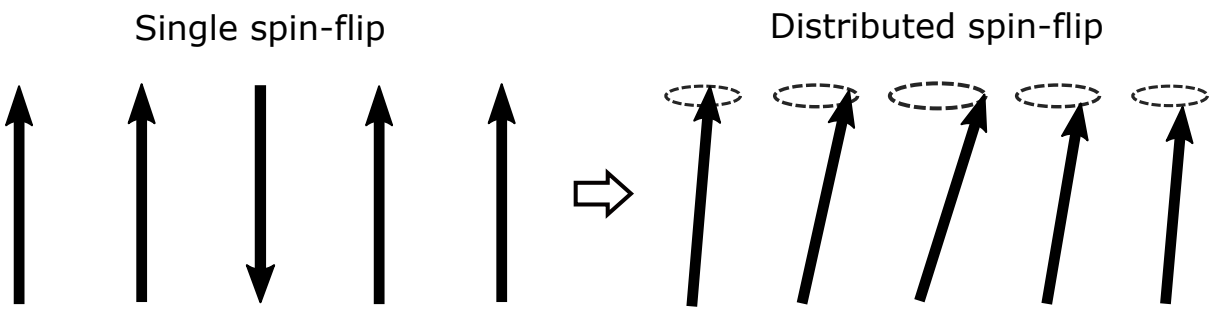

Figure A.1: Illustration of a spin-flip in a one-dimensional lattice. The deviation in the spin stemming from a magnon will generally be distributed over many lattice sites to minimize the energy, as illustrated on the right-hand side.

spins, whereas the sum of deviations is linear in this quantity[1]. Thus, the lowest energy excitations will have the spin excitation distributed over multiple sites [17].

As the energy of the state depends on the number of spin deviations from the ground state, the quantum number for the new basis is chosen to be the number of spin deviations n_j at site j. Multiple spin deviations can exist in the same location as long as the sum of deviations on any given site is less than or equal to the total spin, and as such the spin deviations are not subject to the Pauli exclusion principle; rather, they behave as bosons. The states can then be expressed as harmonic oscillator eigenstates $|n_j\rangle$. The corresponding creation and annihilation operators $\hat{a}_j, \hat{a}_j^\dagger$ create and annihilate a quasiparticle known as the *magnon* which corresponds to a single spin being flipped in the lattice, in general spread out over multiple lattice sites.

The operators in the new basis are defined by the following equations:

$$[\hat{a}_i, \hat{a}_j^\dagger] = \delta_{ij}, \tag{A.15}$$
$$[\hat{a}_i, \hat{a}_j] = [\hat{a}_i^\dagger, \hat{a}_j^\dagger] = 0, \tag{A.16}$$
$$\hat{a}_j |n_j\rangle = \sqrt{n_j}\, |n_j - 1\rangle\,, \tag{A.17}$$
$$\hat{a}_j^\dagger |n_j\rangle = \sqrt{n_j + 1}\, |n_j + 1\rangle\,, \tag{A.18}$$
$$\hat{a}_j^\dagger \hat{a}_j |n_j\rangle = n_j |n_j\rangle\,. \tag{A.19}$$

By noting that both the old and new operators act on the spin in the z direction at site j, expressed as s_{jz} in the original basis and $s - n_j$ in the new basis, the transformation

[1]For small angles θ, $\sin\theta \approx \theta$, $\cos\theta \approx 1 - \theta^2$. $\Delta E \propto -\cos\theta$, $\sum_i S_{iz} \propto \sin\theta$.

from the original basis to the new can be expressed as

$$\begin{aligned}
\hat{S}_{jz}\,|n_j\rangle &= \hbar(s-n_j)\,|n_j\rangle \\
&= \hbar(s-\hat{a}_j^\dagger\hat{a}_j)\,|n_j\rangle \qquad \text{(A.20)}\\
\hat{S}_j^+\,|n_j\rangle &= \hbar(s(s+1)-(s-n_j)(s-n_j+1))^{1/2}\,|n_j-1\rangle \\
&= \hbar(2sn_j-n_j^2+n_j)^{1/2}\,|n_j-1\rangle \\
&= \hbar\sqrt{2s}\Big(1-\frac{n_j-1}{2s}\Big)^{1/2}\sqrt{n_j}\,|n_j-1\rangle \\
\implies \hat{S}_j^+ &= \hbar\sqrt{2s}\Big(1-\frac{\hat{a}_j^\dagger\hat{a}_j}{2s}\Big)\hat{a}_j, \qquad \text{(A.21)}\\
\hat{S}_j^-\,|n_j\rangle &= \hbar(s(s+1)-(s-n_j)(s-n_j-1))^{1/2}\,|n_j+1\rangle\,, \\
&= \hbar(2s(1+n_j)-n_j^(1+-n_j))^{1/2}\,|n_j+1\rangle \\
&= \hbar\sqrt{2s}\sqrt{n_j+1}\Big(1-\frac{n_j}{2s}\Big)^{1/2}\,|n_j+1\rangle \\
\implies \hat{S}_j^- &= \hbar\sqrt{2s}\hat{a}_j^\dagger\Big(1-\frac{\hat{a}_j^\dagger\hat{a}_j}{2s}\Big), \qquad \text{(A.22)}
\end{aligned}$$

Where the relations in Eqs. (A.17) – (A.19) were used. The equations (A.21) and (A.22) are known as the *Holstein-Primakoff transformation*.

In order for the Hamiltonian to be diagonalizable, the operators in the new basis are linearized by employing the low temperature approximation. In this approximation the number of exciations is assumed to be small, $\hat{a}_j^\dagger\hat{a}_j << 2s$, such that the square root term in Eqs. (A.21) and (A.22) can be approximated as

$$\Big(1-\frac{\hat{a}_j^\dagger\hat{a}_j}{2s}\Big)^{1/2}\approx 1 \qquad \text{(A.23)}$$

The spin ladder operators can then be expressed as

$$\hat{S}_j^+ = \hbar\sqrt{2s}\hat{a}_j, \qquad \text{(A.24)}$$

$$\hat{S}_j^- = \hbar\sqrt{2s}\hat{a}_j^\dagger. \qquad \text{(A.25)}$$

Substituting Eqs. (A.20), (A.24) and (A.25) into the Hamiltonian and keeping terms to second order in creation/annihilation operators yields [Eq. (A.12)]:

$$\begin{aligned}
\hat{\mathrm{H}} =& -2Js\sum_{j,\boldsymbol{\delta}}[\hat{a}_j^\dagger\hat{a}_{j+\boldsymbol{\delta}}+\hat{a}_j\hat{a}_{j+\boldsymbol{\delta}}^\dagger-\hat{a}_j^\dagger\hat{a}_j-\hat{a}_{j+\boldsymbol{\delta}}^\dagger\hat{a}_{j+\boldsymbol{\delta}}+s]-g\mu_B B_0\sum_j(s-\hat{a}_j^\dagger\hat{a}_j) \\
=& -2JNZs^2-g\mu_B B_0 Ns+\hat{\mathrm{H}}', \\
\hat{\mathrm{H}}' =& -2Js\sum_{j,\boldsymbol{\delta}}[\hat{a}_j^\dagger\hat{a}_{j+\boldsymbol{\delta}}+\hat{a}_j\hat{a}_{j+\boldsymbol{\delta}}^\dagger-\hat{a}_j^\dagger\hat{a}_j-\hat{a}_{j+\boldsymbol{\delta}}^\dagger\hat{a}_{j+\boldsymbol{\delta}}]+g\mu_B B_0\sum_j(\hat{a}_j^\dagger\hat{a}_j) \qquad \text{(A.26)}
\end{aligned}$$

To diagonalize the Hamiltonian, the Fourier transformed operators $\hat{a}_{\boldsymbol{k}}, \hat{a}_{\boldsymbol{k}}^\dagger$ are introduced:

$$\hat{a}_{\boldsymbol{k}}^\dagger = \frac{1}{\sqrt{N}}\sum_j e^{i\boldsymbol{k}\cdot\boldsymbol{r}_j}\hat{a}_j^\dagger, \qquad \text{(A.27)}$$

$$\hat{a}_{\boldsymbol{k}} = \frac{1}{\sqrt{N}}\sum_j e^{-i\boldsymbol{k}\cdot\boldsymbol{r}_j}\hat{a}_j^\dagger, \qquad \text{(A.28)}$$

where $\boldsymbol{r}_j$ is the position vector of lattice site j. These new operators create and annihilate magnons with wavenumber $\boldsymbol{k}$ and have the commutation relation

$$[\hat{a}_{\boldsymbol{k}}, \hat{a}^\dagger_{\boldsymbol{k'}}] = \frac{1}{N}\sum_j e^{i(\boldsymbol{k'}-\boldsymbol{k})\boldsymbol{r}_j} = \delta_{\boldsymbol{k'},\boldsymbol{k}}, \tag{A.29}$$

where $\delta_{\boldsymbol{k'},\boldsymbol{k}}$ is the Kronecker delta. The inverse transform is:

$$\hat{a}^\dagger_j = \frac{1}{\sqrt{N}}\sum_{\boldsymbol{k}} e^{-i\boldsymbol{k}\cdot\boldsymbol{r}_j}\hat{a}^\dagger_{\boldsymbol{k}}, \tag{A.30}$$

$$\hat{a}_{\boldsymbol{j}} = \frac{1}{\sqrt{N}}\sum_{\boldsymbol{k}} e^{i\boldsymbol{k}\cdot\boldsymbol{r}_j}\hat{a}^\dagger_{\boldsymbol{k}}. \tag{A.31}$$

Substituting into Eq. (A.26) yields:

$$\begin{aligned}
\hat{\mathrm{H}}' = & -\frac{2Js}{N}\sum_{j\boldsymbol{\delta}\boldsymbol{k}\boldsymbol{k'}}\Big(e^{-i(\boldsymbol{k}-\boldsymbol{k'})\cdot\boldsymbol{r}_j}e^{i\boldsymbol{k'}\cdot\boldsymbol{\delta}}\hat{a}^\dagger_{\boldsymbol{k}}\hat{a}_{\boldsymbol{k'}} + e^{i(\boldsymbol{k}-\boldsymbol{k'})\cdot\boldsymbol{r}_j}e^{-i\boldsymbol{k'}\cdot\boldsymbol{\delta}}\hat{a}_{\boldsymbol{k}}\hat{a}^\dagger_{\boldsymbol{k'}} \\
& - e^{-i(\boldsymbol{k}-\boldsymbol{k'})\cdot\boldsymbol{r}_j}\hat{a}^\dagger_{\boldsymbol{k}}\hat{a}_{\boldsymbol{k'}} - e^{-i(\boldsymbol{k}-\boldsymbol{k'})\cdot(\boldsymbol{r}_j+\boldsymbol{\delta})}\hat{a}^\dagger_{\boldsymbol{k}}\hat{a}_{\boldsymbol{k'}} \\
& + \frac{g\mu_B B_0}{N}\sum_{j\boldsymbol{k}\boldsymbol{k'}} e^{-i(\boldsymbol{k}-\boldsymbol{k'})\cdot\boldsymbol{r}_j}\hat{a}^\dagger_{\boldsymbol{k}}\hat{a}_{\boldsymbol{k'}}\Big) \\
= & -2Js\sum_{\boldsymbol{\delta}\boldsymbol{k}}\Big(e^{i\boldsymbol{\delta}\cdot\boldsymbol{k}}\hat{a}^\dagger_{\boldsymbol{k}}\hat{a}_{\boldsymbol{k}} + e^{-i\boldsymbol{\delta}\cdot\boldsymbol{k}}(\hat{a}^\dagger_{\boldsymbol{k}}\hat{a}_{\boldsymbol{k}}+1) - 2\hat{a}^\dagger_{\boldsymbol{k}}\hat{a}_{\boldsymbol{k}}\Big) + g\mu_B B_0\sum_{\boldsymbol{k}}\hat{a}^\dagger_{\boldsymbol{k}}\hat{a}_{\boldsymbol{k}} \\
= & -2Js\sum_{\boldsymbol{k}}\Big[\hat{a}^\dagger_{\boldsymbol{k}}\hat{a}_{\boldsymbol{k}}(\gamma_{\boldsymbol{k}}+\gamma_{-\boldsymbol{k}}-2)\Big] - 2Js\underbrace{\sum_{\boldsymbol{\delta}\boldsymbol{k}} e^{-i\boldsymbol{\delta}\cdot\boldsymbol{k}}}_{=0} + g\mu_B B_0\sum_{\boldsymbol{k}}\hat{a}^\dagger_{\boldsymbol{k}}\hat{a}_{\boldsymbol{k}} \\
= & \sum_{\boldsymbol{k}}\Big(2JsZ(2-\gamma_{\boldsymbol{k}}-\gamma_{-\boldsymbol{k}}) + g\mu_B B_0\Big)\hat{a}^\dagger_{\boldsymbol{k}}\hat{a}_{\boldsymbol{k}},
\end{aligned} \tag{A.32}$$

where the quantity $\gamma_{\boldsymbol{k}}$ has been defined as $\gamma_{\boldsymbol{k}} \equiv \sum_{\boldsymbol{\delta}} e^{i\boldsymbol{\delta}\cdot\boldsymbol{k}}$, which depends on the geometry of the lattice.

By defining the dispersion relation

$$\hbar\omega_k = 2JsZ(2-\gamma_{\boldsymbol{k}}-\gamma_{-\boldsymbol{k}}) + g\mu_B B_0, \tag{A.33}$$

the magnons can be described using the bosonic Hamiltonian

$$\hat{\mathrm{H}}_{\mathrm{magnon}} = \sum_k \hat{n}_{\boldsymbol{k}}\hbar\omega_{\boldsymbol{k}}. \tag{A.34}$$

As the Hamiltonian for magnons is diagonalizable in k-space rather than position space, the configuration of spin deviations will generally move around the lattice, giving rise to the name *spin wave*.

B. Magnetization of a ferromagnet

In this appendix we will derive the dynamics of the magnetization of a ferromagnet in a magnetic field with a small time-dependent component, drawing on a similar derivation in Chapter 1.2-1.4 in [16].

The magnetization of a material is defined as the total magnetic moment per unit volume of a magnet:

$$\boldsymbol{M} = \frac{1}{V}\sum_i \boldsymbol{\mu}_i, \tag{B.1}$$

where V is the volume of the material, $\sum_i$ sums over all lattice sites i, and μ_i is the magnetic moment at site i.

The equation of motion for a magnetic moment can be obtained by substituting eq. (2.5) into eq. (2.7), which can then be summed over all sites to obtain an equation of motion for the magnetization:

$$\frac{\mathrm{d}\boldsymbol{M}}{\mathrm{d}t} = -\gamma\mu_0 \boldsymbol{M} \times \boldsymbol{H}. \tag{B.2}$$

We consider the time-dependent component of the magnetic field as a perturbation:

$$\boldsymbol{H}(t) = \boldsymbol{H}_0 + \boldsymbol{h}(t), \tag{B.3}$$

where $\boldsymbol{h}(t)$ is a field with harmonic time dependence that is small compared to the static field $\boldsymbol{H}_0$.

The magnetization can be expressed in a similar manner;

$$\boldsymbol{M}(t) = \boldsymbol{M}_0 + \boldsymbol{m}(t), \tag{B.4}$$

where $\boldsymbol{m}(t)$ is a harmonically time-dependent magnetization, which we assume to be small compared to the mean magnetization $\boldsymbol{M}_0$.

Inserting into the equation of motion (B.2) yields:

$$\frac{\mathrm{d}}{\mathrm{d}t}(\boldsymbol{M_0} + \boldsymbol{m}) = -\gamma\mu_0(\boldsymbol{M_0} + \boldsymbol{m}) \times (\boldsymbol{H}_0 + \boldsymbol{h}). \tag{B.5}$$

This expression can be split by order in the small parameters $\boldsymbol{h}$ and $\boldsymbol{m}$, and solved order by order.

The zeroth-order equation is:

$$\boldsymbol{H}_0 \times \boldsymbol{M}_0 = 0. \tag{B.6}$$

This means that the direction of equilibrium magnetization is parallel to the static field H_0.

The first-order equation is:

$$\frac{\mathrm{d}\boldsymbol{m}}{\mathrm{d}t} + \gamma\mu_0 \boldsymbol{m} \times \boldsymbol{H}_0 = -\gamma\mu_0 \boldsymbol{M}_0 \times \boldsymbol{h} \tag{B.7}$$

Neglecting the second order equation, the equation of motion has been linearized in the parameters $\boldsymbol{h}$ and $\boldsymbol{m}$.

Due to the harmonic time dependence $\boldsymbol{m}$ and $\boldsymbol{h}$ can be written as the real parts of the complex vectors rotating in the complex plane:

$$\boldsymbol{m}^{\boldsymbol{C}} = \tilde{\boldsymbol{m}} e^{-i\omega t}, \tag{B.8}$$

$$\boldsymbol{h}^{\boldsymbol{C}} = \tilde{\boldsymbol{h}} e^{-i\omega t}, \tag{B.9}$$

where ω is the frequency of the time dependent oscillation, and $\tilde{\boldsymbol{m}}, \tilde{\boldsymbol{h}}$ are complex amplitudes of the oscillations.

Substituting into eq. (B.7) yields:

$$-i\omega\tilde{\boldsymbol{m}} + \gamma\mu_0 \tilde{\boldsymbol{m}} \times \boldsymbol{H}_0 = -\gamma\mu_0 \boldsymbol{M}_0 \times \tilde{\boldsymbol{h}}. \tag{B.10}$$

By aligning the z-axis so that $\boldsymbol{H}_0 = H_0 \boldsymbol{e}_z$ and $\boldsymbol{M}_0 = M_0 \boldsymbol{e}_z$ with $\boldsymbol{e}_z$ the unit vector in the direction z, eq. (B.10) can be expressed in terms of Cartesian components:

$$-i\omega\tilde{m}_x + \gamma\mu_0 H_0 \tilde{m}_y = \gamma\mu_0 M_0 \tilde{h}_y, \tag{B.11}$$

$$-i\omega\tilde{m}_y - \gamma\mu_0 H_0 \tilde{m}_x = -\gamma\mu_0 M_0 \tilde{h}_x, \tag{B.12}$$

$$-i\omega\tilde{m}_z = 0. \tag{B.13}$$

This can be reexpressed in tensor notation:

$$\tilde{\boldsymbol{m}} = \bar{\boldsymbol{\chi}} \tilde{\boldsymbol{h}}, \tag{B.14}$$

$$\bar{\boldsymbol{\chi}} \equiv \begin{pmatrix} \chi & -i\chi_a & 0 \\ i\chi_a & \chi & 0 \\ 0 & 0 & 0 \end{pmatrix}, \tag{B.15}$$

$$\chi \equiv \frac{(\gamma\mu_0)^2 M_0 H_0}{(\gamma\mu_0 H_0)^2 - \omega^2}, \quad \chi_a \equiv \frac{\gamma\mu_0 M_0 \omega}{(\gamma\mu_0 H_0)^2 - \omega^2}, \tag{B.16}$$

where $\bar{\boldsymbol{\chi}}$ is known as the *susceptibility tensor*.

Equation (B.2) does not contain any damping terms, even though it is energetically favorable for the magnetization $\boldsymbol{M}$ to align with the magnetic field $\boldsymbol{H}$. In actuality, there will be some form of damping in the system, and if the damping is relatively small, there are a number of ways of phenomenologically adding damping to the equation of motion [16].

One method, proposed by T. Gilbert [48][1], modifies Eq. (B.2) as

$$\frac{\mathrm{d}\boldsymbol{M}}{\mathrm{d}t} = -\gamma\mu_0 \boldsymbol{M} \times \boldsymbol{H} + \frac{\alpha}{M} \boldsymbol{M} \times \frac{\partial \boldsymbol{M}}{\partial \mathrm{t}}, \tag{B.17}$$

where α is a small dimensionless parameter that characterizes the rate of dissipation.

[1] It was originally proposed in an unpublished paper in 1955

Inserting eqs. (B.3) and (B.4) into the damped equation of motion (B.17) yields:

$$\begin{aligned}\frac{\mathrm{d}}{\mathrm{d}t}\Big(\boldsymbol{M}_0+\boldsymbol{m}(t)\Big) = &-\gamma\mu_0\Big(\boldsymbol{M}_0+\boldsymbol{m}(t)\Big)\times\Big(\boldsymbol{H}_0+\boldsymbol{h}(t)\Big)\\ &+\frac{\alpha}{M_0}\Big(\boldsymbol{M}_0+\boldsymbol{m}(t)\Big)\times\frac{\partial}{\partial\mathrm{t}}\Big(\boldsymbol{M}_0+\boldsymbol{m}(t)\Big),\end{aligned} \tag{B.18}$$

where the amplitude of the magnetization in the denominator of the dissipative term has been replaced with the average amplitude of the magnetization:

$$\langle M\rangle = M_0+\underbrace{\langle m(t)\rangle}_{=0}.$$

Equation (B.18) can be separated by order in the small parameters $\boldsymbol{h}$ and $\boldsymbol{m}$, and solved order by order. The zeroth order equation is:

$$\boldsymbol{H}_0\times\boldsymbol{M}_0=0. \tag{B.19}$$

This means that the direction of the equilibrium magnetization M_0 is parallel to the static part of the field H_0. The first order equation is

$$\begin{aligned}\frac{\mathrm{d}\boldsymbol{m}(t)}{\mathrm{d}t} = &-\gamma\mu_0\boldsymbol{M}_0\times\boldsymbol{h}(t)-\gamma\mu_0\boldsymbol{m}(t)\times\boldsymbol{H}_0\\ &+\frac{\alpha}{M_0}\boldsymbol{M}_0\times\frac{\partial\boldsymbol{m}(t)}{\partial\mathrm{t}}\\ \Longrightarrow\ -\gamma\mu_0\boldsymbol{M}_0\times\tilde{\boldsymbol{h}} = &-i\omega\tilde{\boldsymbol{m}}+\gamma\mu_0\tilde{\boldsymbol{m}}\times\boldsymbol{H}_0+i\omega\frac{\alpha}{M_0}\boldsymbol{M}_0\times\tilde{\boldsymbol{m}}\end{aligned} \tag{B.20}$$

Neglecting the second-order equation, the equation of motion has been linearized in the parameters $\boldsymbol{h}$ and $\boldsymbol{m}$. Equivalent linearized equations of motion can be obtained from the lossless case by transforming the amplitude H_0 as [Eq.(B.10)]:

$$\gamma\mu_0H_0\to\gamma\mu_0H_0-i\alpha\omega. \tag{B.21}$$

The susceptibility tensor with losses can then be found by making use of the relation Eq.(B.21) with Eq.(B.15):

$$\tilde{\boldsymbol{m}}=\bar{\boldsymbol{\chi}}\tilde{\boldsymbol{h}}, \tag{B.22}$$

$$\bar{\boldsymbol{\chi}}\equiv\begin{pmatrix}\chi & -i\chi_a & 0\\ i\chi_a & \chi & 0\\ 0 & 0 & 0\end{pmatrix}, \tag{B.23}$$

$$\chi\equiv\chi'+i\chi'',\ \chi_a\equiv\chi_a'+i\chi_a''. \tag{B.24}$$

using the following definitions:

$$\begin{aligned}
\omega_H &\equiv \gamma\mu_0 H_0, \\
\omega_M &\equiv \gamma\mu_0 M_0, \\
\chi' &= \frac{1}{D}\omega_H\omega_M\Big[\omega_H^2 - (1-\alpha^2)\omega^2\Big], \\
\chi'' &= \frac{1}{D}\alpha\omega_M\omega\Big[\omega_H^2 + (1+\alpha^2)\omega^2\Big], \\
\chi_a' &= \frac{1}{D}\omega_M\omega\Big[\omega_H^2 - (1+\alpha^2)\omega^2\Big], \\
\chi_a'' &= \frac{2}{D}\alpha\omega_m\omega_h\omega^2, \\
D &= \Big[\omega_H^2 - (1+\alpha^2)\omega^2\Big]^2 + 4\alpha^2\omega^2\omega_H^2,
\end{aligned} \tag{B.25}$$

C. Semiconductor–Light Hamiltonian and Bloch equations

In this appendix, the quantum mechanical Hamiltonian for a semiconductor interacting with light is presented, from which a set of coupled differential equations characterizing the dynamics of the system, known as the *semiconductor Bloch equations*, is derived. The section follows an adapted approach from chapter 10 of Ref. [22]. For the semiconductor it will be assumed that the dynamics can be described using a two-band model with single valence and conduction bands. The light will be assumed to be in a coherent state, such that it can be treated classically.

Hamiltonian of the semiconductor–light system

The light-semiconductor interaction is treated using perturbation theory, splitting the Hamiltonian into two parts:

$$\hat{\mathrm{H}}(t) = \hat{\mathrm{H}}_0 + \hat{V}(t), \tag{C.1}$$

where H_0 is the unperturbed Hamiltonian of the semiconductor without light present, and $\hat{V}(t)$ represents the interaction energy of the light-semiconductor interaction. The unperturbed Hamiltonian will initially be written in terms of creation and annihilation operators for conduction band electrons and valence band holes. The conduction band electron is a quasiparticle representing an electron confined to the conduction band. The valence band hole, on the other hand, is a quasiparticle representing the absence of a valence band electron, presumably as it has been excited to the conduction band, which has the opposite momentum, spin and charge, and same effective mass as the corresponding valence band electron. Formally, the annihilation and creation operators of the valence band hole are defined as

$$\begin{aligned} \hat{c}_{\mathrm{h},\boldsymbol{k}} &= \hat{c}^{\dagger}_{\mathrm{v},-\boldsymbol{k}}, \\ \hat{c}^{\dagger}_{\mathrm{h},\boldsymbol{k}} &= \hat{c}_{\mathrm{v},-\boldsymbol{k}}, \end{aligned} \tag{C.2}$$

where subscript h (v) denotes a valence band hole (electron), and k is the quantum number of the particle, which is assumed to correspond to the wave vector and spin of the particle. It is assumed that the conduction band electron and valence band hole, hereafter referred to simply as electron and hole, follow the anticommutation relations

$$\{\hat{c}_{\mathrm{b},\boldsymbol{k}}, \hat{c}^{\dagger}_{\mathrm{b'},\boldsymbol{k'}}\} = \delta_{\mathrm{bb'}}\delta_{\boldsymbol{k}\boldsymbol{k'}} \tag{C.3}$$

$$\{\hat{c}_{\mathrm{b},\boldsymbol{k}}, \hat{c}_{\mathrm{b'},\boldsymbol{k'}}\} = \{\hat{c}^{\dagger}_{\mathrm{b},\boldsymbol{k}}, \hat{c}^{\dagger}_{\mathrm{b'},\boldsymbol{k'}}\} = 0 \tag{C.4}$$

where the band index b = c (b = h) denotes an electron (hole) operator.

Using the creation and annihilation operators for the electron and the hole, the unperturbed Hamiltonian can be written as [22]

$$\begin{aligned}\hat{\mathrm{H}}_0 = &\sum_{\boldsymbol{k}} \left(\varepsilon_{\mathrm{c},\boldsymbol{k}} \hat{c}^\dagger_{\mathrm{c},\boldsymbol{k}} \hat{c}_{\mathrm{c},\boldsymbol{k}} + \varepsilon_{\mathrm{h},\boldsymbol{k}} \hat{c}^\dagger_{\mathrm{h},\boldsymbol{k}} \hat{c}_{\mathrm{h},\boldsymbol{k}}\right) \\ &+ \frac{1}{2} \sum_{\boldsymbol{k},\boldsymbol{k'}\boldsymbol{q}\neq 0} V(\boldsymbol{q}) \Big(\hat{c}^\dagger_{\mathrm{c},\boldsymbol{k}+\boldsymbol{q}} \hat{c}^\dagger_{\mathrm{c},\boldsymbol{k'}-\boldsymbol{q}} \hat{c}_{\mathrm{c},\boldsymbol{k'}} \hat{c}_{\mathrm{c},\boldsymbol{k}} \\ &+ \hat{c}_{\mathrm{h},\boldsymbol{k}+\boldsymbol{q}} \hat{c}_{\mathrm{h},\boldsymbol{k'}-\boldsymbol{q}} \hat{c}^\dagger_{\mathrm{h},\boldsymbol{k'}} \hat{c}^\dagger_{\mathrm{h},\boldsymbol{k}} \\ &+ 2\hat{c}^\dagger_{\mathrm{c},\boldsymbol{k}+\boldsymbol{q}} \hat{c}_{\mathrm{h},\boldsymbol{k'}-\boldsymbol{q}} \hat{c}^\dagger_{\mathrm{v},\boldsymbol{k'}} \hat{c}_{\mathrm{c},\boldsymbol{k}} \Big).\end{aligned} \tag{C.5}$$

where $\varepsilon_{\mathrm{c},\boldsymbol{k}}$ ($\varepsilon_{\mathrm{h},\boldsymbol{k}}$) is the energy of an electron (hole) with quantum number $\boldsymbol{k}$, and $V(\boldsymbol{q})$ is the Fourier transform of the Coulomb interaction between the particles.

The interaction between the semiconductor system and light is treated in the *long wavelength approximation*(LWA) and *dipole approximation*. In the LWA the electric field is treated as if it is the same for all interacting particles, i. e. spatial variations are not taken into account. This is valid as long as the relevant length scales are small compared to the wavelength of the light. For light in the optical regime, the wavelength in a semiconductor is several orders of magnitudes larger than the lattice constant, which is the relevant length scale of the semiconductor. The dipole approximation treats the light as if it is classical and approximates the interaction energy as the interaction between the dipole moments in the system and the electric field component of the light, which typically dominates the optical response of a material [14]. This approximation neglects transitions where a valence band electron is excited into a conduction band state with the opposite spin, as such transitions are dependent on higher-order interactions. Thus excitonic modes stemming from such transitions, denoted as *dark excitons*, are neglected due to their low optical response.Writing the interaction energy as the shift in dipole energy due to the electric field of the light yields the interaction Hamiltonian [22]:

$$\hat{\mathrm{H}}_{\mathrm{int}} \approx \sum_{\boldsymbol{k}} \hbar (g_{\omega_d} \hat{c}^\dagger_{\mathrm{c},\boldsymbol{k}} \hat{c}^\dagger_{\mathrm{h},-\boldsymbol{k}} e^{-i\omega_d t} + \mathrm{h.c.}), \tag{C.6}$$

where ω_d is the frequency of the classical light, denoted as the optical drive, g_{ω_d} is the coupling strength of the light and electrons, which is proportional to the electric field strength of the light and dipole moment between the electrons and the holes, and h. c. denotes Hermitian conjugate. From the interaction Hamiltonian, one can surmise that the interaction between semiconductor and light results in the creation and annihilation of electron-hole pairs, which happens due to the absorption and emission of light.

The total Hamiltonian of the semiconductor–light system can then be written as

$$\begin{aligned}\hat{\mathrm{H}} &= \hat{\mathrm{H}}_0 + \hat{\mathrm{H}}_{\mathrm{int}} \\ &= \sum_{\boldsymbol{k}} \left(\varepsilon_{\mathrm{c},\boldsymbol{k}} \hat{c}^\dagger_{\mathrm{c},\boldsymbol{k}} \hat{c}_{\mathrm{c},\boldsymbol{k}} + \varepsilon_{\mathrm{h},\boldsymbol{k}} \hat{c}^\dagger_{\mathrm{h},\boldsymbol{k}} \hat{c}_{\mathrm{h},\boldsymbol{k}}\right) \\ &\quad + \frac{1}{2} \sum_{\boldsymbol{k},\boldsymbol{k'}\boldsymbol{q}\neq 0} V(\boldsymbol{q}) \Big(\hat{c}^\dagger_{\mathrm{c},\boldsymbol{k}+\boldsymbol{q}} \hat{c}^\dagger_{\mathrm{c},\boldsymbol{k'}-\boldsymbol{q}} \hat{c}_{\mathrm{c},\boldsymbol{k'}} \hat{c}_{\mathrm{c},\boldsymbol{k}} \\ &\quad + \hat{c}_{\mathrm{h},\boldsymbol{k}+\boldsymbol{q}} \hat{c}_{\mathrm{h},\boldsymbol{k'}-\boldsymbol{q}} \hat{c}^\dagger_{\mathrm{h},\boldsymbol{k'}} \hat{c}^\dagger_{\mathrm{h},\boldsymbol{k}} \\ &\quad + 2\hat{c}^\dagger_{\mathrm{c},\boldsymbol{k}+\boldsymbol{q}} \hat{c}_{\mathrm{h},\boldsymbol{k'}-\boldsymbol{q}} \hat{c}^\dagger_{\mathrm{v},\boldsymbol{k'}} \hat{c}_{\mathrm{c},\boldsymbol{k}} \Big) \\ &\quad + \sum_{\boldsymbol{k}} \hbar (g_{\omega_d} \hat{c}^\dagger_{\mathrm{c},\boldsymbol{k}} \hat{c}^\dagger_{\mathrm{h},-\boldsymbol{k}} e^{-i\omega_d t} + \mathrm{h.c.}).\end{aligned} \tag{C.7}$$

Semiconductor Bloch equations

The dynamics of the semiconductor system can be explained by the dynamics of the conduction band electrons and the valence band holes. The interaction with light results in the creation and annihilation of electron–hole pairs, and as such the dynamics of the total semiconductor–light system can be formulated as the coupled dynamics of the electron and hole populations and the electron–hole pairs. One such approach is the semiconductor Bloch equations, which is a set of differential equations for the expectation values of the electron and hole number operators, $n_{\mathrm{b},\boldsymbol{k}} \equiv \langle \hat{c}^\dagger_{\mathrm{b},\boldsymbol{k}} \hat{c}_{\mathrm{b},\boldsymbol{k}} \rangle$, and the expectation value of the pair operator $P_{\mathrm{ch},\boldsymbol{k}} \equiv \langle \hat{c}_{\mathrm{h},-\boldsymbol{k}} \hat{c}_{\mathrm{c},\boldsymbol{k}} \rangle$.

The semiconductor Bloch equations are obtained by taking the expectation value of the Heisenberg equations of motion of the corresponding operators. For the pair operator this yields [Eq. (2.2)]

$$\begin{aligned}\frac{\mathrm{d}\hat{P}_{\mathrm{ch},\boldsymbol{k}}}{\mathrm{d}t} = &-\frac{i}{\hbar}(\varepsilon_{\mathrm{c},\boldsymbol{k}} + \varepsilon_{\mathrm{h},\boldsymbol{k}})\hat{P}_{\mathrm{ch},\boldsymbol{k}} + i g_{\omega_d}\Big[1 - \hat{c}^\dagger_{\mathrm{h},-\boldsymbol{k}}\hat{c}_{\mathrm{h},-\boldsymbol{k}} - \hat{c}^\dagger_{\mathrm{c},\boldsymbol{k}}\hat{c}_{\mathrm{c},\boldsymbol{k}}\Big] \\ &+ \frac{i}{\hbar}\sum_{\boldsymbol{k}',\boldsymbol{q}\neq 0} V(\boldsymbol{q})\Big(\delta_{-\boldsymbol{k},\boldsymbol{k}'-\boldsymbol{q}} P_{\mathrm{ch},\boldsymbol{k}-\boldsymbol{q}} + \hat{c}^\dagger_{\mathrm{h},\boldsymbol{k}'-\boldsymbol{q}}\hat{c}_{\mathrm{h},\boldsymbol{k}'}\hat{c}_{\mathrm{h},-\boldsymbol{k}}\hat{c}_{\mathrm{c},\boldsymbol{k}-\boldsymbol{q}} \\ &+ \hat{c}^\dagger_{\mathrm{c},\boldsymbol{k}'+\boldsymbol{q}}\hat{c}_{\mathrm{c},\boldsymbol{k}'}\hat{c}_{\mathrm{h},-\boldsymbol{k}+\boldsymbol{q}}\hat{c}_{\mathrm{c},\boldsymbol{k}} + \hat{c}^\dagger_{\mathrm{c},\boldsymbol{k}'-\boldsymbol{q}}\hat{c}_{\mathrm{c},\boldsymbol{k}'}\hat{c}_{\mathrm{c},\boldsymbol{k}-\boldsymbol{q}}\hat{c}_{\mathrm{h},-\boldsymbol{k}} \\ &+ \hat{c}^\dagger_{\mathrm{h},\boldsymbol{k}'-\boldsymbol{q}}\hat{c}_{\mathrm{h},-\boldsymbol{k}-\boldsymbol{q}}\hat{c}_{\mathrm{h},\boldsymbol{k}'}\hat{c}_{\mathrm{c},\boldsymbol{k}}\Big).\end{aligned} \tag{C.8}$$

Taking the expectation value of the operators, there is an issue with the four-operator terms in the final sum; the four-operator term expectation values are dependent on six-operator expectation values, which are dependent on eight-operator expectation values etc. [23]. In order to obtain a closed set of equations that can be solved, the *random phase approximation* is employed. This approximation assumes, much like the RWA, that a subset of the operators has a dominant time dependence, meaning the four-operator terms can be approximately factorized in terms of the dominant subset by inserting delta functions, essentially picking out the dominant terms and neglecting all others. The resultant expectation values are then further factorized in terms of two-operator expectation values, which in this case yields [23]:

$$\begin{aligned}\frac{dP_{\mathrm{ch},\boldsymbol{k}}}{\mathrm{d}t} \approx &-\frac{i}{\hbar}\Big[\varepsilon_{\mathrm{c},\boldsymbol{k}} + \varepsilon_{\mathrm{h},\boldsymbol{k}} - \sum_{\boldsymbol{q}\neq 0} V(\boldsymbol{q})(n_{\mathrm{c},\boldsymbol{k}-\boldsymbol{q}} + n_{\mathrm{h},\boldsymbol{k}-\boldsymbol{q}})\Big]P_{\mathrm{ch},\boldsymbol{k}} \\ &+ \Big(i g_{\omega_d} + \frac{i}{\hbar}\sum_{\boldsymbol{q}\neq 0} V(\boldsymbol{q}) P_{\mathrm{ch},\boldsymbol{k}-\boldsymbol{q}}\Big)[1 - n_{\mathrm{c},\boldsymbol{k}} - n_{\mathrm{h},\boldsymbol{k}}],\end{aligned} \tag{C.9}$$

where $P_{\mathrm{ch},\boldsymbol{k}} \equiv \langle \hat{P}_{\mathrm{ch},\boldsymbol{k}} \rangle$ is the expectation value of the pair operator, and $n_{\mathrm{c},\boldsymbol{k}} \equiv \langle \hat{c}^\dagger_{\mathrm{c},\boldsymbol{k}}\hat{c}_{\mathrm{c},\boldsymbol{k}} \rangle$ ($n_{\mathrm{h},\boldsymbol{k}} \equiv \langle \hat{c}^\dagger_{\mathrm{h},\boldsymbol{k}}\hat{c}_{\mathrm{h},\boldsymbol{k}} \rangle$) is the expectation value of the number conduction-band electrons (holes).

In the *low excitation limit*, also known as the *ulralow density regime*, where the number of excited conduction-band electrons and valence-band holes are small enough that they can be neglected in the equations of motion of the system, $n_{\mathrm{c},\boldsymbol{k}} = n_{\mathrm{h},\boldsymbol{k}} = 0$. The equation of motion then reads:

$$\frac{\mathrm{d}P_{\mathrm{ch},\boldsymbol{k}}}{\mathrm{d}t} = -\frac{i}{\hbar}\Big(E_g + \frac{\hbar^2 k^2}{2m^*_r}P_{\mathrm{ch},\boldsymbol{k}}\Big) + \frac{i}{\hbar}\Big(\hbar g_{\omega_d} + V(\boldsymbol{q})P_{\mathrm{ch},\boldsymbol{k}-\boldsymbol{q}}\Big), \tag{C.10}$$

where E_g is the band gap-energy, and the energy of the conduction-band electrons and holes, relative to the top of the valence band, has been written in terms of the energy of effective single particle states with a reduced mass $m_{\mathrm{c}}^{*} = m_{\mathrm{c}} m_{\mathrm{h}}/(m_{\mathrm{c}} + m_{\mathrm{h}})$.

D. Construction of optical elements in the experimental setup

Chapter 3 presented a number of optical elements used in the experimental setup, but did not specify much beyond their function. This appendix will expand on the working principles of the optical elements and how they were constructed in the lab using beam splitters, lenses and wave plates. For the electro-optic and acousto-optic modulators, commercial components were used, and as such the construction of these elements will not be detailed. The appendix will conclude with a schematic of the entire experimental setup in terms of optical components.

D.1 Attenuators

The lasers used in the setup must operate at a power above the so-called laser threshold. As such, the laser is operated at a power which is higher than what is desired for the optical drive, and consequently, optical elements known as *attenuators* had to be used to adjust the optical power to a satisfactory level. An attenuator can be constructed using a half-wave plate and a polarizing beam splitter.

The half-wave plate is an optical component constructed from a birefringent material, which has anisotropic refractive properties. A birefringent material is characterized by its orthogonal fast and slow axes, where the fast and slow refers to the relative phase-speed of the electric field component of light along said axis. Thus, light traveling through a birefringent material will obtain a relative phase shift between the electric field components along the fast and slow axes, where the size of the phase shift will be proportional to the thickness of the material and the wavelength of the light, changing the polarization of the light. A half-wave plate has a thickness such that light with a specific frequency will obtain a relative phase shift of π, displacing the waves by a half wavelength, between the fast and slow axis. A half-wave plate acting on linearly polarized light will in effect rotate the polarization with an angle dependent on the relative angle between the fast axis of the wave plate and the polarization of the incident light [49].

A polarizing beam splitter (PBS) similarly distinguishes between two axes, which we will refer to as its eigenaxes. The PBS will reflect all light polarized along one of its eigenaxes, and transmit all of the light polarized along the other, orthogonal axis. By placing a half-wave plate in front of the PBS, one can adjust the ratio between transmitted and reflected light by rotating the wave plate. Thus, one can create an adjustable attenuator by combining a half-wave plate and a PBS, and blocking either the reflected or transmitted light, as illustrated in Fig. D.1.

D.2 Galilean expander

In the experimental setup, a Galilean expander is used to increase the beam waist of the laser beam before the objective lens, resulting in a reduced focused beam waist at

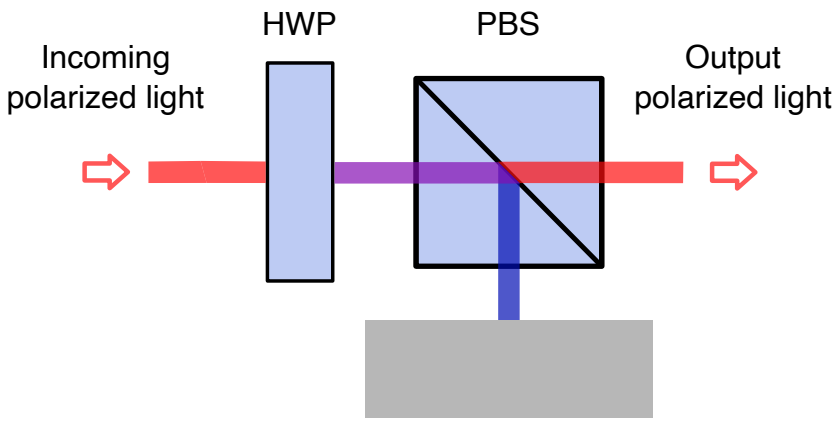

Figure D.1: Schematic of an optic attenuator consisiting of a half-wave plate (HWP) and a polarizing beam splitter (PBS) with one of the output paths blocked. The light polarized along an eigenaxis of the PBS is colored red or blue depending on the axis. Areas where light of both polarizations overlap are colored purple.

the surface of the sample. More generally, a Galilean expander is an anisotropic optical element with two ports that increases the beam waist of light entering through one port, and reduces the beam waist of light entering through the other.

A Galilean expander can be constructed from two thin-lenses, one negative and one positive lens. Light passing through a thin lens obeys the *Gaussian lens formula* [49]:

$$\frac{1}{s_\mathrm{o}} + \frac{1}{s_\mathrm{i}} = \frac{1}{f}, \tag{D.1}$$

where the light spreads out from a point at distance s_o in front of the lens, and the light is focused at a point at distance s_i after the lens, and where f is the focal length of the lens. Lenses can be characterised by the sign of the focal length, denoting them as either positive or negative. Negative lenses, $f < 0$, will spread incoming light such that the distance s_i is negative, as opposed to positive lenses which focuses incident light. The mechanics of positive and negative lenses are illustrated in Figs. D.2a) & b).

A Galilean expander can be constructed from a negative and positive lens with coinciding focal points. Collimated light entering through the negative lens will be spread by the negative lens and collimated by the positive lens, effectively increasing the radius of the collimated light. Collimated light entering through the positive lens however, will be focused by the positive lens and collimated by the negative lens, effectively reducing the radius of the light. This is illustrated in Fig. D.2c).

D.3 Circulator

A circulator is a component with at least three ports, for which a signal entering through one port will exit through the next in a cyclical fashion, commonly used to separate an incident and reflected signal. For this use specifically, it is sufficient for the circulator to have a functioning first and second port. An optical circulator satisfying these requirements can be be constructed from a polarizing beam splitter and a quarter-wave plate. The quarter-wave plate, similarly to the half-wave plate will shift the polarization of the incident light. For the special case where the fast-axis of the quarter-wave plate subtends a 45° angle with the eigenaxes of the PBS, the light exiting from the PBS and entering through the quarter-wave plate will be polarized circularly [49]. If light passes through

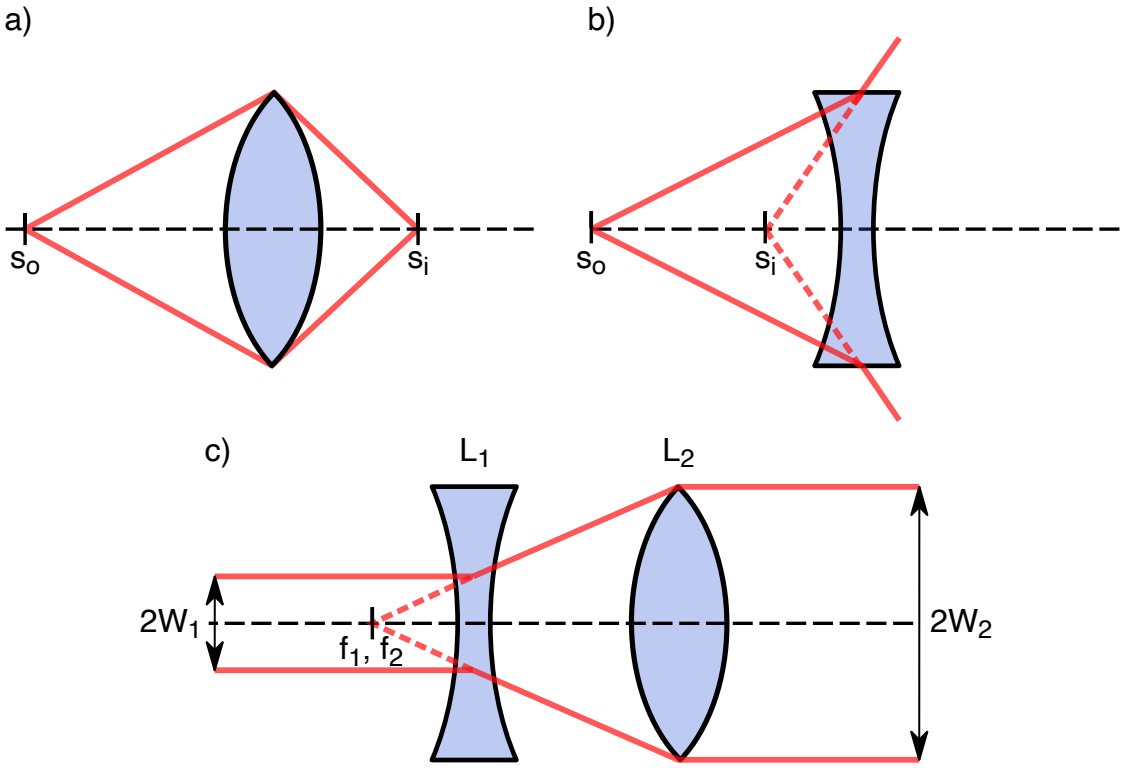

Figure D.2: a) Illustration of the mechanics of a lens with a positive focal length. The light rays emerge a length s_o before the lens, and are focused after a length s_i after the lens. b) Illustration of the mechanics of a lens with a negative focal length. Here the light rays are spread by the lens, as if they are focused to a negative length s_i after the lens. c) Illustration of a collimated beam passing through a Galilean expander. The lenses are placed such that their focal points, f_1 and f_2, coincide. For a beam entering through the positive (negative) lens, the beam waist is increased (decreased) from W_1 (W_2) to W_2 (W_1). The optical axis is shown in all figures as a dashed horizontal line.

two quarter-wave plates, the total effect will be equal to that of a half-wave plate. With the fast axis rotated 45° with respect to the linear polarization of the incident light, the polarization will be rotated by 90°. Thus, light transmitted through the PBS and passing through the wave plate twice, once as incident light and once as reflected, will be linearly polarized along the other eigenaxis of the PBS, resulting in total reflection at the PBS, constituting the operation of a circulator. This process is illustrated in Fig. D.3.

An added convenience of the circulator on this form is that the light can be linearly polarized before passing through the quarter-wave plate and after passing through the quarter wave plate again, which is desired for compatibility with polarizing beam splitters and as such attenuators. Furthermore, the light focused at the sample will be circularly polarized, which is necessary to address a specific valley of the TMD.

D.4 Other optical components in the setup

In addition to the components presented, the optical setup uses three additional types of components: an isolator, fiber adapters, and mirrors.

The isolator is placed just after the laser, and serves two purposes. Its main purpose is to admit incident light and block reflected light, such that no light is reflected back into the laser device. It additionally acts as an initial polarizer, polarizing the laser to a linear polarization, which is a requirement for the use of wave plates.

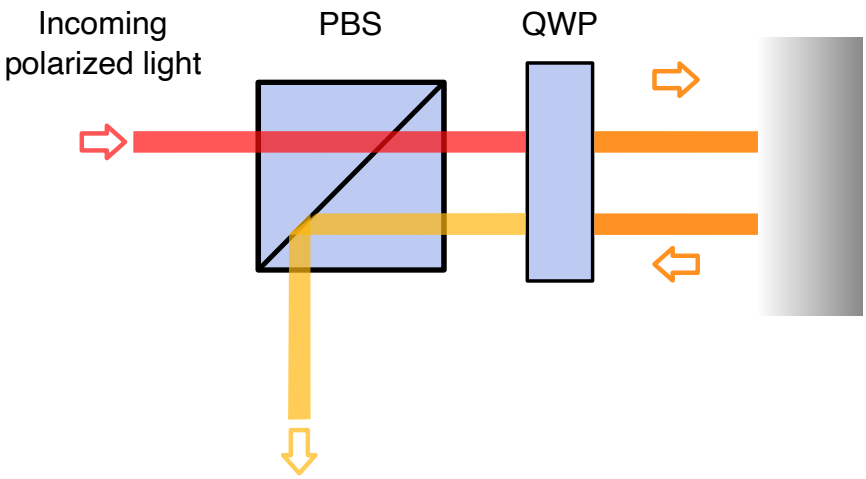

Figure D.3: Schematic of an optical circulator constructed from a polarizing beam splitter (PBS) and a quarter-wave plate (QWP). The incident light is assumed to be linearly polarized such that it passes through the PBS, whereas the reflected light will enter the PBS with the orthogonal linear polarization such that it is entirely reflected. The color of the light denotes the polarization, where red denotes horizontal linear polarization, orange denotes circular polarization, and yellow denotes vertical linear polarization.

Fiber adapters are used to transfer the light to and from optical fibers. Some of the optical components, such as the fiber adapters and lenses, are very sensitive to the relative position and direction of the beam's incidence. For instance, the formulas used for the mechanics of the lenses assumes the beam enters at the center of the lens and that it propagates along the optical axis. In order to control the position and direction of the beam, two mirrors with adjustable angles are used. Each mirror provides two degrees of freedom in adjusting the angle of reflection, which collectively provides control of both the position and direction of the reflected beam. The process of adjusting the mirrors to position the laser beam is referred to as alignment. For this process it is also common to adjust the position of the components themselves.

A schematic of the optical setup, containing all of the components, is shown in Fig. 3.4.

References

[1] A. V. Chumak, V. I. Vasyuchka, A. A. Serga, and B. Hillebrands. Magnon spintronics. *Nature Physics*, 11(6):453–461, 2015.

[2] Y. Tabuchi, S. Ishino, A. Noguchi, T. Ishikawa, R. Yamazaki, K. Usami, and Y. Nakamura. Coherent coupling between a ferromagnetic magnon and a superconducting qubit. *Science*, 349(6246):405–408, 2015.

[3] A. K. Geim and I. V. Grigorieva. Van der waals heterostructures. *Nature*, 499(7459):419–425, 2013.

[4] R. Hisatomi, A. Osada, Y. Tabuchi, T. Ishikawa, A. Noguchi, R. Yamazaki, K. Usami, and Y. Nakamura. Bidirectional conversion between microwave and light via ferromagnetic magnons. *Physical Review B*, 93(17):174427, 2016.

[5] N. J. Lambert, A. Rueda, F. Sedlmeir, and H. G. Schwefel. Coherent conversion between microwave and optical photons—an overview of physical implementations. *Advanced Quantum Technologies*, 3(1):1900077, 2020.

[6] L. Ciorciaro, M. Kroner, K. Watanabe, T. Taniguchi, and A. Imamoğlu. Observation of magnetic proximity effect using resonant optical spectroscopy of an electrically tunable $MoSe_2/CrBr_3$ heterostructure. *Physical Review Letters*, 124(19):197401, 2020.

[7] D. Lachance-Quirion, Y. Tabuchi, A. Gloppe, K. Usami, and Y. Nakamura. Hybrid quantum systems based on magnonics. *Applied Physics Express*, 12(7):070101, 2019.

[8] D. Lachance-Quirion, S. P. Wolski, Y. Tabuchi, S. Kono, K. Usami, and Y. Nakamura. Entanglement-based single-shot detection of a single magnon with a superconducting qubit. *Science*, 367(6476):425–428, 2020.

[9] S. P. Wolski, D. Lachance-Quirion, Y. Tabuchi, S. Kono, A. Noguchi, K. Usami, and Y. Nakamura. Dissipation-based quantum sensing of magnons with a superconducting qubit. arxiv:2005.09250, 2020.

[10] X. Xu, W. Yao, D. Xiao, and T. F. Heinz. Spin and pseudospins in layered transition metal dichalcogenides. *Nature Physics*, 10(5):343–350, 2014.

[11] S. Manzeli, D. Ovchinnikov, D. Pasquier, O. V. Yazyev, and A. Kis. 2D transition metal dichalcogenides. *Nature Reviews Materials*, 2(8):17033, 2017.

[12] B. Scharf, G. Xu, A. Matos-Abiague, and I. Žutić. Magnetic proximity effects in transition-metal dichalcogenides: converting excitons. *Physical review letters*, 119(12):127403, 2017.

[13] C. W. Gardiner and M. J. Collett. Input and output in damped quantum systems: Quantum stochastic differential equations and the master equation. *Physical Review A*, 31(6):3761, 1985.

[14] M. Fox. *Quantum optics: an introduction*. OUP Oxford, 2006.

[15] D. D. Stancil and A. Prabhakar. *Spin waves*, volume 5. Springer, 2009.

[16] A. G. Gurevich and G. A. Melkov. *Magnetization oscillations and waves*. CRC press, 1996.

[17] C. Kittel. *Introduction to solid state physics*, volume 8. Wiley New York, 1967.

[18] B. Bhoi, T. Cliff, I. S. Maksymov, M. Kostylev, R. Aiyar, N. Venkataramani, S. Prasad, and R. L. Stamps. Study of photon–magnon coupling in a YIG-film split-ring resonant system. *Journal of Applied Physics*, 116(24):243906, 2014.

[19] L.-M. Duan. Entanglement detection in the vicinity of arbitrary dicke states. *Physical review letters*, 107(18):180502, 2011.

[20] R. H. Dicke. Coherence in spontaneous radiation processes. *Physical review*, 93(1):99, 1954.

[21] D. F. Walls and G. J. Milburn. *Quantum optics*. Springer Science & Business Media, 2007.

[22] Y. Yamamoto and A. Imamoğlu. *Mesoscopic quantum optics*. John Wiley, 1999.

[23] H. Haug and S. W. Koch. *Quantum theory of the optical and electronic properties of semiconductors: fivth edition*. World Scientific Publishing Company, 2009.

[24] W. Yao, D. Xiao, and Q. Niu. Valley-dependent optoelectronics from inversion symmetry breaking. *Physical Review B*, 77(23):235406, 2008.

[25] T. Cao, G. Wang, W. Han, H. Ye, C. Zhu, J. Shi, Q. Niu, P. Tan, E. Wang, B. Liu, and J. Feng. Valley-selective circular dichroism of monolayer molybdenum disulphide. *Nature communications*, 3(1):1–5, 2012.

[26] D. Xiao, G.-B. Liu, W. Feng, X. Xu, and W. Yao. Coupled spin and valley physics in monolayers of MoS_2 and other group-VI dichalcogenides. *Physical review letters*, 108(19):196802, 2012.

[27] M. Koperski, M. R. Molas, A. Arora, K. Nogajewski, M. Bartos, J. Wyzula, D. Vaclavkova, P. Kossacki, and M. Potemski. Orbital, spin and valley contributions to zeeman splitting of excitonic resonances in $MoSe_2$, WSe_2 and WS_2 monolayers. *2D Materials*, 6(1):015001, 2018.

[28] Y. Zhang, T.-R. Chang, B. Zhou, Y.-T. Cui, H. Yan, Z. Liu, F. Schmitt, J. Lee, R. Moore, Y. Chen, H. Lin, H.-T. Jeng, Z. Hussain, A. Bansil, and Z.-X. Shen. Direct observation of the transition from indirect to direct bandgap in atomically thin epitaxial $MoSe_2$. *Nature nanotechnology*, 9(2):111, 2014.

[29] A. Arora, K. Nogajewski, M. Molas, M. Koperski, and M. Potemski. Exciton band structure in layered $MoSe_2$: from a monolayer to the bulk limit. *Nanoscale*, 7(48):20769–20775, 2015.

[30] A. Chernikov, T. C. Berkelbach, H. M. Hill, A. Rigosi, Y. Li, O. B. Aslan, D. R. Reichman, M. S. Hybertsen, and T. F. Heinz. Exciton binding energy and nonhydrogenic rydberg series in monolayer WS_2. *Physical review letters*, 113(7):076802, 2014.

[31] R. C. Miller, D. A. Kleinman, W. T. Tsang, and A. C. Gossard. Observation of the excited level of excitons in GaAs quantum wells. *Physical Review B*, 24(2):1134, 1981.

[32] A. Kormányos, G. Burkard, M. Gmitra, J. Fabian, V. Zólyomi, N. D. Drummond, and V. Fal'ko. k · p theory for two-dimensional transition metal dichalcogenide semiconductors. *2D Materials*, 2(2):022001, 2015.

[33] K. He, N. Kumar, L. Zhao, Z. Wang, K. F. Mak, H. Zhao, and J. Shan. Tightly bound excitons in monolayer WSe_2. *Physical review letters*, 113(2):026803, 2014.

[34] S. Zeytinoğlu, C. Roth, S. Huber, and A. Imamoğlu. Atomically thin semiconductors as nonlinear mirrors. *Physical Review A*, 96(3):031801, 2017.

[35] A. Srivastava, M. Sidler, A. V. Allain, D. S. Lembke, A. Kis, and A Imamoğlu. Valley zeeman effect in elementary optical excitations of monolayer WSe_2. *Nature Physics*, 11(2):141–147, 2015.

[36] T. Norden, C. Zhao, P. Zhang, R. Sabirianov, A. Petrou, and H. Zeng. Giant valley splitting in monolayer WS_2 by magnetic proximity effect. *Nature communications*, 10(1):1–10, 2019.

[37] J. Qi, X. Li, Q. Niu, and J. Feng. Giant and tunable valley degeneracy splitting in $MoTe_2$. *Physical Review B*, 92(12):121403, 2015.

[38] A. A. Clerk, M. H. Devoret, S. M. Girvin, F. Marquardt, and R. J. Schoelkopf. Introduction to quantum noise, measurement, and amplification. *Reviews of Modern Physics*, 82(2):1155, 2010.

[39] A. Gloppe, M. Onga, R. Hisatomi, A. Imamoğlu, Y. Nakamura, Y. Iwasa, and K. Usami. Proximity-mediated magnon-exciton coupling at a van der waals heterointerface. arxiv:2006.14257, 2020.

[40] A. Blais, J. Gambetta, A. Wallraff, D. I. Schuster, S. M. Girvin, M. H. Devoret, and R. J. Schoelkopf. Quantum-information processing with circuit quantum electrodynamics. *Physical Review A*, 75(3):032329, 2007.

[41] C. Zhao, T. Norden, P. Zhang, P. Zhao, Y. Cheng, F. Sun, J. P. Parry, P. Taheri, J. Wang, Y. Yang, T. Scrace, K. Kang, S. Yang, G. Miao, R. Sabirianov, G. Kioseoglou, W. Huang, A. Petrou, and H. Zeng. Enhanced valley splitting in monolayer WSe_2 due to magnetic exchange field. *Nature nanotechnology*, 12(8):757, 2017.

[42] A. F. Kockum, A. Miranowicz, S. De Liberato, S. Savasta, and F. Nori. Ultrastrong coupling between light and matter. *Nature Reviews Physics*, 1(1):19–40, 2019.

[43] B. E. Saleh and M. C. Teich. *Fundamentals of photonics*. John Wiley & Sons, 2007.

[44] L. Novotny and B. Hecht. *Principles of nano-optics*. Cambridge university press, 2012.

[45] H.-A. Bachor and T. C. Ralph. *A guide to experiments in quantum optics*, volume 1. Wiley Online Library, 2004.

[46] L. R. Walker. Magnetostatic modes in ferromagnetic resonance. *Phys. Rev.*, 105:390–399, Jan 1957.

[47] T. Holstein and H. Primakoff. Field dependence of the intrinsic domain magnetization of a ferromagnet. *Physical Review*, 58(12):1098, 1940.

[48] T. L. Gilbert. A phenomenological theory of damping in ferromagnetic materials. *IEEE transactions on magnetics*, 40(6):3443–3449, 2004.

[49] E. Hecht. *Optics*. Addison Wesley, 2002.

List of Figures

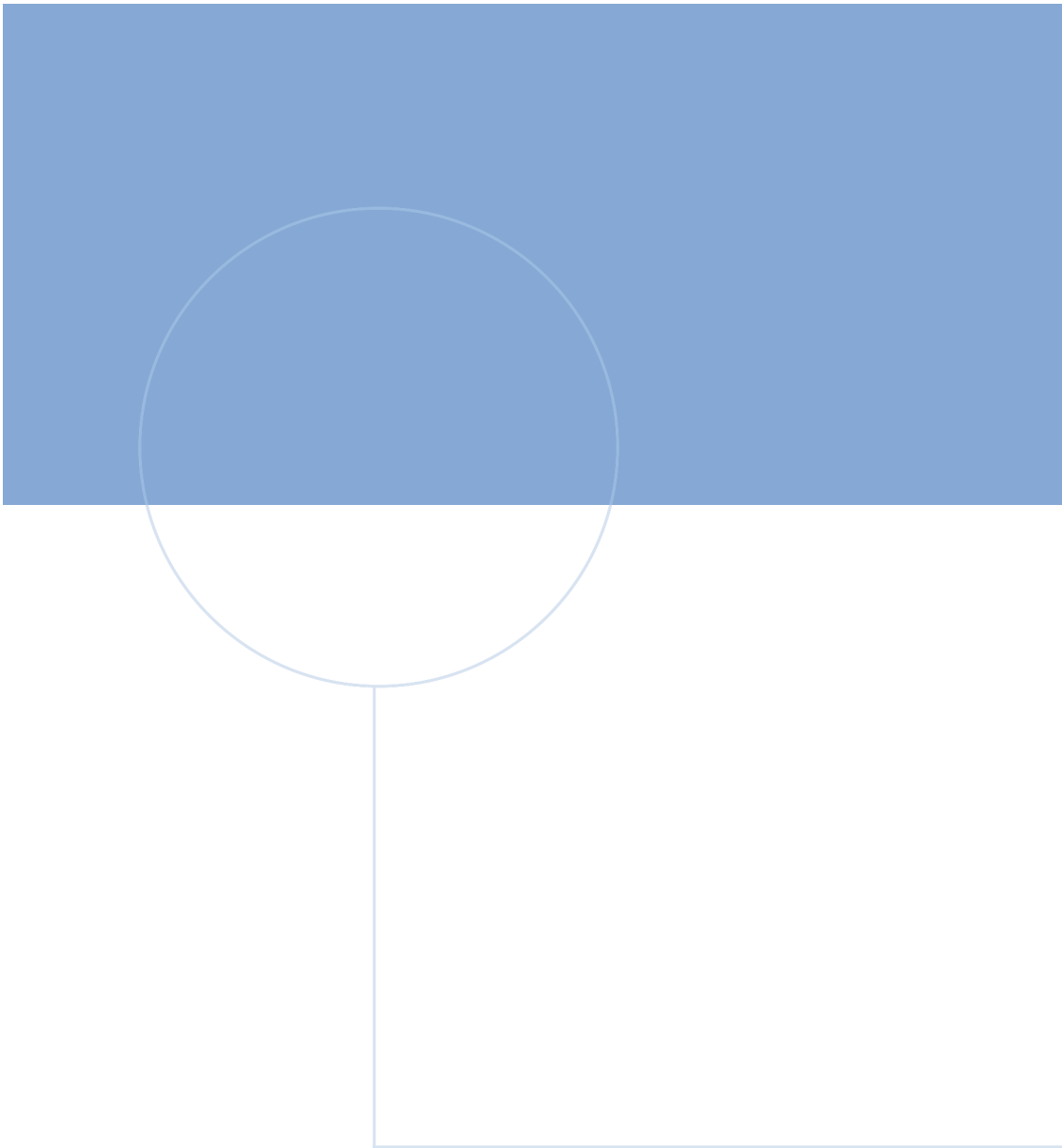

NTNU

Norwegian University of
Science and Technology